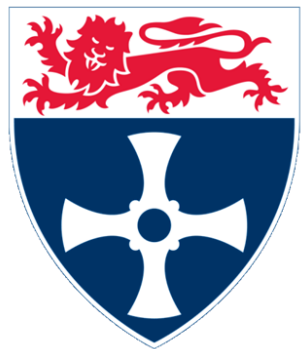


The Squirrel Cage Induction Machine As An Alternative To The Permanent Magnet Generator For Direct Drive Tidal Turbines

Liam Alexander Naugher

A thesis submitted for the degree of
Doctor of Philosophy



School of Electrical and Electronic Engineering

Newcastle University 2018

Abstract

This thesis looks at the direct drive power take off options for the OpenHydro tidal energy turbine and includes an investigation of the existing permanent magnet generator. The squirrel cage induction machine was chosen as an alternative design after reviewing the literature. The lack of rare earth magnet content of the induction machine was an opportunity to improve the cost competitiveness of the OpenHydro tidal turbine to alternative renewable energy sources. The induction machine has been utilised with a gearbox in tidal turbines elsewhere, but in this work a direct drive design has been created.

The generator of the OpenHydro turbine is positioned on the outer rim of the turbine blades, the rotor has a 14m outer diameter. Segmentation of the generator simplifies the construction and assembly of the turbine and also improves the fault tolerance of the turbine, depending on the coil connections.

The existing permanent magnet design was evaluated with a simplified linear FEA model which underwent both manual and numerical optimisation. The optimisation found that the magnet mass could be reduced with minimum impact on the performance of the generator.

To design and model the induction machine, each individual segment was wrapped to form a rotary induction machine, the conventional design process was then used to design the segment. FEA models of three designs were used to investigate the number of segments, with the best design then manually optimised. The study produced a model that was comparable to the permanent magnet generator performance, but with a lower power factor.

The turbine features a buoyant shaft less rotor and as a consequence the generator suffers from eccentricity. The effect of eccentricity on the individual segments of both the permanent magnet and induction machine was investigated using linear FEA models. The eccentricity impacted the permanent magnet design in the voltage and EMF whereas the current was affected for the induction machine design. A numerical model, based on publications, was created to evaluate the effect on the fully assembled generator. The model was able to reproduce the presented inductances.

For the comparison of the two designs the material costs of the permanent magnet and induction machine were calculated. The available power of a deployment site was calculated using the simulated efficiencies of the two generators, the models were run across the speed range corresponding to the tidal speeds. The cost of this energy sold was then used to compare the two generators over a 15 year lifetime. The capital cost of the induction machine design was 17% lower than that of the permanent magnet, over a 15 year lifetime the net income of the induction machine was 16% lower at a rated speed of 25rpm. The optimised permanent magnet design has 0.1% higher net income and a 9% lower capital cost than the original permanent magnet design. The profitability index is higher than both the original and induction machine.

Acknowledgements

I would like to acknowledge my poor computer whose hard drive was always full, and never once defragmented over the course of my PhD. Not once did it crash while simultaneously solving two FEA simulations, streaming music and processing a word document.

I would like to thank my supervisors Dr Nick Baker and Dr Glynn Atkinson whose patience and understanding allowed me to complete this work. It was a long and arduous journey but I think I came through it relatively unscathed, I'm unsure about my supervisors though.

Obviously thanks to my colleagues of the UG lab; Yang, Yin, Osama, Aslan, Richard, Muhsien, Junnan, Iago, Nasiru, Tahani, Raihan and Ahmed, who had to listen to many hare-brained ideas over the last four years. It's finally over, you can rest easy, I'm leaving.

And finally my family who never really understood what I was doing for the last four years but continued to support me. Mostly my parents who provided a poor eternal student with food and shelter and only sometimes questioned when I would get a job.

Table of contents

Abstract	i
Acknowledgements	ii
Table of contents	iii
Table of figures	viii
Table of abbreviations.....	xi
Chapter 1. Introduction	1
1.1. The importance of tidal energy	1
1.2. Tidal energy extraction.....	1
1.2.1. Tidal barrage	1
1.2.2. Tidal lagoons.....	2
1.2.3. Tidal stream.....	3
1.3. The OpenHydro turbine	4
1.4. Project aims and objectives	5
1.5. Contributions to knowledge	5
1.6. Publications	5
1.7. Thesis overview.....	5
Chapter 2. Tidal turbines and tidal energy	6
2.1. Tidal turbine system	6
2.1.1. OpenHydro turbine system.....	7
2.1.2. The power coefficient and the tip speed ratio	7
2.1.3. Tidal power	10
2.2. Tidal resource modelling.....	11
2.2.1. OpenHydro site model	13
2.2.2. Tidal speed occurrences	14
2.3. Demands on electrical machine.....	15
2.4. Types of tidal turbines.....	15
2.4.1. SeaGen-S.....	15
2.4.2. AR-1500.....	16
2.4.3. SR2000.....	16
2.4.4. HS1000.....	17

Table of contents

2.4.5.	CoRMat 500	17
2.4.6.	Comparison of the turbines.....	18
2.5.	Electrical machines.....	19
2.5.1.	Squirrel cage induction generator (SCIG)	19
2.5.2.	Doubly fed induction generator (DFIG).....	19
2.5.3.	Brushless doubly fed induction generator (BDFIG).....	20
2.5.4.	Wound field synchronous generator (WFSG)	21
2.5.5.	Permanent magnet synchronous generator (PMSG).....	21
2.5.6.	Switched reluctance generator (SRG)	22
2.5.7.	Double stator axial flux permanent magnet generator (DSAFPMG)	23
2.5.8.	Transverse flux generator (TFG).....	23
2.5.9.	Claw pole generator (CPG)	24
2.6.	Discussion of electrical machines.....	25
2.7.	Summary.....	25
Chapter 3.	Permanent magnet machine	26
3.1.	The existing permanent magnet design	26
3.2.	The simplified FEA model	27
3.2.1.	Linear model validation.....	28
3.3.	Optimisation	31
3.3.1.	Constraints.....	32
3.3.2.	Coarse design study	34
3.3.3.	Fine design study	36
3.3.4.	Numerical optimisation	38
3.4.	Power and efficiency	40
3.5.	Selection of final machine	41
3.6.	Summary.....	41
Chapter 4.	Induction machine	42
4.1.	Design specification	42
4.2.	Number of segments.....	43
4.3.	Modelling the segment	44

4.3.1.	Wrapping the segment.....	44
4.3.2.	Initial design parameters	45
4.4.	Development of the analytical design model	45
4.4.1.	Output coefficient method.....	46
4.4.2.	Saturation factor estimation.....	46
4.4.3.	Initial sizing of the machine	48
4.4.4.	Stator design.....	49
4.4.5.	Rotor design	50
4.4.6.	Validity of the slot width guideline in a large air gap machine.....	53
4.4.7.	Execution of the proposed analytical design method	57
4.5.	The initial designs	62
4.6.	40 segment optimisation.....	67
4.7.	60 segment optimisation.....	68
4.7.1.	Comparison of the designs	69
4.8.	100 segment optimisation.....	70
4.9.	Selection of segment number	72
4.10.	JMag linear model of IM-60-1	72
4.11.	Performance of linear induction machine over the tidal speed range.....	74
4.12.	Summary	76
Chapter 5.	Eccentricity.....	77
5.1.	The problem of eccentricity	77
5.2.	Eccentricity in the permanent magnet segment.....	78
5.3.	Eccentricity in the induction machine segment.....	79
5.4.	Eccentricity model.....	80
5.4.1.	The windings function approach	81
5.4.2.	Inductance	82
5.5.	Model validation	84
5.6.	60 Segment induction machine	86
5.7.	Summary	87
Chapter 6.	The cost of energy	88

Table of contents

6.1.	Overview of key factors affecting cost.....	88
6.1.1.	Capital costs.....	88
6.1.2.	Operational and maintenance costs	88
6.1.3.	Energy supply	88
6.2.	Turbine capital costs.....	89
6.2.1.	Installation and deployment costs.....	89
6.2.2.	Material costs.....	89
6.2.3.	Labour costs.....	91
6.3.	Operational and maintenance costs	91
6.4.	Drive system.....	91
6.5.	Annual tidal energy	92
6.6.	Net present value	93
6.7.	Summary.....	94
Chapter 7.	Conclusion.....	95
7.1.	Overview	95
7.1.1.	Permanent magnet optimisation	95
7.1.2.	Squirrel cage induction generator.....	95
7.1.3.	Eccentricity.....	95
7.1.4.	The cost of energy	95
7.2.	Permanent magnet generator	96
7.3.	Squirrel cage induction generator.....	96
7.4.	Eccentricity.....	96
7.5.	The cost of energy	97
7.6.	Future work	97
7.7.	Summary.....	99
Appendix A:	Eccentricity Matlab script.....	100
A1.	Validation model script	100
A2.	60 Segment script	105
A3.	60 Segment inductance calculations script.....	107
A4.	Current and torque calculation script.....	108

A5. Functions	109
A5i. Integra function	109
A5ii. InductanceMatrix function	109
References	110

Table of figures

Figure 1: Tidal barrage	2
Figure 2: La Rance tidal barrage [8].....	2
Figure 3: 320 MW Pathfinder project, Swansea Bay [10].....	3
Figure 4: OpenHydro Turbine [16]	4
Figure 5: Generalised tidal turbine system	6
Figure 6: OpenHydro tidal turbine system	7
Figure 7: Typical power coefficient curve	8
Figure 8: Different power coefficient calculations	8
Figure 9: Tip speed ratio.....	9
Figure 10: Linear relationship of tidal speed and turbine speed.....	10
Figure 11: Marine power against tidal flow speed, with cut in and cut out speeds.	10
Figure 12: Tidal turbine array [21]	11
Figure 13: Rosyth harbour site	12
Figure 14: Comparison of tidal speed based on the tidal atlas and from the equation	12
Figure 15: OpenHydro project deployment sites [4]	13
Figure 16: Model monthly semi-diurnal tide.....	13
Figure 17: Histogram of tidal speed and annual occurrence	14
Figure 18: SeaGen-S deployment.....	15
Figure 19: Submerged AR-1500.....	16
Figure 20: Deployed SR2000	16
Figure 21: ANDRITZ HYDRO Hammerfest HS1000	17
Figure 22: CoRMat 500 being installed at EMEC.....	17
Figure 23: Connection of a conventional SCIG to the grid.....	19
Figure 24: Grid connection of a typical DFIG.....	20
Figure 25: Connection of the BDIG to the grid [39]	20
Figure 26: 2 pole wound field synchronous machine [40]	21
Figure 27: Permanent magnet synchronous machine [43]	22
Figure 28: Switched reluctance machine [36]	22
Figure 29: Double stator axial flux permanent magnet generator [45].....	23
Figure 30: Transverse flux machine [47]	24
Figure 31: (a) Stator claw pole [48]; (b) Rotor claw pole [49].....	24
Figure 32: Single stator segment and two rotor segments	26
Figure 33: Simplification of the CAD model	27
Figure 34: Linear single pole pair model.....	29
Figure 35: Flux linkage generated in the coils of both the OpenHydro model and the simplified linear model respectively.....	29

Figure 36: EMF of the CAD and simple linear model	30
Figure 37: Force of the CAD and simplified linear model.....	30
Figure 38: Magnet dimensions	31
Figure 39: Air gap flux density for maximum and minimum magnet width	33
Figure 40: Harmonics of the flux densities of the maximum and minimum magnet widths	33
Figure 41: Initial design PM-72-3	34
Figure 42: FEA results of the coarse design study showing variation of average force with the magnet width and length.....	35
Figure 43: FEA results of the coarse design study showing variation of average force with the magnet width and height.....	35
Figure 44: FEA results of the coarse design study showing variation of average force with the magnet height and length.....	35
Figure 45: PM-72-16.....	36
Figure 46: FEA results of the fine design study showing variation of average force with the magnet width and length.....	37
Figure 47: FEA results of the fine design study showing variation of average force with the magnet width and height.....	37
Figure 48: FEA results of the fine design study showing variation of average force with the magnet height and length.....	37
Figure 49: Optimisation results of 225 cases	39
Figure 50: Optimisation cases exceeding the force threshold	39
Figure 51: Section of the rim generator.....	42
Figure 52: Segment span	43
Figure 53: Equating the segment circumferential length to the rotary model.....	44
Figure 54: Design workflow	46
Figure 55: B-H curve of M600-65A with reference point and rotor tooth operational point.....	48
Figure 56: Double layer winding slot layout.....	49
Figure 57: Triple layer slot layout.....	49
Figure 58: Fractional winding slot layout	49
Figure 59: Concentric broken chain end windings.....	50
Figure 60: Rotor slot shape for inverter driven induction machine	51
Figure 61: Progression from trapezoidal bars with rounded back to rectangular bars	52
Figure 62: Optimised design	52
Figure 63: Efficiency variation with slot opening, using FEA and ADM.....	56
Figure 64: Power factor variation with slot opening, using FEA and ADM.....	56
Figure 65: Design flowchart.....	57
Figure 66: Vertical and horizontal conductors in a slot	59
Figure 67: Half section of the squirrel cage	60

Figure 68: From left to right are the 40, 60 and 100 segment designs	62
Figure 69: Torque of the 60 segment.....	63
Figure 70: Torque-speed graph of the MotorSolve model	64
Figure 71: Efficiency of the MotorSolve model.....	64
Figure 72: Power factor of the MotorSolve model.....	64
Figure 73: Stator tooth and slot dimensions of the initial design	72
Figure 74: The linear segment.....	72
Figure 75: The linear segment with steel spacers.....	72
Figure 76: The linear segment with wider teeth	73
Figure 77: Force of the linear segment.....	73
Figure 78: Force of the linear segment with steel spacers.....	73
Figure 79: Force of the linear segment with wider teeth	74
Figure 80: Rotor eccentricity.....	77
Figure 81: Hydrodynamic squeeze film bearing	78
Figure 82: Permanent magnet linear model.....	79
Figure 83: Graph of EMF and flux density with an eccentric condition	79
Figure 84: Linear IM segment force and current with eccentricity	80
Figure 85: Stator model.....	81
Figure 86: Winding function a single phase	82
Figure 87: Winding function of a rotor bar	82
Figure 88: Results from [60] combined with the predictions from the Matlab model of the mutual inductance of stator phase a and rotor loop 1 with no eccentricity.....	85
Figure 89: Results from [60] combined with the predictions from the Matlab model of the magnetising inductance of rotor loop 1 with 50% static eccentricity	85
Figure 90: Results from [60] combined with the predictions from the Matlab model of the mutual inductance of stator phase a and rotor loop 1 with 50% static eccentricity.....	85
Figure 91: Mutual inductance of stator phase a and rotor loop 1 with no eccentricity from the Matlab model.....	86
Figure 92: Magnetising inductance of rotor loop 1 with 50% static eccentricity from the Matlab model	86
Figure 93: Mutual inductance of stator phase a and rotor loop 1 with 50% static eccentricity.....	87
Figure 94: OpenHydro deployment barge [68]	89
Figure 95: Material costs	90
Figure 96: Turbine control centre [69]	92
Figure 97: Annual energy extraction when 2.75 m/s is mapped to 15 rpm.....	92
Figure 98: Annual energy extraction when 2.75 m/s is mapped to 25 rpm.....	93

Table of abbreviations

ADM	–	Analytical design method
BDFIG	–	Brushless double fed induction generator
CAD	–	Computer aided design
CNPV	–	Cumulative net present value
CPG	–	Claw pole generator
CPVF	–	Cumulative present value factors
DF	–	Discount factor
DFIG	–	Double fed induction generator
DSAFPMG	–	Double stator axial flux permanent magnet generator
EMF	–	Electromotive force
FEA	–	Finite element analysis
FFT	–	Fast fourier transform
IM	–	Induction Machine
LIM	–	Linear induction machine
MMF	–	Magnetomotive force
MWFA	–	Modified winding function approach
PMSG	–	Permanent magnet synchronous generator
SCIG	–	Squirrel cage induction generator
SRG	–	Switched reluctance generator
TFG	–	Transverse flux generator
WFSG	–	Wound field synchronous generator

Chapter 1. Introduction

1.1. The importance of tidal energy

Fossil fuel power stations have reliably met UK energy demands for decades, and older power stations are being decommissioned. The construction of new facilities are opposed due to environmental concerns, and therefore alternative energy sources are required. Solar and wind technologies have been developed in recent years to work alongside existing energy sources to meet the growing energy demands of the UK. Tidal energy is a currently untapped resource with the UK possessing 48% [1] of the available energy along European coasts. Tidal energy is estimated to be capable of providing 12 TWh/year [1] to the UK grid. Projects have been investigating the extraction of energy from the sea using tidal stream and wave technology. There are various projects in development such as the Seagen-S a 2 MW turbine, which has generated 3 GWh between 2008-2012 [2]. Another project is the OpenHydro turbine rated at 2.2 MW, with sites capable of producing a total of 1 GW currently being developed [3]. Each site is capable of supporting multiple turbines in an array, the Bay of Fundy site has a 4 MW tidal array that has the potential to expand to a 300 MW tidal array [4].

Tidal energy is extremely predictable years in advance, however there are challenges such as the high development costs. Unlike wave energy devices, tidal energy devices are commonly located on the sea bed. This negates the hazardous surface conditions that occur during storms. The manufacturing costs of the turbine are determined by the material costs, the assembly and machining costs. A complex turbine design results in a high manufacturing cost. The deployment of a turbine requires offshore cranes, transport and divers (in the case of submerged turbines) resulting in high deployment costs. To operate the turbine in rough conditions the turbine has to be fault tolerant, the turbine design determines the operational and maintenance costs. This thesis is partnered with the company OpenHydro and focuses on the OpenHydro tidal turbine. The motivation of the project is to improve the cost competitiveness of tidal energy, with established renewable technology such as wind and solar.

1.2. Tidal energy extraction

Tidal energy refers to the kinetic energy of a large body of water, the extraction of this energy is the conversion of the kinetic energy to useful electrical energy that is fed to the grid. Large dams and barrages have been in operation for decades harnessing the kinetic energy from a body of water. Tidal barrages extract energy based on the change in water height (potential energy) and tidal stream which extracts kinetic energy directly from the flow of tidal water.

1.2.1. Tidal barrage

Tidal barrages isolate a section of shore referred to as a basin, when the sea level is higher than the basin the sluice gates are opened. This allows the water to move into the basin via channels containing

turbines. When the basin level matches the sea level the sluice gates are closed until the tide ebbs, at which point the basin water level is higher than sea level. The sluice gates are opened and water flows from the basin into the sea via the turbine [5]. Figure 1 shows a side view of a tidal barrage.

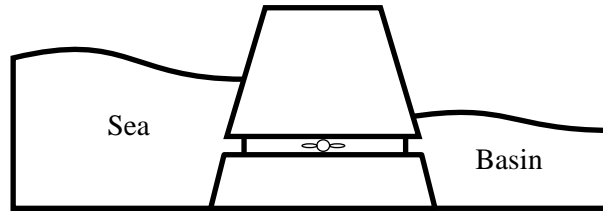


Figure 1: Tidal barrage

One of the most notable successful tidal barrages is the La Rance barrage, capable of producing 500 GWh/year shown in Figure 2. A barrage was proposed for the Severn estuary but concerns over wildlife dependent on the mudflats caused the proposal to be rejected. However a contradictory view was published by R. Kirby et al [6] in which it is claimed that a barrage would actually improve the environmental conditions. The Severn estuary has been a site of interest with papers published as early as 1949 [7] discussing a possible barrage.



Figure 2: La Rance tidal barrage [8]

1.2.2. Tidal lagoons

The operation of tidal lagoons is similar to tidal barrages [9], while the power generation capacity is reduced so is the environmental impact. Consequently tidal lagoons receive less opposition to deployment. Figure 3 shows the proposed deployment site for a tidal lagoon in Swansea Bay.



Figure 3: 320 MW Pathfinder project, Swansea Bay [10]

1.2.3. Tidal stream

Tidal stream devices operate similar to a tidal barrage without the surrounding architecture. The turbine is situated on the sea bed and extracts energy from the tidal currents [11]. However deploying the turbine below the surface increases the difficulty of the maintenance therefore increasing the operational cost.

The long term plan for the deployment of these machines is to place them in arrays similar to how wind turbines are arranged, this is to maximise the potential of power extracted from the site. An investigation of the environmental impact of an array of marine current turbines is necessary for each potential deployment site, an example of this type of investigation can be found in [12-14]. The turbine restricts the surrounding water flow consequentially creating a wake that affects turbines further downstream. The effect of this wake or turbulence on the downstream turbine is dependent on the ambient turbulence intensity (ATI), the authors [13] concluded that areas that have a higher ATI results in a narrower wake and the stream recovers quicker resulting in less of an environmental impact.

1.3. The OpenHydro turbine

A marine current turbine (MCT) is a device that converts the kinetic energy to electrical energy, where the kinetic energy is provided by the tidal variation. The operation of an MCT is somewhat similar to wind turbines except that the fluid density is significantly greater, as energy is provided by the flow of water instead of air. There are 2 categories of generator designs, direct drive and geared. The turbine shown in Figure 4 is the OpenHydro turbine that uses a rim-driven generator. The active parts of the generator are placed around the outer rim of the blades, this type of generator is a direct drive generator. A direct drive generator does not require a gearbox, however the generator must be designed to operate at low speeds. This results in the number of poles being quite large and increases the weight of the generator. However the absence of a gearbox means there is one less potential failure point in the turbine.

This project is partnered with the company OpenHydro, the technical design data of a commercial generator was provided by OpenHydro. The OpenHydro turbine is a shaft-less design using a permanent magnet synchronous generator. The rotor is neutrally buoyant and free to rotate in a large flooded gap. The present generator design is a surface mounted permanent magnet machine [15], the generator is heavily reliant on expensive rare earth materials to generate the air gap field. For example a 2 MW tidal turbine might rotate at just 25 rpm, in which case the generator torque is almost 1 MNm. As the torque is related to machine active volume, direct drive machines tend to be large and heavy.

The company OpenHydro was formed in 2005 and OpenHydro has achieved a number of industry firsts, including being the first to deploy a tidal turbine at the European Marine Energy Centre (EMEC) [3]. The original turbine prototype was 6 m in diameter with the latest prototype being 16 m in diameter. The company is based in Ireland with projects across the globe including the Bay of Fundy in Nova Scotia and in Japan.

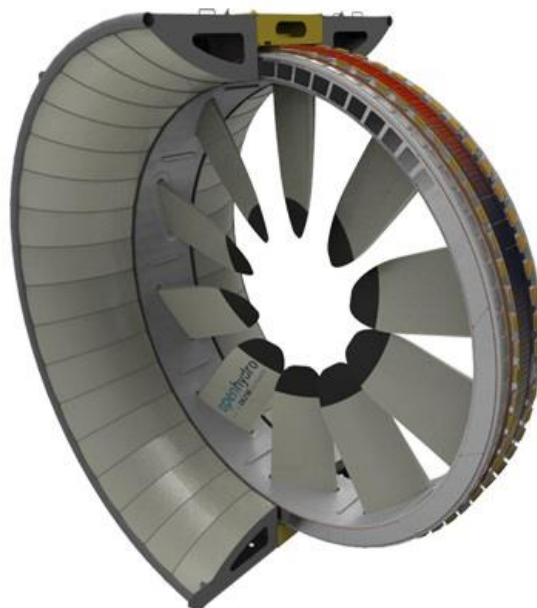


Figure 4: OpenHydro Turbine [16]

1.4. Project aims and objectives

The overall aim is to improve the cost competitiveness of the OpenHydro tidal turbine by focusing on the generator and the associated costs.

Objectives:

1. Optimisation of the existing permanent magnet generator
2. Design an alternative generator (Induction generator)
3. Comparison of the optimised generator and the alternative design

1.5. Contributions to knowledge

- A Feasibility study of a direct drive squirrel cage induction machine for use in a tidal turbine.
- Presented a modified design procedure of large scale squirrel cage induction machine.
- Comparison of direct drive permanent magnet design and induction machine based on material costs and energy supplied.
- Eccentricity study of large scale induction machine based on existing literature.

1.6. Publications

L. A. Naugher, N. J. Baker, and G. Atkinson, "Large air gap squirrel cage induction generator for a tidal turbine," in *8th IET International Conference on Power Electronics, Machines and Drives (PEMD 2016)*, 2016, pp. 1-6.

N. J. Baker, L. A. Naugher, "Large direct drive generators: The induction machine as an alternative to permanent magnet machines." in *7th IET International Conference on Renewable Power Generation (RPG 2018)*, accepted and awaiting publication.

1.7. Thesis overview

Chapter 2 Tidal turbines – This chapter reviews other tidal turbine prototypes as well as reviews alternative machine types for this application.

Chapter 3 Permanent magnet optimisation – This chapter focuses on the existing generator, simplification for modelling, manual and numerical optimisation.

Chapter 4 Induction machine design – This chapter describes the design procedure of the alternative design and manual optimisation.

Chapter 5 Eccentricity – This chapter introduces the concept of eccentricity of the turbine and begins to investigate the effect on both the permanent magnet and induction designs.

Chapter 6 The cost of energy – This is a comparison of the two designs based on material costs and energy generation.

Chapter 2. Tidal turbines and tidal energy

This chapter reviews the OpenHydro device and other tidal turbine prototypes and reviews alternative machine types for this application. Turbines, other than the OpenHydro turbine, are reviewed and the electrical machines used are identified. The different types of electrical machines are introduced and assessed with regards to the suitability for the application

2.1. Tidal turbine system

The system to extract the tidal energy can be generalised as in Figure 5. The turbine is deployed offshore connected by subsea cables to an onshore control unit. The subsea cables transfer the power from the turbines as well as monitoring data to the control unit. The energy is provided to the grid by the control unit.

The challenges to tidal turbines are not just physical but also economic, the system costs can be broken down into deployment, manufacture, operational and maintenance costs. The turbine system has high deployment costs as offshore cranes, transport and divers (in the case of submerged turbines) are required to successfully install the turbine at the desired deployment site. The manufacturing costs of the turbine are driven by not only the material costs but includes the assembly and machining costs, a complex turbine design results in a high cost. The operational and maintenance costs are determined by the robustness of the turbine to operate in rough conditions.

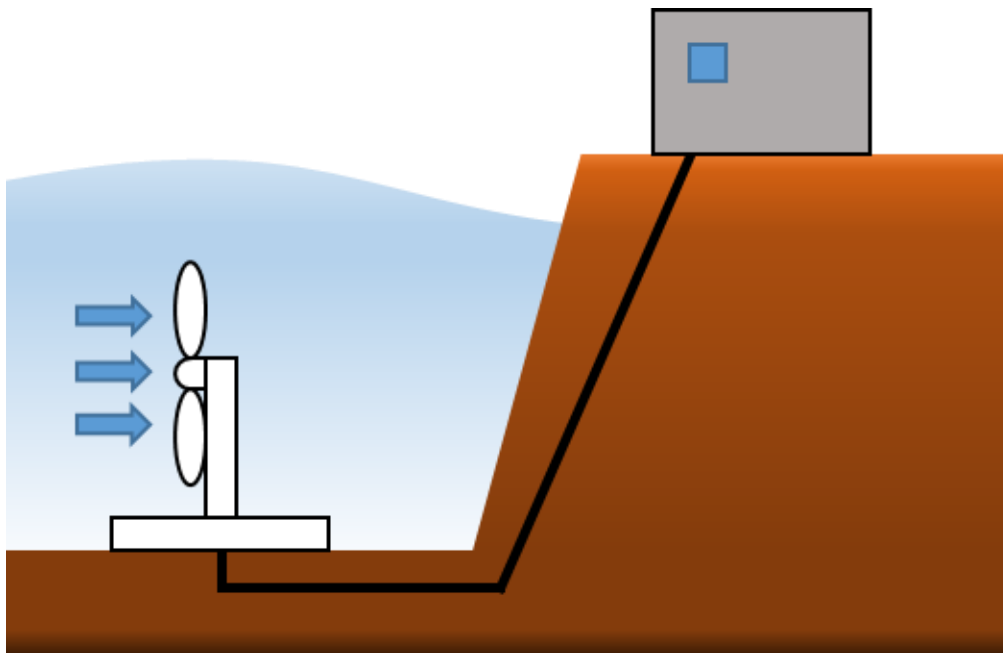


Figure 5: Generalised tidal turbine system

2.1.1. OpenHydro turbine system

The original turbine prototype was 6 m in diameter with the latest prototype being 16 m in diameter. The company is based in Ireland with projects across the globe including the Bay of Fundy in Nova Scotia and in Japan. The system is being actively developed, such as a custom control unit as opposed to an onshore solution and the construction of a custom barge for turbine deployment and retrieval.

The OpenHydro tidal turbine is deployed in arrays with a subsea control unit referred to as the turbine control centre (TCC). Figure 6 shows an example of a tidal array at a deployment site, the TCC is capable of controlling multiple turbines within the array. Rather than multiple cables to shore the TCC consolidates the outputs of the turbines and delivered to shore by a single cable. The OpenHydro turbine uses a direct drive generator and the active parts of the generator are placed around the outer rim of the blades. The generator must be designed to operate at low speeds as a direct drive generator does not have a gearbox. This increases the weight of the generator and the number of poles are quite large. However the absence of a gearbox means there is one less potential failure point in the turbine. As the torque is related to machine active volume, direct drive machines tend to be large and heavy.

The OpenHydro turbine is a shaft-less design using a permanent magnet synchronous generator and the present generator design is a surface mounted permanent magnet machine [15]. Expensive rare earth materials are required to generate the air gap field. The rotor is neutrally buoyant and free to rotate in a large flooded gap. The turbine prototype is rated as 2.2 MW and has a diameter of 16 m.

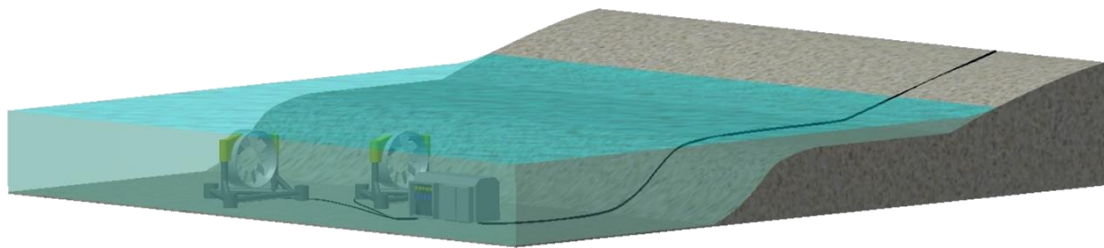


Figure 6: OpenHydro tidal turbine system

2.1.2. The power coefficient and the tip speed ratio

The amount of available power is dependent on the tidal speed (v) as shown in Equation (1) [17], the power coefficient (C_p) is a measure of efficiency of the conversion of tidal energy to mechanical energy. The power coefficient is dependent on the tip speed ratio (λ) Figure 7 is a typical power coefficient curve from [18] and shows this relationship. The power that is available for extraction is limited to 59% of the site's potential, the same as for wind turbines and is known as the Betz limit [19].

$$P = \frac{1}{2} \cdot \rho \cdot v^3 \cdot \pi \cdot R^2 \cdot C_p \quad (1)$$

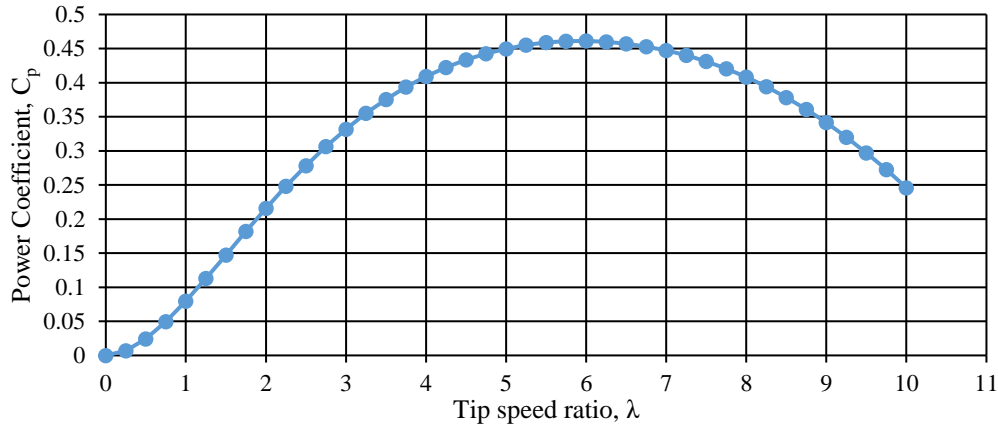


Figure 7: Typical power coefficient curve

Different power coefficient equations are presented in [18], originally these equations were determined for wind turbines from [20]. C_{p2} , C_{p3} and C_{p4} are calculated based on the blade pitch (β) which is fixed for the OpenHydro turbine. Figure 8 shows the power coefficient using the different equations for a blade pitch of 25° . C_{p5} was determined from Equation (2) presented in [1], the equation was obtained by fitting the curve of the data from a tidal turbine prototype.

$$C_{p5} = 0.01395 \cdot \lambda^2 (1.3172 \cdot e^{(-0.3958 \cdot \lambda + 1.539)} - 0.0867 \cdot \cos(0.4019 \cdot \lambda - 5.6931)) \quad (2)$$

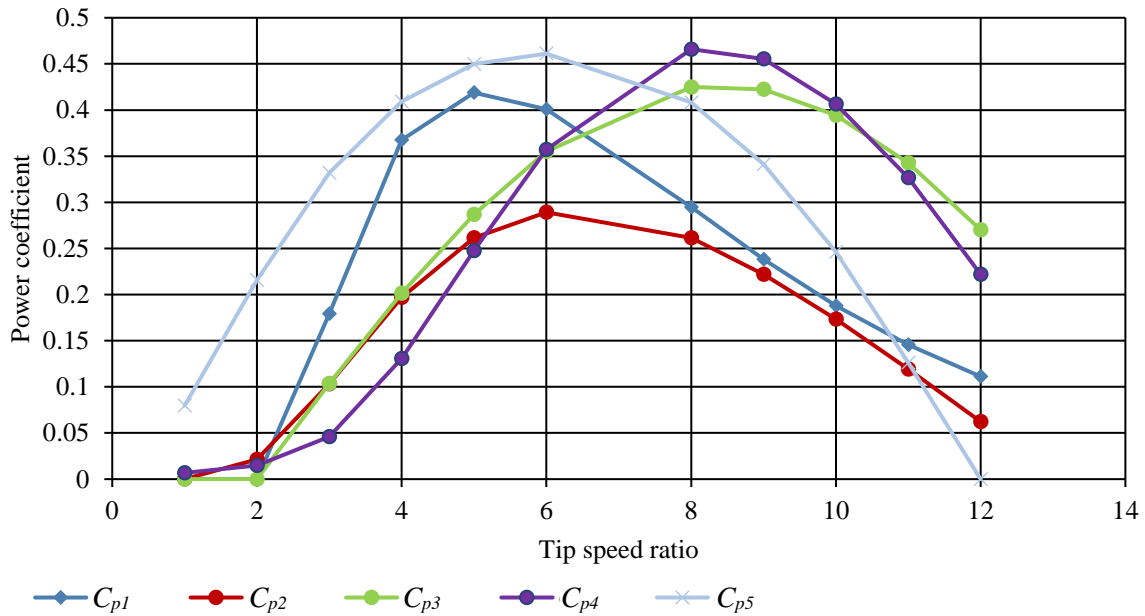


Figure 8: Different power coefficient calculations

The tip speed ratio, Equation (3) [17], is the relation of the turbine angular velocity (ω_r) and the tidal flow speed, the tip speed ratio depends on the turbine radius (R).

$$\lambda = \frac{R \cdot \omega_r}{v} \quad (3)$$

Figure 9 shows the tip speed ratio of a fixed blade turbine, this shows the cut in and cut out speeds of the turbine. The cut in speed is the speed at which the turbine losses are negligible, the cut out speed is the speed threshold at which the turbine is disabled. Speeds above the cut out threshold could potentially damage the turbine therefore the turbine is disabled to protect the generator. If the blade pitch can be adjusted then the tip speed ratio can be held constant until the nominal angular velocity after which the angular velocity is held constant and as a result the tip speed ratio decreases.

The OpenHydro turbine uses fixed blades and the tip speed ratio is variable, the simplest method of determining the power extracted is by assuming a constant power coefficient. This assumption results in an overestimation of the extracted turbine power. A constant power coefficient signifies a constant tip speed ratio. To model the variable tip speed ratio and therefore a variable power coefficient, the relationship between the tidal speed and the turbine speed was assumed to be linear. Figure 10 shows the resultant linear relationship of tidal and turbine speeds. The gradient of the line can be determined by assigning, referred to as mapping, the tidal speed to a turbine speed. The tip speed ratio and hence the corresponding turbine speeds can then be determined for all tidal speeds.

Figure 9 shows the tip speed ratio when the tidal speed 2.75 m/s was mapped to the rated turbine speed of 15 rpm, referred to as TSR_{15} . When the tidal speed 2.75 m/s was mapped to the rated turbine speed of 25 rpm the tip speed ratio was referred to as TSR_{25} . Figure 9 shows that the tip speed ratio is higher when the tidal speed 2.75 m/s is assigned to 25 rpm and this corresponds to a higher power coefficient, Figure 7.

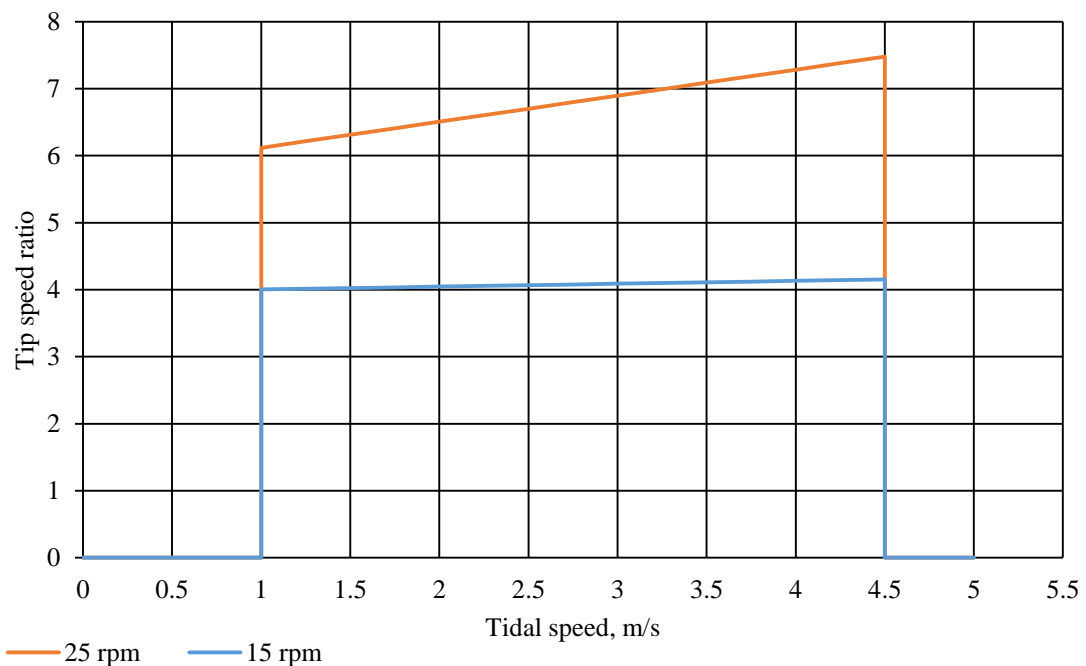


Figure 9: Tip speed ratio

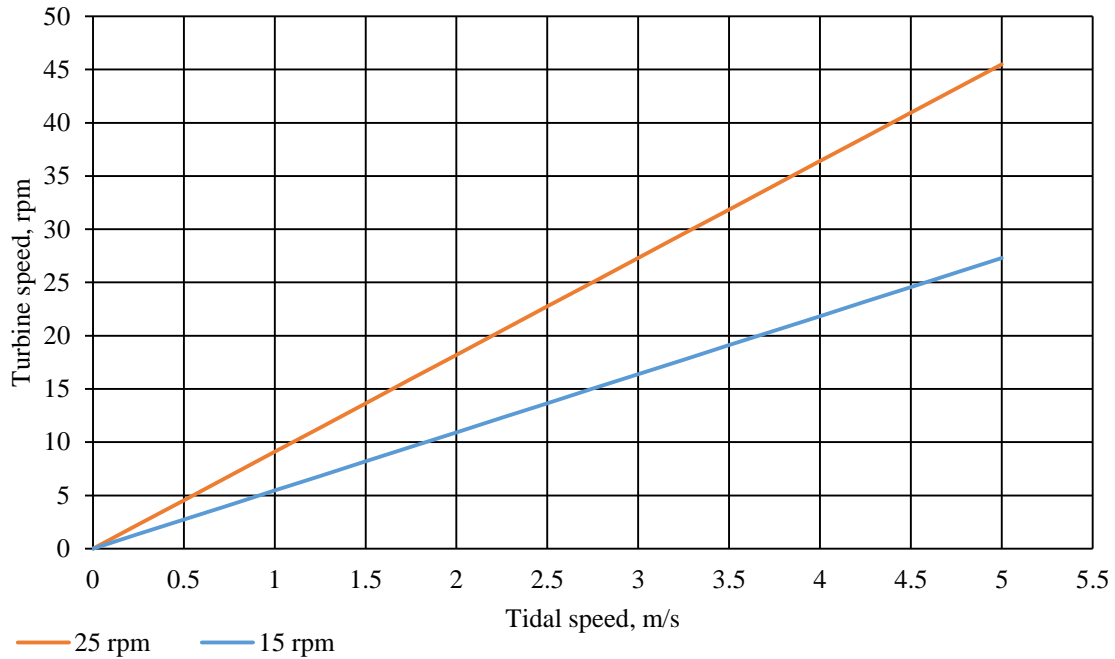


Figure 10: Linear relationship of tidal speed and turbine speed

2.1.3. Tidal power

The turbine power can be calculated using Equation (1), Figure 11 shows the calculated power of the turbine assuming a constant power coefficient and using the values from C_p5 . The extracted power is higher when assuming a constant power coefficient. The power is limited to the rated value, the graph only shows the power for positive flow speed however the turbine is bidirectional and as such generates when the tide is reversed the graph has the same shape however inverted in the Y-axis.

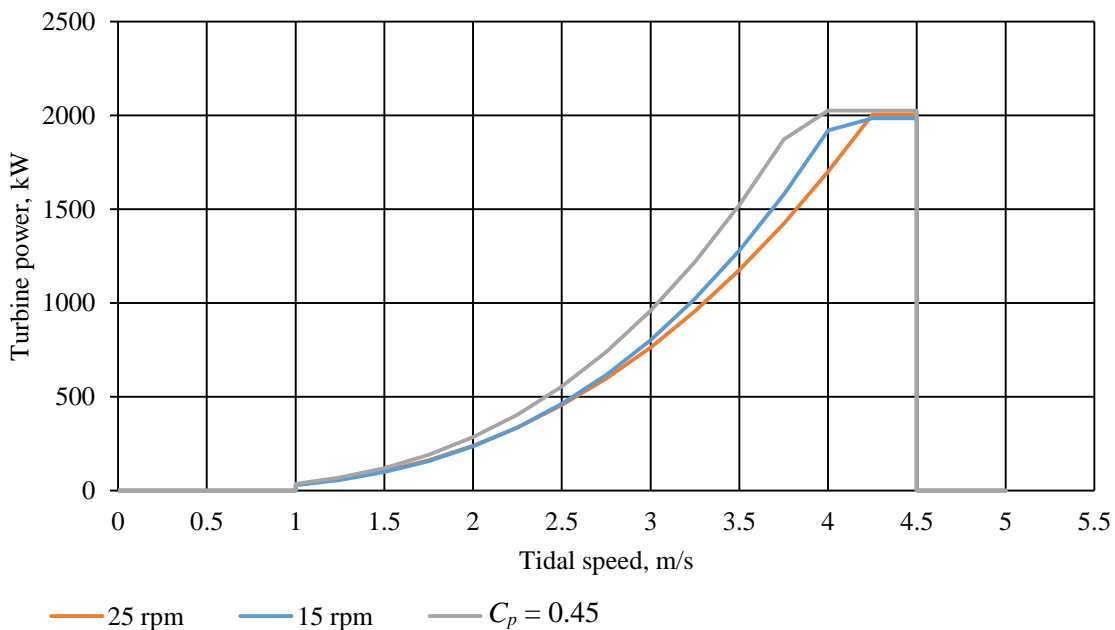


Figure 11: Marine power against tidal flow speed, with cut in and cut out speeds.

2.2. Tidal resource modelling

Tidal resource modelling is a complex process and each deployment site offers unique challenges to an MCT. The depth and bathymetry of the deployment site can affect the turbine and the turbine affects the environment. The effect of the turbines on the surrounding environment has been investigated by [13]. A deployment site will contain more than a single MCT as the turbines will be deployed in arrays similar to wind farms shown in Figure 12. The impact of a MCT on a second MCT downstream has been investigated by [13], it was concluded that in a fast flowing stream MCTs can be deployed closer together as the stream recovers faster.

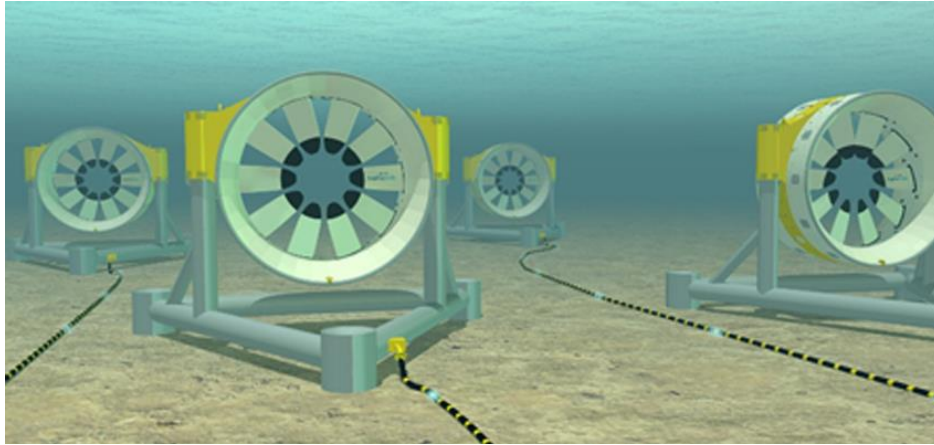


Figure 12: Tidal turbine array [21]

The tidal models are used to investigate the environmental impacts of an MCT at the deployment site, in this instance the model is used to determine the occurrences of the tidal speeds. The power generated by the turbine at each speed can be used to determine the annual tidal energy yield of the turbine. Resources such as a tidal atlas [22] provide tidal speeds for 6 hours before and 6 hours after high water. The tidal speeds are determined by the tidal height variation using the computation of rates method presented in the atlas [22]. For the purpose of comparing the generator energy yields the tidal speed variation can be modelled using Equation (4) from [23].

$$v(t) = \left(K_0 + K_1 \cdot \cos\left(\frac{2\pi t}{T_1}\right) \right) \cdot \cos\left(\frac{2\pi t}{T_0}\right) \quad (4)$$

Where K_0 is determined by the peak mean spring tidal speed and K_1 from the ratio of the peak mean spring tidal speed and the peak mean neap tidal speed. T_0 is the spring neap period, 12.4 hours, and T_1 is the tidal period, 353 hours. To compare the two methods a test site in Rosyth harbour, Figure 13 [24], was chosen, the tide height data was provided from [25] for the 12th and 13th February 2018. The data required for Equation (4) for the same site was provided by [26]. Figure 14 shows the tidal speed variation over 24 hours at the Rosyth site for both methods.



Figure 13: Rosyth harbour site

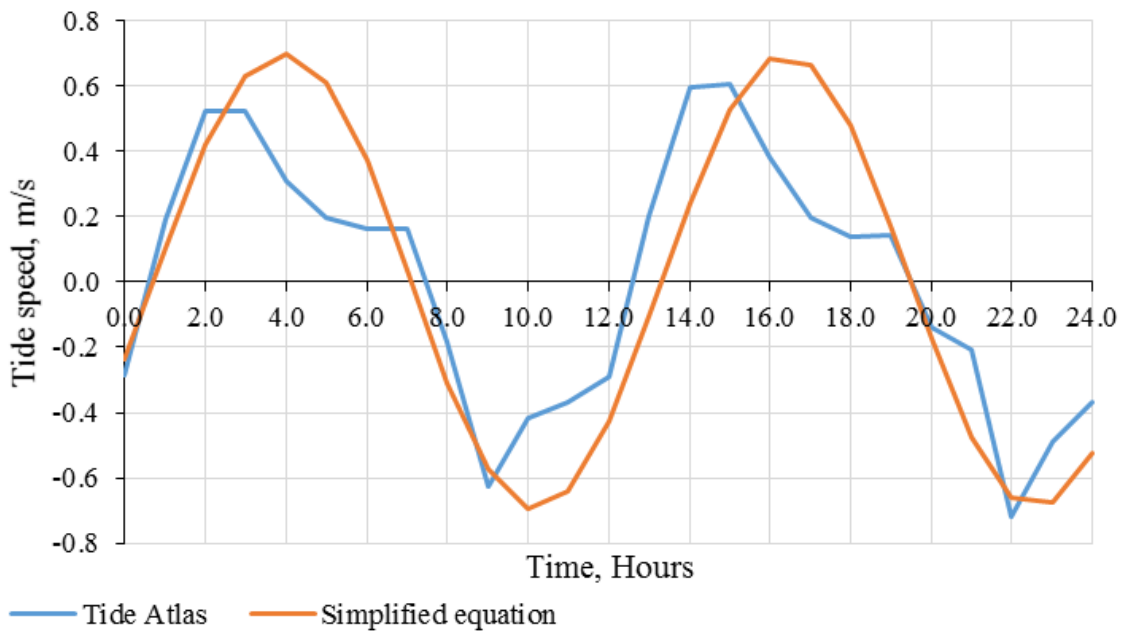


Figure 14: Comparison of tidal speed based on the tidal atlas and from the equation

The equation assumes a perfectly sinusoidal variation in tidal speed, however the tidal atlas data in Figure 14 shows that the tidal speed variation is distorted. The frequency of the tidal speed from the tide atlas is variable whereas the equation assumes a fixed frequency. The equation is capable of providing tidal speeds for different sites and easily expanded to provide data for any time periods. The tidal atlas provides an accurate tidal speed variation however the atlas is site dependent. The tidal atlas requires the site tidal height predictions to provide data for the same time periods.

2.2.1. OpenHydro site model

Figure 15 shows the global deployment sites of various OpenHydro projects, Table 1 shows the peak mean spring and neap speeds at four of these deployment sites. The Bay of Fundy off the coast of Nova Scotia and Raz Blanchard in Normandy are both deployment sites for the 16 m turbine. The Bay of Fundy is known for rapid tidal speeds appropriate for a tidal turbine, and was chosen for use as the theoretical deployment site for the designs presented in later chapters.



Figure 15: OpenHydro project deployment sites [4]

Figure 16 demonstrates a monthly semi-diurnal tide for the Bay of Fundy. The tidal speeds were calculated using the data provided in Table 1 for the Bay of Fundy [26] and Equation (4).

Table 1: OpenHydro deployment site data from the webAtlas [26]

Deployment Site	peak mean spring speed, m/s	peak mean neap speed, m/s
Raz Blanchard, Normandy	4.48	2.53
Torr head, Ireland	2.06	1.08
Eday Test Site, Orkney Island	1.49	0.83
Bay of Fundy, Nova Scotia	4	1.88

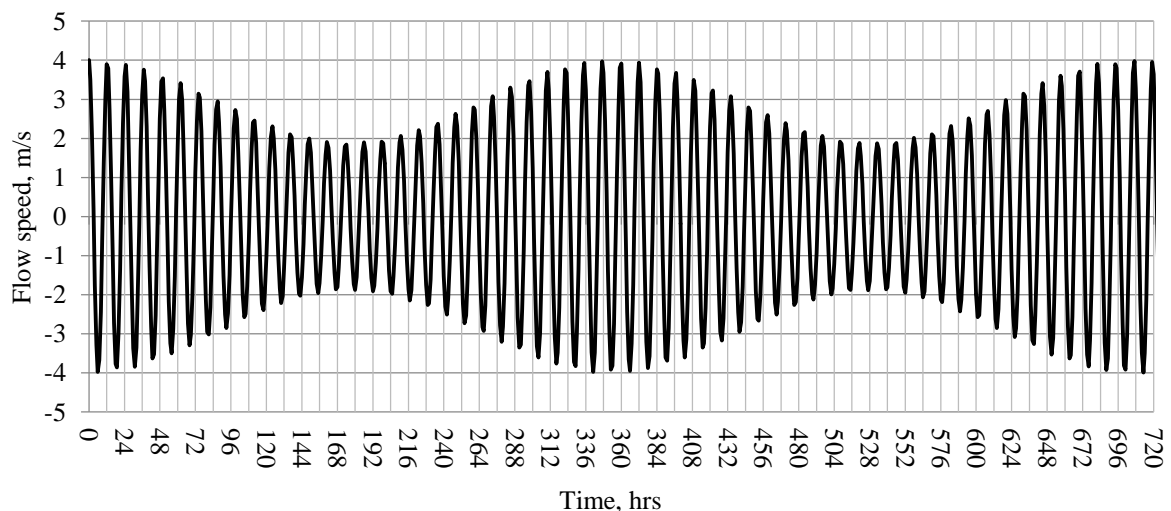


Figure 16: Model monthly semi-diurnal tide

2.2.2. Tidal speed occurrences

The tidal speed data of Figure 16 is used to determine the turbine power using Equation (1), Figure 17 shows the histogram of the tidal data. The moving average trend-line has been applied to accentuate that the majority of the hours per year are around the speed of 2.75 m/s. The high tidal speeds, 4 m/s and higher do not occur as often as tidal speeds in the range of 2.5-3 m/s. The tidal turbines of Table 2 are designed to achieve the rated performance at a speed of 3 m/s. As tidal speeds around this value occur the most often. Designing the turbine to operate at its rated value at these speeds results in the turbine generating power more efficiently than if the turbine was designed for an operational tidal speed of 4 m/s or higher.

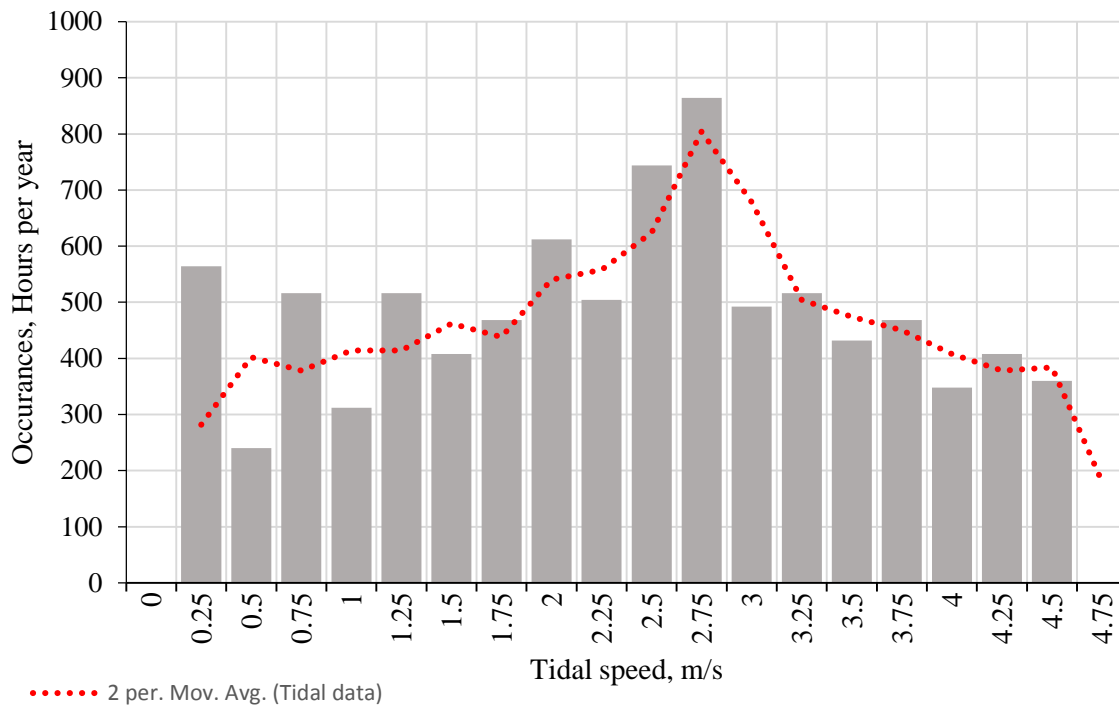


Figure 17: Histogram of tidal speed and annual occurrence

2.3. Demands on electrical machine

In some renewable energy applications, notably wind, the mass and size of the electric machine are critical – directly affecting the mechanical requirements of the supporting tower. In other generator applications, however, the turbine has to be large to capture the rated power and so arguably the torque density of the machine is less important. The diameter of the OpenHydro generator is dictated by the diameter of the blades – around 14 m for a 2 MW machine. Shear stress is used as an indication of the performance of an electric machine. The shear stress is the tangential force applied to a surface area on the rotor. The turbine has a rated torque of 1 MNm, and the active area envelope for the machine is approximately 22 m². The rated torque can therefore be reached by a shear stress of 6.5 kN/m², conventional machines typically have shear stress values of 10-40 kN/m² [27].

By designing the generator to be as mechanically robust as possible the operational periods between maintenance can be increased. The operational environment of the marine current turbine causes the maintenance and repair costs to be expensive. These costs account for approximately 15% of the cost of energy of a tidal turbine[28], therefore the ideal generator should be low maintenance and robust. This would reduce the turbine cost in the long term by reducing the number of maintenance cycles over the life of the turbine.

The machine will have to operate in an environment with powerful tides capable of not only damaging the machine, but also capable of moving the machine without proper ballast. Therefore the generator requires a base with substantial weight however this makes it difficult to transport the turbine.

2.4. Types of tidal turbines

As previously stated there are various tidal stream projects in development a few of them are presented here.

2.4.1. SeaGen-S

The SeaGen-S designed by Marine Current Turbines [29] uses two 1 MW geared squirrel cage induction generators. The turbines are mounted to a pylon and are capable of being lifted above sea level for ease of access for maintenance. With the pylon above the water the placement of the farm needs careful consideration to avoid disrupting ships.



Figure 18: SeaGen-S deployment

2.4.2. AR-1500

Designed by Atlantis [30] and constructed by Lockheed Martin, this turbine has a permanent magnet synchronous generator connected to a planetary gearbox. The turbine is secured with a gravity base, the weight of the base holds the turbine in place. This reduces site preparation and hence costs, however it complicates maintenance.



Figure 19: Submerged AR-1500

2.4.3. SR2000

Constructed by Scotrenewables [31] the SR2000 has a similar set up as the SeaGen-S with two 1 MW squirrel cage induction generators. However the turbines are connected to retractable arms, during transit the arms are positioned next to the barge. The arms can be retracted during harsh weather conditions to protect the turbines. The barge contains the turbine drive cabinets as well as monitoring equipment. The barge is held in place with tethers, with a subsea cable delivering the generated power to the grid onshore. As the barge is situated on the surface recovery of the device for maintenance is simple, the barge is untethered and the turbines are retracted then the barge can be towed to the docks.

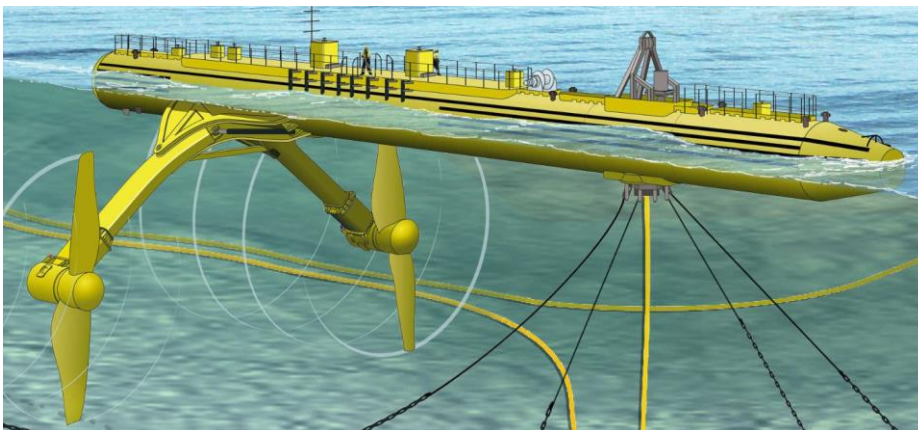


Figure 20: Deployed SR2000

2.4.4. HS1000

The HS1000 produced by ANDRITZ HYDRO Hammerfest [32] also utilises a geared 1 MW squirrel cage induction generator mounted to a gravity base similar to the AR-1500.



Figure 21: ANDRITZ HYDRO Hammerfest HS1000

2.4.5. CoRMat 500

The CoRMat 500 designed by Nautricity [33], the turbine has a double rotor axial flux permanent magnet generator. The CoRMat is a counter rotating turbine and the rotors are connected to two sets of blades with one rotor rotating clockwise and the other rotates counter clockwise. This effectively doubles the relative rotational speed of the turbine without requiring a gearbox [34].



Figure 22: CoRMat 500 being installed at EMEC

2.4.6. Comparison of the turbines

Table 2 lists the parameters of the reviewed turbines, it can be easily identified that the permanent magnet and induction machine are commonly used in tidal turbines. Both topologies are simple and robust. Another feature is that the cut in speed is 1 m/s and the rated speed is 3 m/s. In the case of the SeaGen-S and the SR2000 only the data for a single generator is shown. At present OpenHydro has the greatest installed capacity, however there are many projects that are planned for deployment in the future. OpenHydro has an advantage as the deployment and installation have been developed to reduce costs and time required; a turbine can be deployed to the site in two hours [4].

The electrical torque (T_e), Equation (5) [27], of a machine can be calculated based on the shear stress (σ), the active area and the radius (r). The active area is the surface area of the air gap, it is calculated based on the circumference of rotor and the axial length (l). The turbine torque (T_m), Equation (6) [17], is calculated from the fluid density (ρ), the tidal speed (v), the turbine radius (R), the power coefficient (C_p) and the tip speed ratio (λ). The ratio of the turbine and generator radius can be evaluated using Equation (7) [17] created by equating the turbine and electrical torque, where $\left(\frac{l}{r}\right)$ is referred to as the aspect ratio of the machine. E. Spooner [17] identified that a direct wind turbine designed with an aspect ratio of 0.5 results in a generator 5-10% of the turbine diameter. A direct drive tidal turbine designed with an aspect ratio of 0.5 would result in a generator diameter 25-30% of the turbine diameter. A rim generator under the same conditions as a direct drive turbine has a lower tip speed ratio and aspect ratio. However the rim generator is capable of operating with higher torque.

$$T_e = \sigma \cdot 2 \cdot \pi \cdot r^2 \cdot l \quad (5)$$

$$T_m = \frac{\rho \cdot v^2 \cdot \pi \cdot R^3 \cdot C_p}{2 \cdot \lambda} \quad (6)$$

$$\frac{r^3}{R^3} = \frac{\rho \cdot v^2 \cdot C_p}{4 \cdot \lambda \cdot \sigma \cdot \left(\frac{l}{r}\right)} \quad (7)$$

Table 2: Tidal turbines

Turbine	SeaGen-S	AR-1500	SR2000	HS1000	OpenHydro	CoRMat 500
Rated power, kW	1000	1500	1000	1000	2200	500
Turbine diameter (including blades), m	20	18	16	21	16	N/A
Direct drive or gear box	Gearbox	Gearbox	Gearbox	Gearbox	Direct drive	Direct drive
Generator	SCIG	PMSG	SCIG	SCIG	PMSG	DRAFPMG ¹
Fixed or pitched blades	Pitch	Pitch	Fixed	Pitch	Fixed	Fixed
Yaw system	No	Yes	No	Yes	No	Yes
Rated operation tidal speed, m/s	2.5	3	3	N/A	3	N/A
Cut in speed, m/s	1	1	1	N/A	1	N/A
Total installed capacity ² , kW	1200 [2]	3000 [35]	2000 [31]	3000 [35]	8250 [4]	500 [34]

1 – Double rotor axial flux permanent magnet generator;

2 – Total installed capacity including prototypes as of 09/04/2018

2.5. Electrical machines

This section reviews possible generator technologies, different electrical machines are considered for use in the tidal turbine. The advantages and disadvantages of each machine are presented in consideration of the application.

2.5.1. Squirrel cage induction generator (SCIG)

The squirrel cage induction generator has been used extensively in industry due to its simple construction and the capability to operate in extreme conditions. This generator is capable of variable speed with established control methods and when the machine is disconnected no electromotive force (EMF) is produced by the rotor which is good for fault tolerance. The synchronous speed of 8 pole SCIG at 50 Hz is 750 rpm and 3000 rpm for a 2 pole SCIG. For a synchronous speed of 30 rpm the SCIG would require 200 poles, resulting in large outer diameter. A gearbox increases the speed allowing a readily available SCIG to be used. A gearbox requires regular maintenance and with variable speed operation the gearbox would experience additional fatigue due to the rapid changes of torque [36, pp.191]. A direct drive design for the OpenHydro turbine would result in a large machine with a large number of poles.

When connected to a fully rated inverter, as a synchronous PM machine must be, they can also operate at variable speed with established control methods at high efficiency points, Table 3. Typical air gap lengths of a SCIG are in the range of 0.5-1 mm however the OpenHydro turbine forces an air gap of 12 mm. The large air gap length requires a large magnetisation current resulting in a poor power factor, a low power factor increases the rating of the convertor and hence its costs.

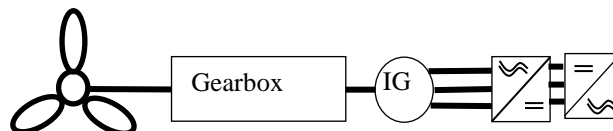


Figure 23: Connection of a conventional SCIG to the grid

Table 3: 460V, 4 pole, open frame design B performance, [37, pp. 429]

Power Rating (kW)	Nominal full load efficiencies (%)
3.7	87.5
37	93
370	95.8

2.5.2. Doubly fed induction generator (DFIG)

The doubly fed induction generator has become popular for large wind turbines due to the controllability of the rotor field current via slip rings. The armature winding is connected directly to the grid so that the speed and magnitude of the rotating field is constant. The field winding is coupled to the grid through a convertor that only requires a partial rating of the power of the machine. Variable speed is achieved by varying the rotor current frequency. The typical DFIG would require a gearbox however a direct drive

design would result in a large diameter slip ring which requires a large amount of copper. The slip rings would require regular maintenance, and would require additional copper for the slip rings for the direct drive design. The DFIG and PMSG were compared by S. Beneghali et al [38] for a geared tidal turbine, the authors built a test rig with a PMSG and a DFIG to provide practical data such as efficiency and power generated. Tidal data of a deployment site at Raz Blanchard was used to estimate the annual energy yield of each machine and concluded that annually the PMSG extracts more energy than the DFIG [38]. This conclusion neglected the impact of the rotor brushes on the maintenance of the turbine. The lifetime cost of replacing the brushes can heavily outweigh the initial cost of a fully rated convertor for a SCIG.

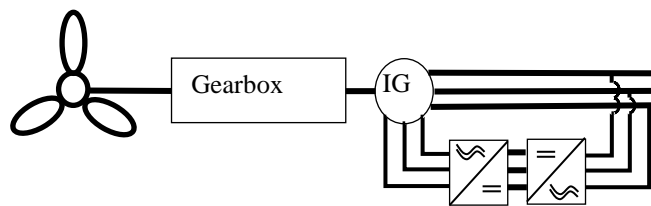


Figure 24: Grid connection of a typical DFIG

2.5.3. Brushless doubly fed induction generator (BDFIG)

The BDFIG has the controllability of the DFIG without the disadvantage of slip rings. The BDFIG has two sets of windings, both situated on the stator with a normal cage rotor. The rotor magnetic field is controlled by the second set of windings on the stator. The winding responsible for controlling the rotor magnetic field is connected to the grid via a partially rated power convertor. The winding responsible for the rotating magnetic field is connected directly to the grid. The avoidance of the slip rings lowers the maintenance requirements of the machine. The machine has a complex design, structure and operation. This would affect the implementation of the machine as a marine current turbine but remains a valid option for this application.

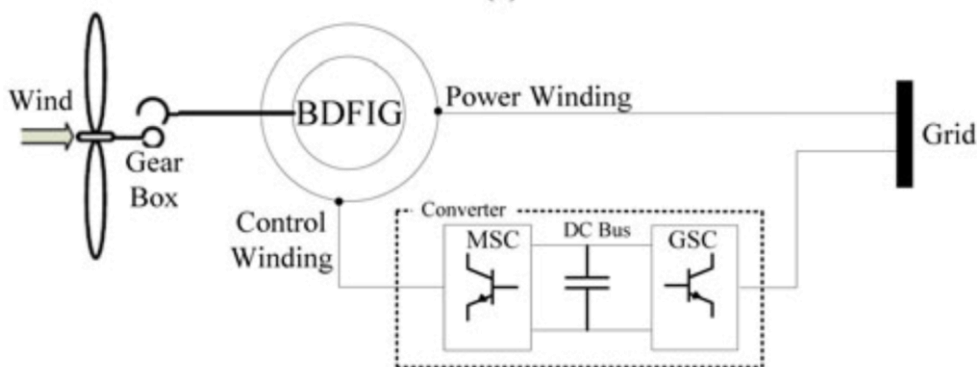


Figure 25: Connection of the BDFIG to the grid [39]

2.5.4. Wound field synchronous generator (WFSG)

The WFSG operates with a rotating magnetic field from the armature winding, this AC excitation is provided by the grid via a fully rated power converter for variable speed operation. The field winding requires DC excitation to create the magnetic field that interacts with the rotating field. The DC excitation is provided via carbon brushes and a commutator, these brushes need to be regularly checked and maintained similar to the slip rings of the DFIG.

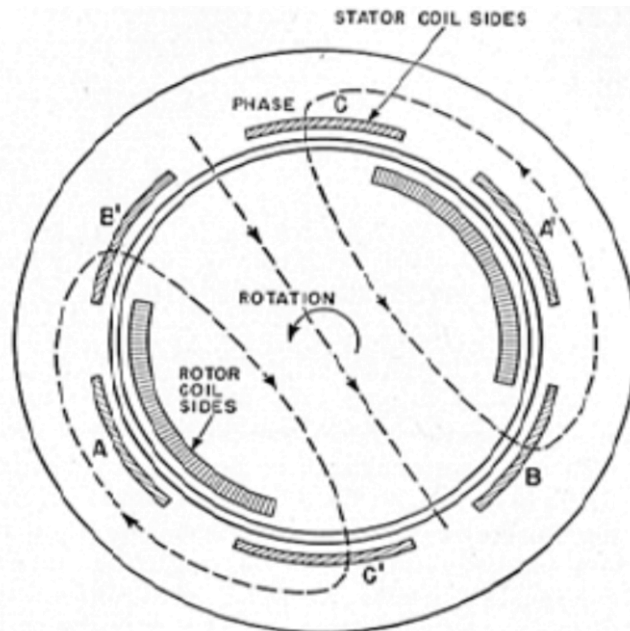


Figure 26: 2 pole wound field synchronous machine [40]

2.5.5. Permanent magnet synchronous generator (PMSG)

The operation of the PMSG is the same as the WFSG except that the field excitation is provided by permanent magnets. These magnets are usually of the rare earth variety due to the high remanence flux density, this type of magnets are more expensive than the ferrite counterparts. This machine is low maintenance with a simple structure that can be easily constructed. As such it has proven popular in marine current turbines, regardless of the high costs involved in the machines manufacturing.

Permanent magnet designs offer high torque density per unit volume and per unit mass. Performance is often expressed as shear stress, the force reacted per unit of air gap area, and typical air cooled machines may reach 10-20 kN/m², with PM topologies achieving in the range of 30-40 kN/m² [17]. The high remnant flux density offers a high magnetic loading, meaning the active area of the air gap, and hence total machine can be relatively small. The PMSG is also known to operate at a high efficiency [41], predominantly because there are no I²R losses associated with setting up magnetic field coils as found in other machine topologies.

Assembly and handling, especially of large machines, is challenging. The large diameter of direct drive design means that a robust mechanical structure is required to resist the large magnetic forces. The design of a axial flux rim generator identified that the turbine structural mass accounts for 80% of the

total mass [42]. The use of air-cored coils mitigates the radial attractive forces, however this increases the magnetic air gap length adversely affecting the machine's performance.

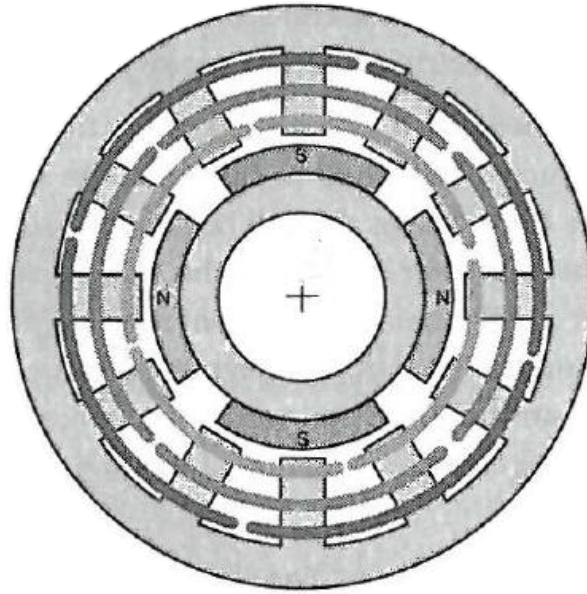


Figure 27: Permanent magnet synchronous machine [43]

2.5.6. Switched reluctance generator (SRG)

Unlike the previous machines that produce torque using the *BII* mechanism the SRG generates torque from the reluctance action of the rotor [36, pp. 320]. In the previous machines this reluctance torque is known as cogging torque, this is the reluctance of the rotor teeth to move from alignment with the stator teeth. It is a negative mechanism for other machines causing torque ripple. The rotor and stator of the SRG have saliency to align the rotor and stator. The rotor of the SRG is made of solid steel and increases the overall weight of the machine. A 20 kW SRG was constructed for use in a wind turbine that demonstrated $\approx 80\%$ efficiency for various loadings [44]. This type of machine would require additional filters in the convertor to remove the current harmonics. The harmonics would need to be removed before connecting this machine to the grid to comply with stringent grid codes.

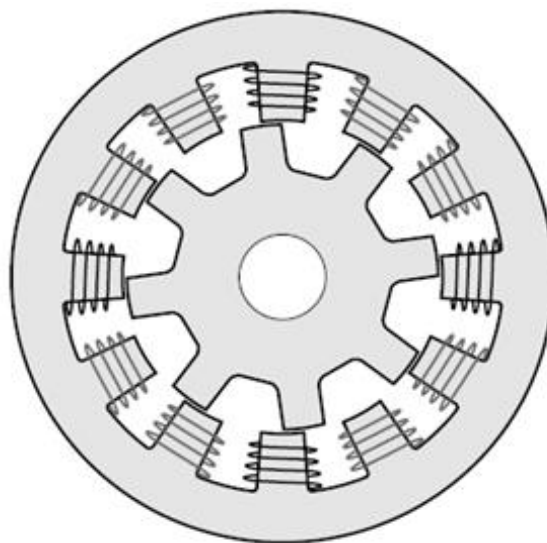


Figure 28: Switched reluctance machine [36]

2.5.7. Double stator axial flux permanent magnet generator (DSAFPMG)

The magnets of this machine are polarised in the axial direction of the machine rather than radial. This design utilises a second stator with the rotor positioned between the two stators. The attractive forces are balanced and thus reduces the wear on the bearings [43, pp.122]. The use of a double stator helps reduce the mechanical stress on the rotor and it also improves the fault tolerance of the machine, as should one stator fail the machine can still operate at half the rated performance[45]. The machine requires a large radius or a large number of poles otherwise the length of the end windings can be greater than the slot length resulting in poor utilisation of the windings [43, pp.123]. As a direct drive generator typically has a large diameter and a substantial number of poles this should not be an issue for the application of a marine current turbine. However it is noted that the stator laminations are packed in a circumferential direction increasing the difficulty of manufacturing [43, pp. 123]. This limits the practicality of this type of machine, as the purpose of this project is to design a machine that is capable of extracting tidal energy economically.

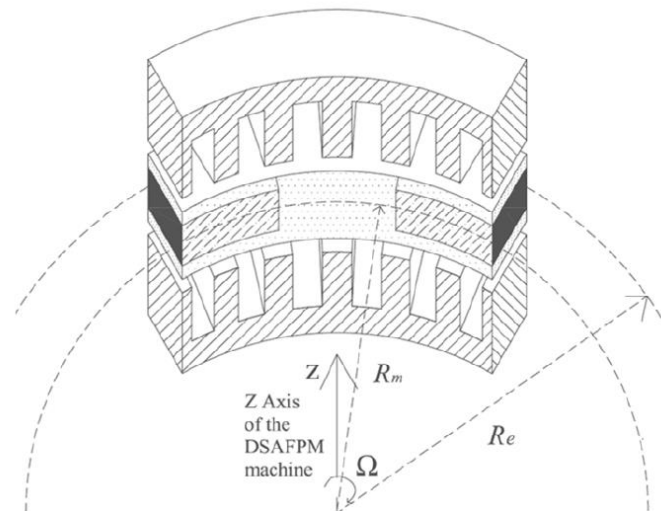


Figure 29: Double stator axial flux permanent magnet generator [45]

2.5.8. Transverse flux generator (TFG)

Transverse flux machines are known to have high torque densities implying this topology may achieve the desired performance using less magnet material. Transverse flux machines generally use radial magnets with an axial path in the stator. The TFG has hoop windings around the stator periphery this results in a large self-inductance. As a consequence the TFG suffers from poor power factor typically in the range of 0.35-0.55 [46], this has to be compensated by the convertor.

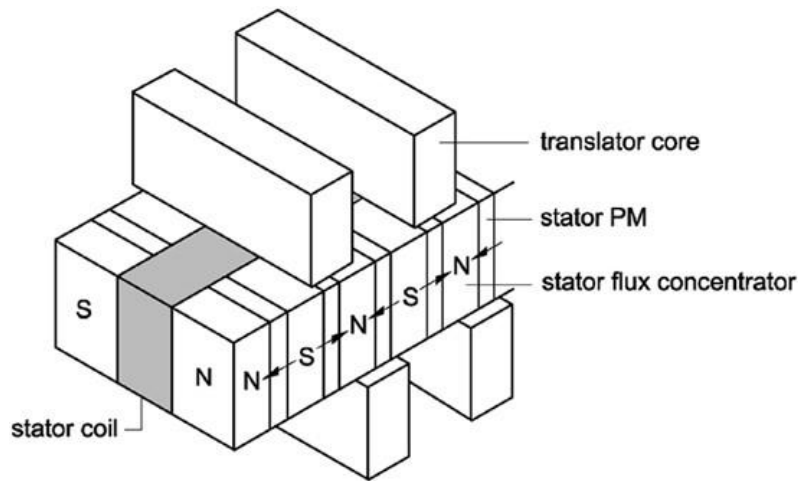


Figure 30: Transverse flux machine [47]

2.5.9. Claw pole generator (CPG)

There are two types of claw pole machine: stator claw pole and the rotor claw pole. The stator claw pole has the claws on the stator with hoop coils and radial magnets. The rotor claw pole has the claws located on the rotor with axial magnets and a standard stator. The stator claw pole, Figure 31a, suffers from low power factor due to the hoop coils. The rotor claw pole, Figure 31b, shows an advantage of the claws being located on the rotor as the rotor can be used with a conventional stator design. The number of poles is dependent on the number of claws.

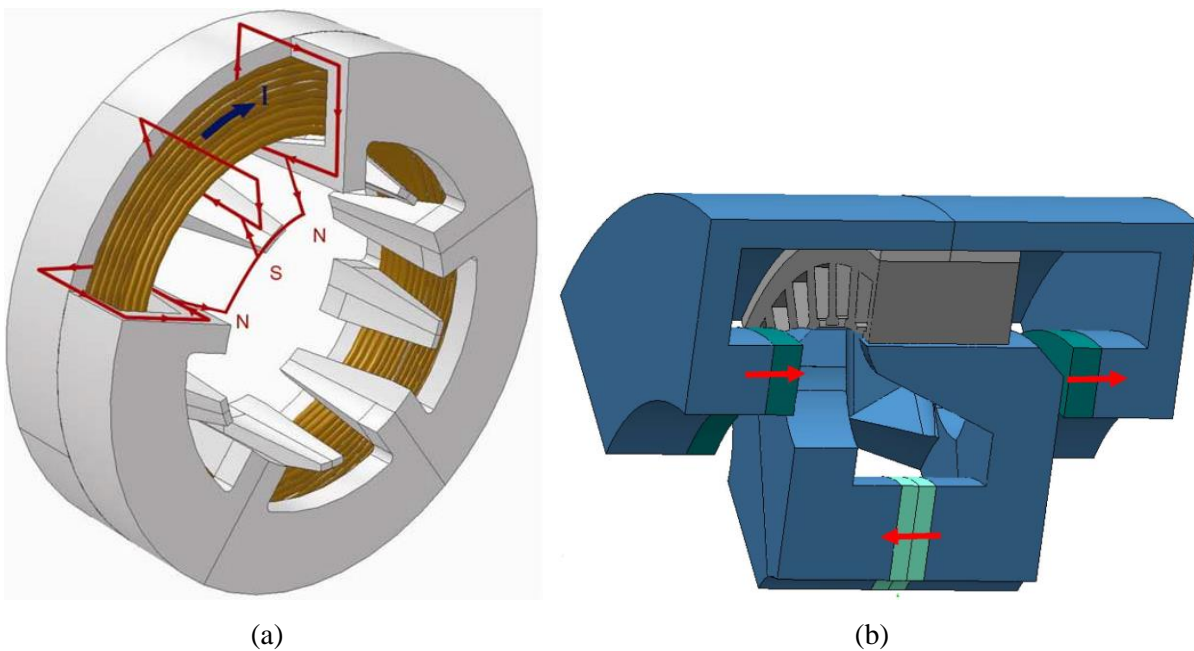


Figure 31: (a) Stator claw pole [48]; (b) Rotor claw pole [49]

2.6. Discussion of electrical machines

The uncertainty surrounding the market price of the rare earth materials has many companies considering different topologies of machine to avoid the associated risk of rare earth materials. Although the price seems to have stabilised the unpredicted spike in rare earth materials market prices has unsettled many consumers. The prospect of new rare earth mines in Greenland and Canada has contributed to alleviating the concerns of wary consumers. This provides a consistent supply of rare earth materials with a stable market price, the cost of construction of a PMSG is the same regardless of the time of its construction. The permanent magnet machine and the induction machine are two extremes of magnet content for this application and there is precedence of using a SCIG in tidal turbines albeit with a gearbox.

The size of the flooded gap between the rotor and stator in the OpenHydro turbine, which is large due to mechanical constraints, is a concern in this application. The air gap increases the leakage inductance thereby decreasing the power factor of the generator. To compensate, an over rated convertor is required. Overall, for the induction machine design to be competitive with the existing PMSG, it needs to have a lower manufacturing cost as well as competing on physical size and efficiency.

2.7. Summary

The chapter has reviewed other tidal turbine projects, where a trend toward permanent magnet and induction machines was observed. Comparing the various machine types, the squirrel cage induction generator was chosen as the alternative to the existing permanent magnet design. Due to the simple and robust nature of the squirrel cage induction generator.

The challenges that tidal turbines face were introduced, the high deployment costs are independent of the generator design and can only be reduced by optimisation of the deployment method. However the manufacturing costs of the turbine can be reduced by optimising the generator, reducing the quantity of materials used. The manufacturing and assembly process can be simplified, and the associated costs reduced, by designing the generator with a simple topology. The design has to be fault tolerant and variable speed to operate in rough conditions.

The deployment site determines the potential available power for extraction and some of the OpenHydro deployment sites were assessed using the web atlas. To determine the extractable power the tidal cycle for a site is necessary, tidal models vary from simple to complex and a simple method was chosen for use in Chapter 6. This method assumes that the semi-diurnal tide is symmetrical with the same peak spring speed.

Chapter 3. Permanent magnet machine

The aim of this chapter is to describe the existing topology and provide an optimised design for comparison with a squirrel cage induction generator. As such a general description of the electrical machine currently used is presented. A finite element model is introduced and used to optimise the design in terms of magnet mass and performance.

3.1. The existing permanent magnet design

The initial model provided by OpenHydro demonstrated that the generator consists of 72 stator segments and 144 rotor segments. Figure 32 shows a single stator segment and two rotor segments. Each stator segment consists of three coils with one coil per phase, the coils are air cored single tooth windings suspended in resin. The lack of stator teeth reduces the radial attractive forces as well as slot harmonics, however the resin is a barrier to good heat dissipation. The coils have poor cooling and as the coils operate in higher temperatures this corresponds to a faster degradation of winding insulation.

The magnets are surface mounted and there are 288 poles and 576 magnets in total, as each segment has 2 poles and each pole consists of 2 magnets. The magnets are axially segmented, this shortens the eddy current path reducing losses by reducing the path resistance. The axial length of the magnets is 270 mm. The magnets are also submerged in resin to protect against corrosion from contact with the flooded air gap. The resin coated magnets are covered with a nonmagnetic cover. Due to the saliency of the rotor a surface mounted permanent magnet machine has high windage losses. The cover presents a uniform surface reducing the mechanical windage losses. Table 4 contains the design parameters of the permanent magnet design.

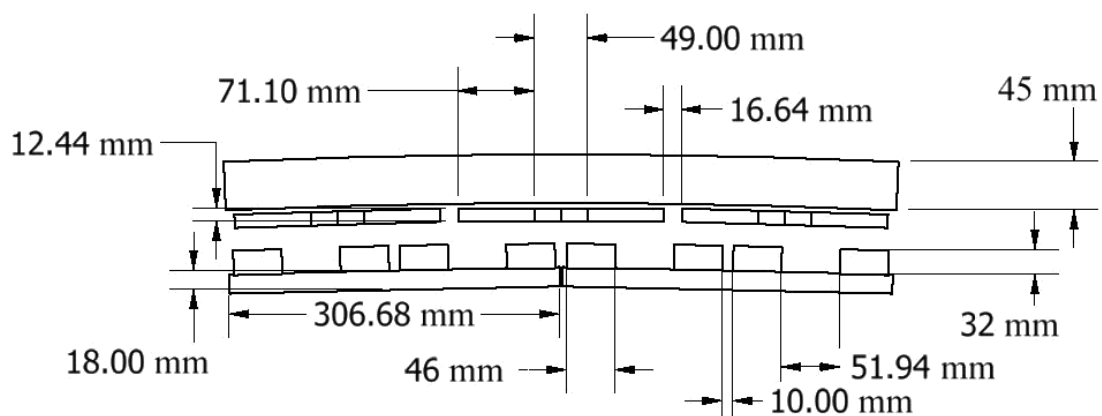


Figure 32: Single stator segment and two rotor segments

Table 4: Permanent magnet design parameters

Number of segments	72
Number of phases	3
Nominal frequency	50 Hz
Number of coils per phase	72
Winding type	Air core single tooth
Number of poles	288
Inner radius	7.136 m
Outer radius	7.260 m
Speed	25 rpm

3.2. The simplified FEA model

The initial 3D model was a mechanical CAD model and contained many features that have limited effects on the magnetic circuit. These features such as chamfers and bolts add significant time to the solver and mesh generation. A detailed design study of the permanent magnet synchronous generator initially focused on simplifying the model. The model simplification was a continuation of the work in [15], where the authors identified a difference between the measured EMF and the EMF from the 2D finite element analysis (FEA) model. The difference was attributed to the end windings and therefore a 3D model was required for the investigation.

The authors of [15] found that removing the surrounding iron had no discernible impact on the result accuracy and concluded that there was no leakage path through the surrounding iron. Therefore the surrounding iron was removed to simplify the model and to improve the computation speed. Figure 33 shows both the full CAD model and the simplified model. The authors further demonstrated that the large scale of the generator allows a single pole pair to be modelled as linear, with little effect on the accuracy of the model.

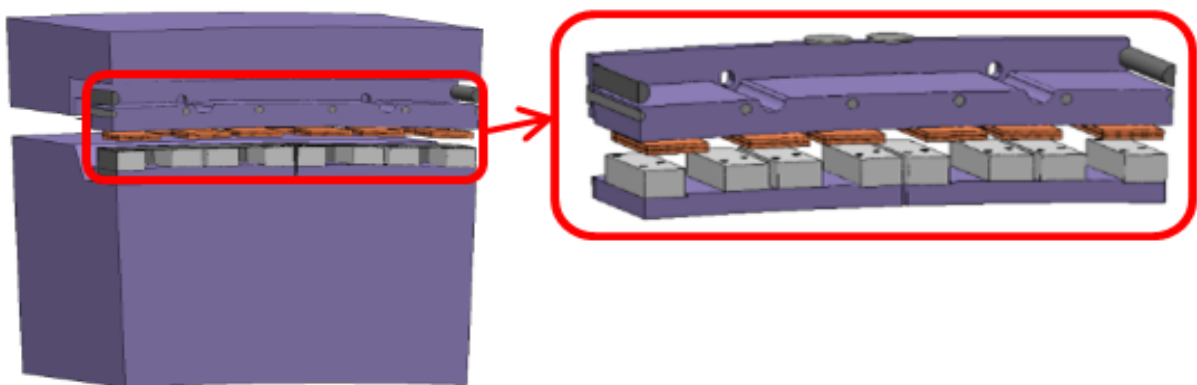


Figure 33: Simplification of the CAD model

3.2.1. Linear model validation

The model could be simplified further due to the scale of the turbine a segment could be modelled as linear. The linear model removes the unnecessary mesh from the origin point to the inner rotor radius improving the computation time, Figure 34 shows the linear model used in the study. The linear model results required validation so the results of the simplified CAD model in Figure 33 were used for comparison. The typical speed of a turbine is usually below 100 rpm [38] the rotary model was run with a synchronous speed of 25 rpm the corresponding linear speed was approximately 18 m/s. The centre coil of the simplified CAD model was used for comparison to the single coil of the linear model. The models have been constructed using the FEA software Magnet [50], and have been solved for the no-load condition.

Table 5: Model geometry parameters

Model		Linear	Simplified CAD
Number of coils		1	3
Air gap length, mm		12	12
Rotor back iron	Length, mm	450	450
	Height, mm	18	18
	Width, mm	303	303
Magnets	Length, mm	270	270
	Height, mm	32	32
	Width, mm	46	46
Coil	Length, mm	356	356
	Height, mm	12.44	12.44
	Width, mm	71.1	71.1
	Inner radius, mm	24.5	24.5
Stator core back	Length, mm	452	452
	Height, mm	45	45
	Width, mm	303	625

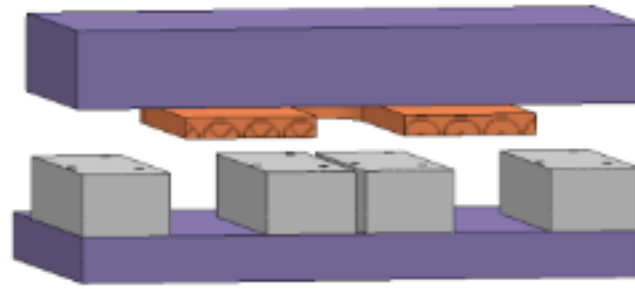


Figure 34: Linear single pole pair model

Figure 35 shows that the flux linkage from the linear model is comparable to that from the simplified CAD model. The peak flux linkage of the linear model is slightly higher believed to be caused by rounding errors when converting the model dimensions. Following the higher peak flux the linear model peak EMF, Figure 36, is also higher than from the CAD. Minor discrepancies between the model speeds exist due to truncation by the FEA software. As the EMF is the rate of change of the flux linkage with respect to time, the higher flux linkage of the linear model results in a higher EMF. The linear model reduces the complexity of the solver mesh allowing more models to be solved in a shorter time frame.

A current was applied to both models, the forces produced by the CAD model and the simplified model are shown in Figure 37. For the comparison, the force of the linear model was translated by 120° and -120° and the 3 phase forces were rectified to produce the waveform in Figure 37. The average force of the CAD model was 796 Nm and 816 Nm for the linear model, the force of the linear model is 2% higher and deemed acceptable. These results show that the linear model is suitable for use in the optimisation of the permanent magnets.

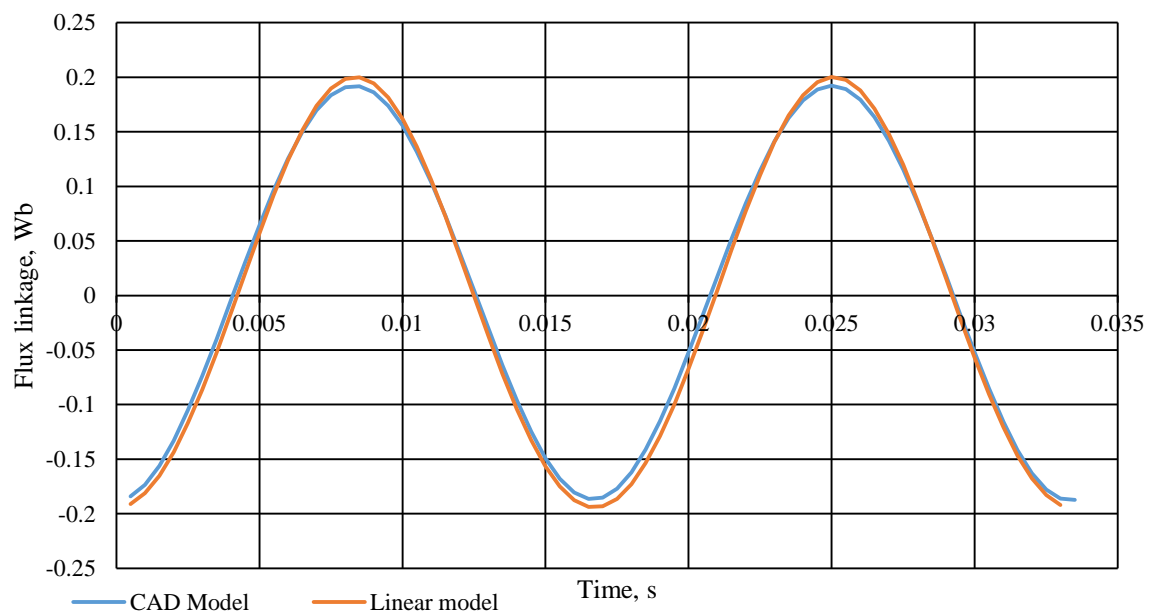


Figure 35: Flux linkage generated in the coils of both the OpenHydro model and the simplified linear model respectively

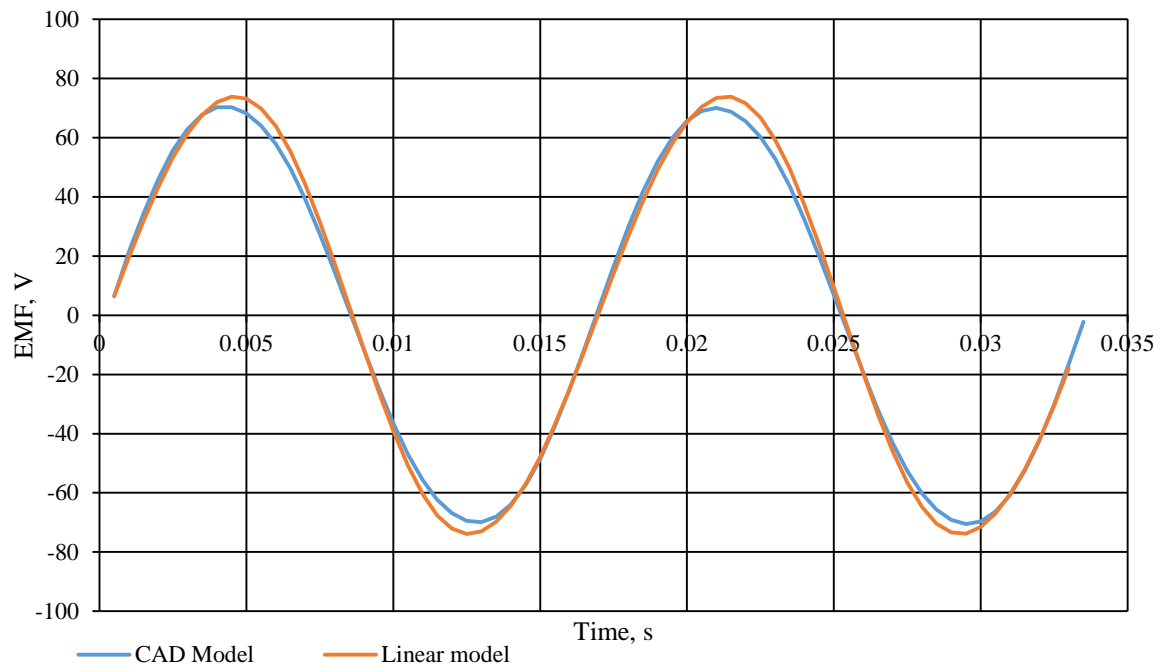


Figure 36: EMF of the CAD and simple linear model

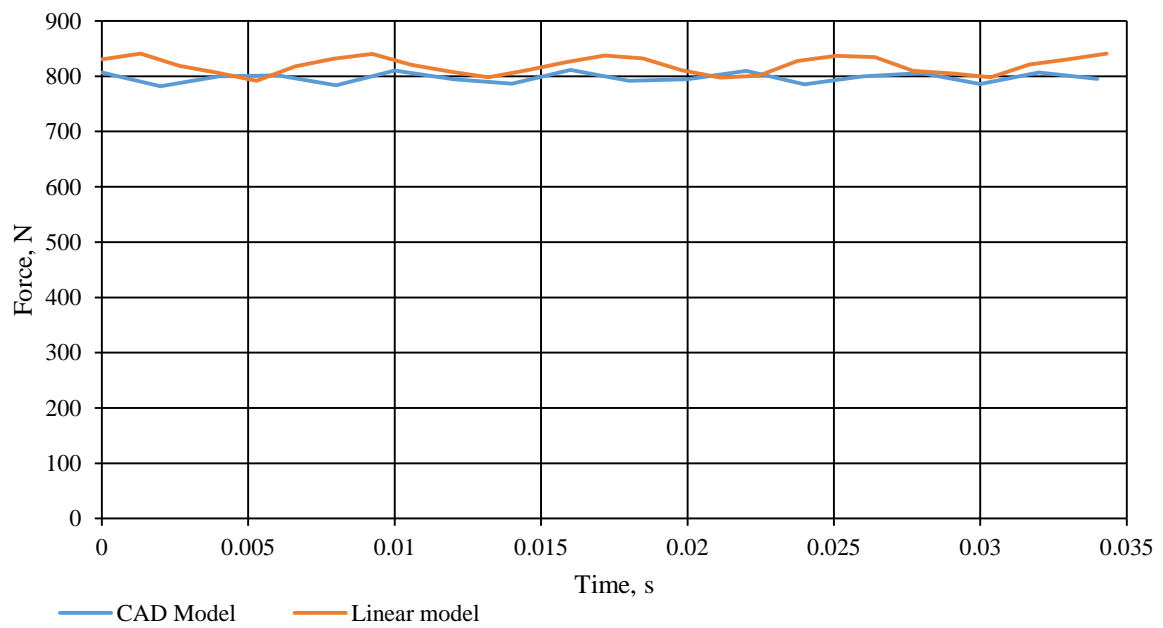


Figure 37: Force of the CAD and simplified linear model

3.3. Optimisation

The magnets constitute a large portion of the generator material costs, to reduce these costs an investigation was carried out to reduce the mass of the rare earth magnets. To provide greater accuracy a large number of models must be solved to locate an optimum point that yields a reduction in rare earth materials. This reduction should have little effect on the generator performance to be viable and therefore various combinations of the magnet dimensions were modelled. A visual basic script, constructed in the excel developer workspace, was used to create the models in the FEA software JMag.

The script that generates the combinations of magnet dimensions can be described by representing the magnet width, height and length as row vectors containing n elements. The row vector \mathbf{W} contains the width measurements, \mathbf{H} contains the height measurements and \mathbf{L} the length measurements. The dot product of these row vectors produces the 3 matrices that represent the dimension combinations for constant width \mathbf{X} , constant height \mathbf{Y} and constant length \mathbf{Z} respectively. Figure 38 shows the magnets in the model and the plane of the dimensions.

$$\begin{array}{lll} \mathbf{W} = [a_1 & \dots & a_n] & \mathbf{H} = [b_1 & \dots & b_n] & \mathbf{L} = [c_1 & \dots & c_n] \\ \mathbf{X} = \mathbf{H} \cdot \mathbf{L} & & & \mathbf{Y} = \mathbf{L}^t \cdot \mathbf{W} & & & \mathbf{Z} = \mathbf{W}^t \cdot \mathbf{H} \end{array}$$

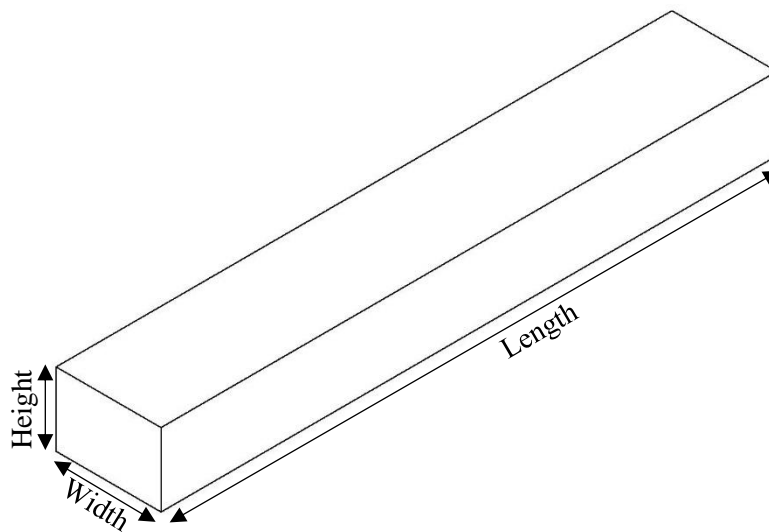


Figure 38: Magnet dimensions

3.3.1. Constraints

The average of the force in the direction of translation was used as a constraint of the studies, a force threshold was set as 95% of the average force generated by the original model. The force of the model is determined by the nodal force of the moving components, the force is for the loaded condition. Only models with a force greater than the threshold were considered. The average of the force is calculated over 6 electrical periods neglecting the first electric period, this mitigates the effects of the initial step calculations on the average force. The applied current is constant for all variations.

A 5% derating of the machine was judged to be acceptable as the turbine power was restricted to 2 MW due to the set maximum torque leaving a 0.1 MW over rating to account for abrupt speed variations. Figure 11 shows that the turbine operates at peak power at speeds of 4 m/s or higher and from Figure 17 speeds of 4 m/s or higher only occur 1116 hours per year. The derating would affect the turbine's performance for 1116 hours per year and would have minimal effect on the net income. However, the reduction of the capital costs is substantial. The decrease in capital costs increases the net income of the turbine at the end of its lifetime, and the cost of energy is dependent on the turbine's capital costs as stated in Chapter 1. To be competitive with wind and solar the cost of energy has to be reduced.

The air gap length is a physical constraint of the turbine due to the mechanical design. The 12 mm air gap is the physical distance between the rotor and stator, the magnets have a resin layer as well as a non-magnetic cover to protect the magnets from the water in the flooded air gap. The stator coils are also submerged in resin, and the effective air gap length is closer to 30 mm due to the lack of stator teeth. The model air gap length is held constant while the back iron position is adjusted to account for the magnet height variation.

The magnet width affects the spatial harmonics of the flux in the air gap, the air gap flux density of the maximum and minimum magnet width is shown in Figure 39. The fast fourier transform (FFT) of the flux densities, Figure 40, shows that the 3rd harmonics are higher for the minimum magnet width. The 3rd harmonic is a triplen harmonic, and as the turbine is a star connected 3 phase system the triplen harmonic current is only of consequence if the system becomes unbalanced. The increased fundamental of the maximum magnet width is due to the additional magnet material, as the magnet height and length were constant for the simulation.

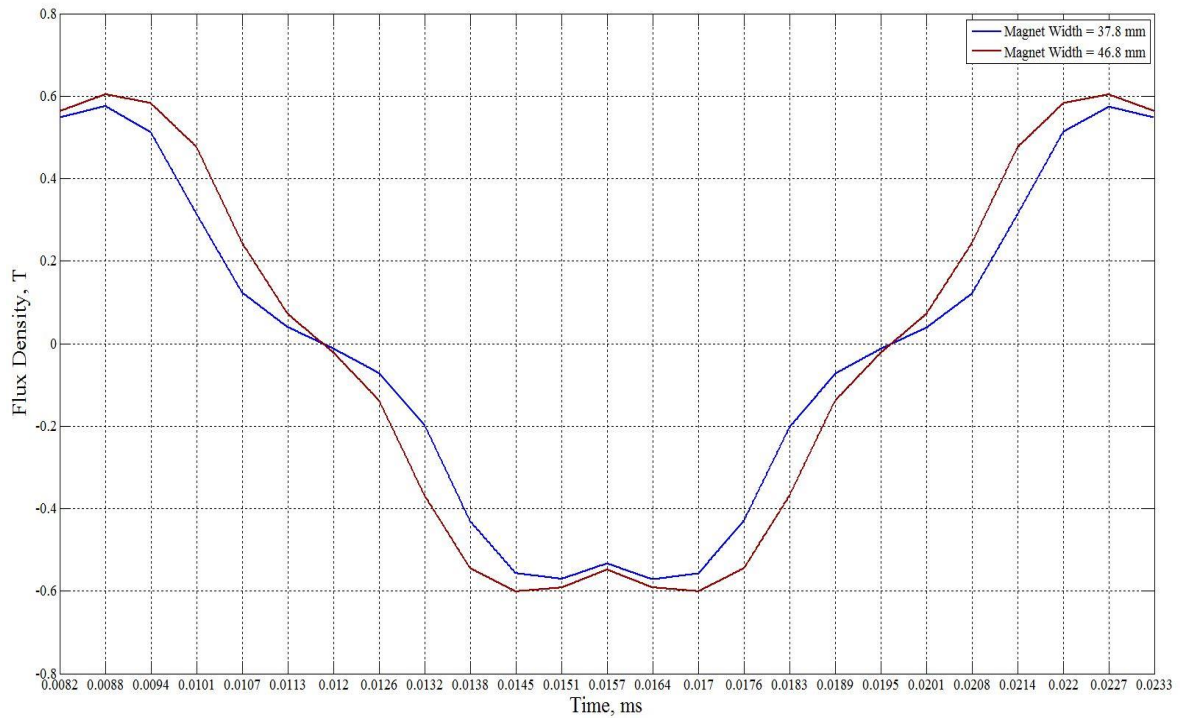


Figure 39: Air gap flux density for maximum and minimum magnet width

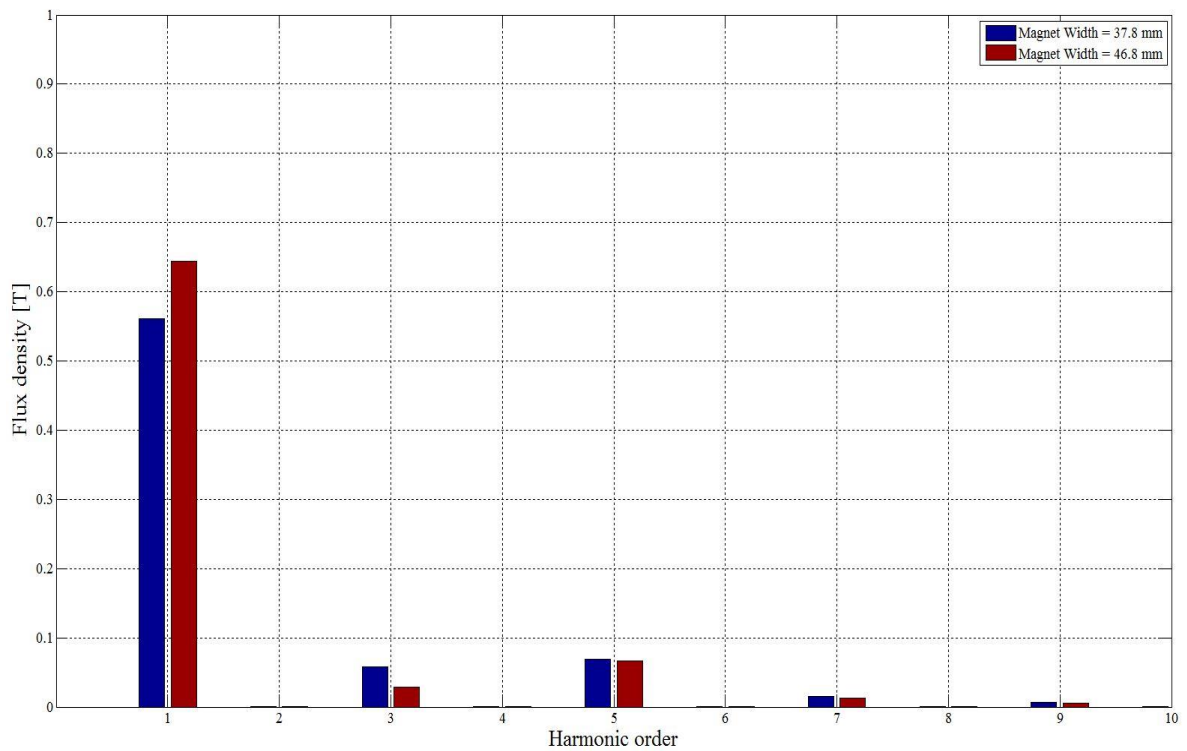


Figure 40: Harmonics of the flux densities of the maximum and minimum magnet widths

3.3.2. Coarse design study

A coarse study was used to quickly identify any optimum points that would yield a large reduction in magnet mass. The decrement in length (dZ) was set as 12 mm, and the decrements of width (dX) and height (dY) are both set as 1.8 mm. Six sets of data for each parameter were chosen as 6^3 results in 216 models. To solve a single model takes 10-15 minutes therefore to solve 216 models would require 36-54 hours, this was judged as an acceptable timeframe.

Figure 44 is the graph of constant magnet height and shows the results from the variation of the magnet width and length. The graph of constant magnet length, Figure 43, shows the resultant average force with variation of the magnet width and height. Figure 44 is the graph of constant magnet width and illustrates the variation of average force with variation of the magnet length and height.

The graph of constant height shows that the length can be reduced to a value between 135-123 mm, up to 9%, with the initial width without dropping below the force threshold. The width can be reduced to 43.2 mm, 8% of the original value, before failing to exceed the force threshold but only for the maximum length. The graph of constant length shows that the height can be reduced to 30.2 mm, up to 11.25% of the original value, and still exceed the force threshold. As before the minimum width was 43.2 mm for the maximum height and length. The graph of constant width corroborates the values of height and length from the previous graphs. Table 6 shows the best magnet dimensions from the three graphs as well as for the original magnet dimensions, PM-72-0. The table shows the calculated magnet mass and the force. Reducing the magnet height significantly reduces the magnet mass and causes a slight reduction of force.

Table 6: Magnet dimensions and mass

Design	Dimensions, mm (% of original dimensions)			Mass per magnet, kg	Force, N
	Height	Width	Length		
PM-72-0	32 (100%)	46 (100%)	270 (100%)	2.98	302.83
PM-72-1	32 (100%)	45 (98%)	270 (100%)	2.92	294
PM-72-2	30.2 (94%)	45 (98%)	270 (100%)	2.75	288
PM-72-3	28.4 (77%)	46.8(102%)	270 (100%)	2.69	289

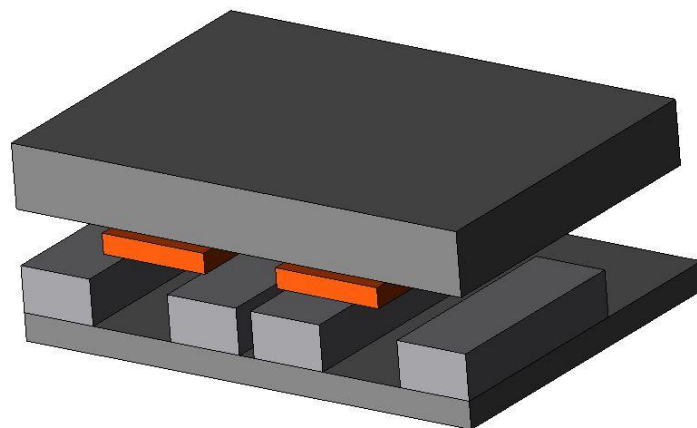


Figure 41: Initial design PM-72-3

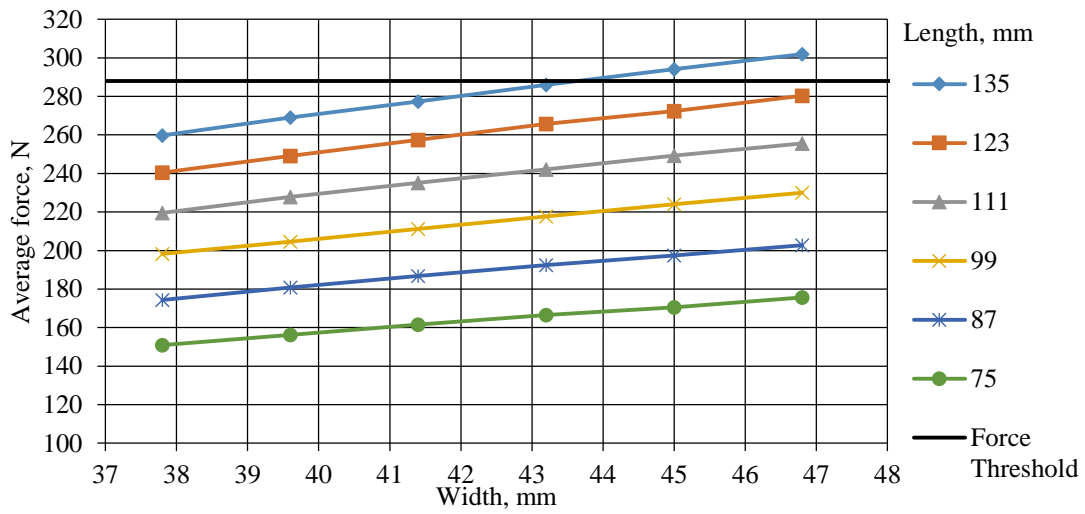


Figure 42: FEA results of the coarse design study showing variation of average force with the magnet width and length

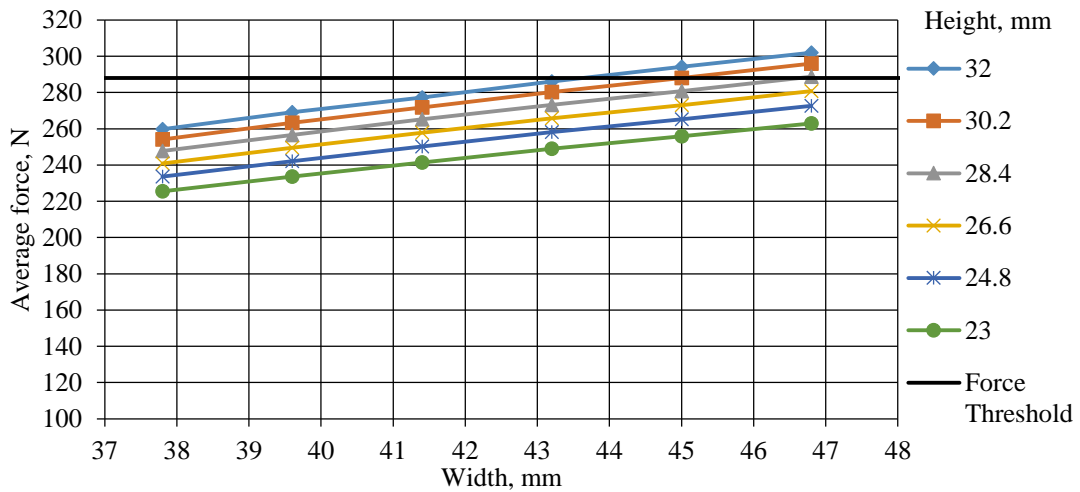


Figure 43: FEA results of the coarse design study showing variation of average force with the magnet width and height

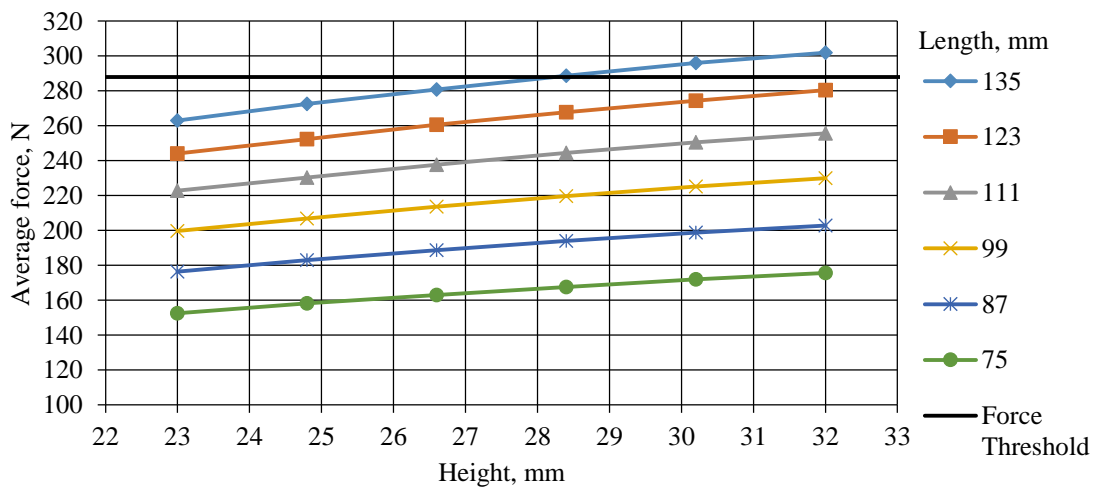


Figure 44: FEA results of the coarse design study showing variation of average force with the magnet height and length

3.3.3. Fine design study

Using the results of the previous study the range for length was set as 135-123 mm, for height 32-28.4 mm and the width was set 46.8-43 mm. The decrements were set as $dX = 0.5$ mm, $dY = 0.5$ mm and $dZ = 1.7$ mm. The number of data sets of the fine design study was increased to eight providing 512 models. Figure 46 is the graph of constant magnet height, and shows the findings of variation of the magnet width and length. Figure 47 is the graph of constant magnet length and shows the resultant average force with variation of the magnet width and height. Figure 48 is the graph of constant magnet width and illustrates the variation of average force with variation of the magnet length and height.

Table 7 shows the best magnet dimensions from the three graphs, Figure 46, Figure 47 and Figure 48, with the calculated mass. Table 7 demonstrates that a reduction in the magnet height has a more significant impact on the mass than a reduction of the length or width. Figure 45 shows the design that achieved the best magnet mass reduction, PM-72-16.

Table 7: Magnet dimensions and mass of the fine design results

Design	Dimensions, mm(% of original dimensions)			Mass per magnet,kg	Force, N
	Height	Width	Length		
PM-72-5	32 (100%)	46.3 (101%)	249.6 (92%)	2.77	288.67
PM-72-6	32 (100%)	44.8 (97%)	256.4 (95%)	2.76	289.14
PM-72-7	31.5 (98%)	46.8 (102%)	249.6 (92%)	2.76	288.99
PM-72-8	32 (100%)	43.3 (94%)	263.2 (97%)	2.74	288.71
PM-72-9	32 (100%)	43.8 (95%)	259.8 (96%)	2.73	288.00
PM-72-10	30.5 (95%)	46.8 (102%)	253 (94%)	2.71	288.96
PM-72-11	29.5 (92%)	46.8 (102%)	256.4 (95%)	2.65	288.30
PM-72-12	29 (91%)	46.8 (102%)	259.8 (96%)	2.64	289.34
PM-72-13	30 (94%)	43.3 (94%)	270 (100%)	2.63	288.00
PM-72-14	28.5 (89%)	46.8 (102%)	263.2 (97%)	2.63	290.26
PM-72-15	29.5 (92%)	43.8 (95%)	270 (100%)	2.62	288.00
PM-72-16	28.5 (89%)	44.8 (97%)	270 (100%)	2.59	288.03

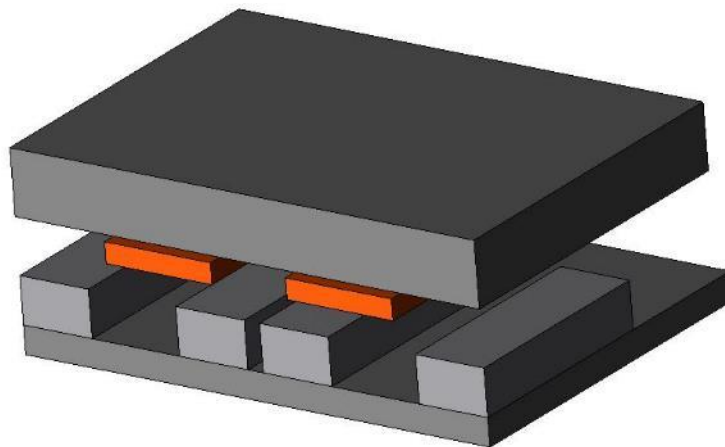


Figure 45: PM-72-16

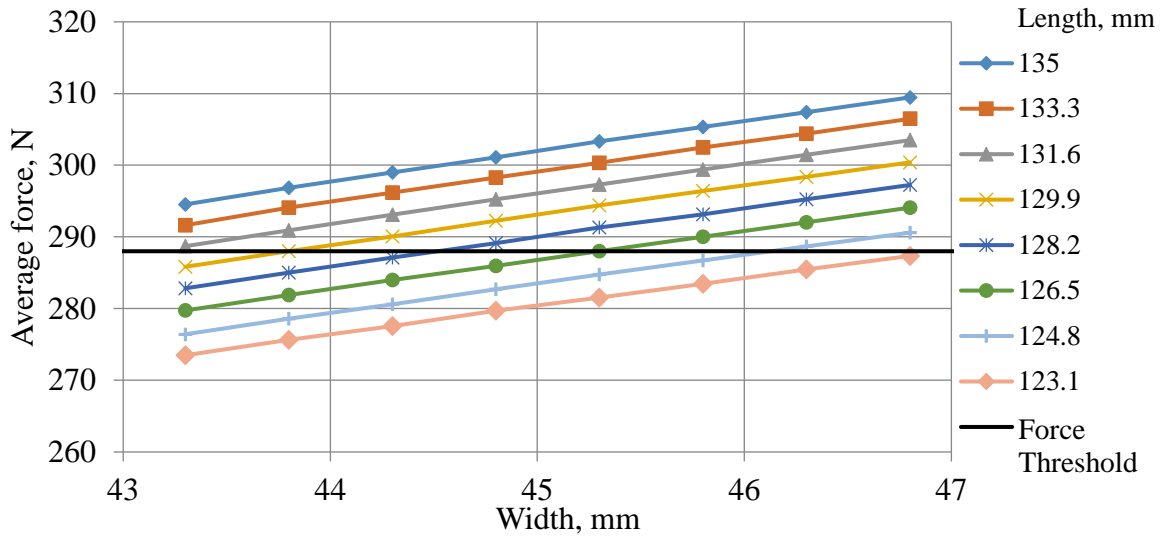


Figure 46: FEA results of the fine design study showing variation of average force with the magnet width and length

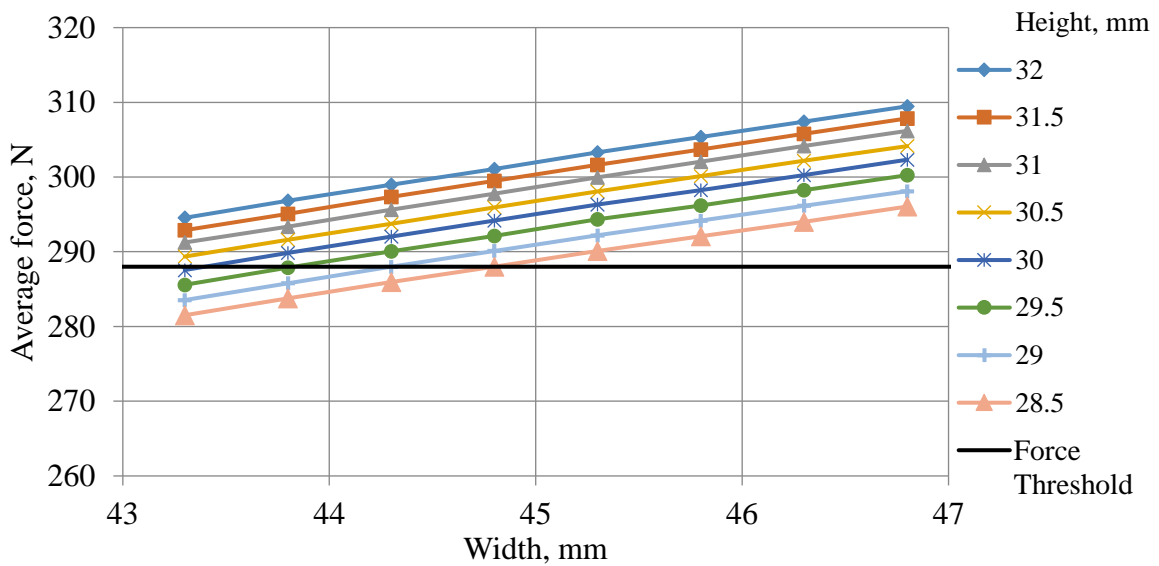


Figure 47: FEA results of the fine design study showing variation of average force with the magnet width and height

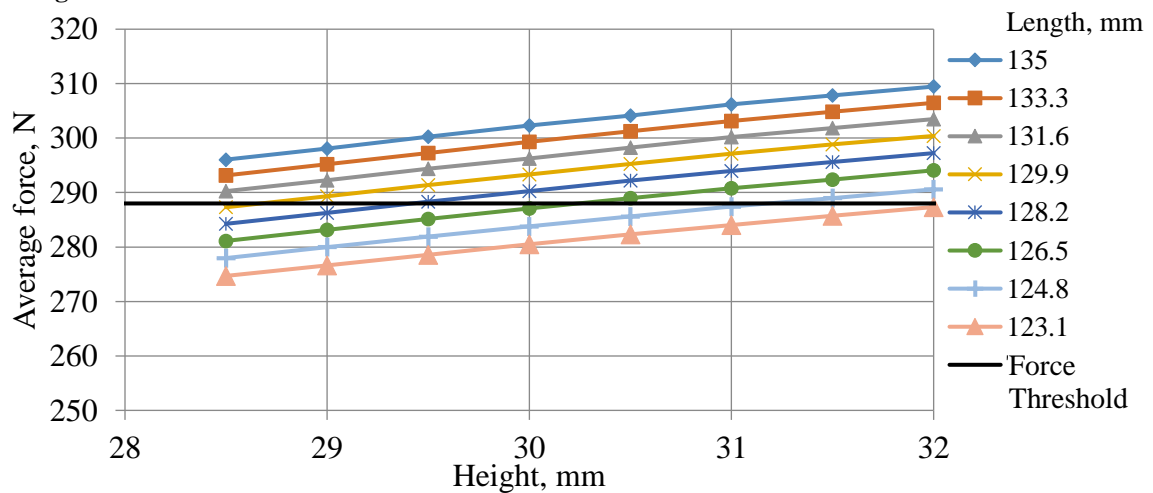


Figure 48: FEA results of the fine design study showing variation of average force with the magnet height and length

3.3.4. Numerical optimisation

A mass reduction of 13.1% was the best result of the design studies, and to identify other possible solutions the optimiser of the FEA software JMag was used. The optimiser used was a quadratic response surface model, alternatively a genetic algorithm could have been implemented. JMag creates a response surface based on the existing results, a solution that matches the objective function is then identified. Equation (8) is the second order polynomial equation from [51] for a three factor response surface. The regression coefficient β_i ($i = 1, 2, 3$) are referred to as the first order effects and the β_{ij} ($i = 1, 2, 3; j = 1, 2, 3$) terms are the second order effects.

$$\eta = \beta_0 + \beta_1 X_1 + \beta_2 X_2 + \beta_3 X_3 + \beta_{11} X_1^2 + \beta_{22} X_2^2 + \beta_{33} X_3^2 + \beta_{12} X_1 X_2 + \beta_{13} X_1 X_3 + \beta_{23} X_2 X_3 \quad (8)$$

η – Response variable

X – Input factors

β – Regression coefficient

The response data was the average force and the objective function was set to minimise the magnet mass, a constraint of average force was applied. The magnet height, width and length are the input factors. Each input factor is assigned three levels (the maximum, median and minimum of the input factor range) and a model is created for each level. The results of the model are used to determine the next input factor levels and generates the models, this process continues until the number of iterations meet the set maximum.

The constraints of the previous design studies were applied to the optimiser. The magnet height range was set as 28-33 mm, the length was set 100-140 mm and the width was 40-47 mm Figure 49 shows the results of the 200+ models. 85% of the models of Figure 49 failed to exceed the force threshold, the 15% that succeeded are shown in greater detail in Figure 50. Figure 50 highlights two models of interest, these correspond to a minimum mass compliant machine, PM-72-17, and an alternative lower mass machine achieving a smaller decrease in force, PM-72-18. These results show that the magnet mass per segment can be reduced by 11% with a decrease in force per segment of only 4%. Alternatively the magnet mass per segment can be reduced by 5.5% with only a 0.6% force reduction. The magnet dimensions of the cases are in Table 8.

Table 8: Case dimensions

Model	Dimensions, mm			Mass per magnet, kg	Average force, N
	Height	Width	Length		
PM-72-0	32	46	270	2.98	302.83
PM-72-17	28.02	45.45	277.5	2.65	291.17
PM-72-18	28.6	46.99	279.28	2.82	301

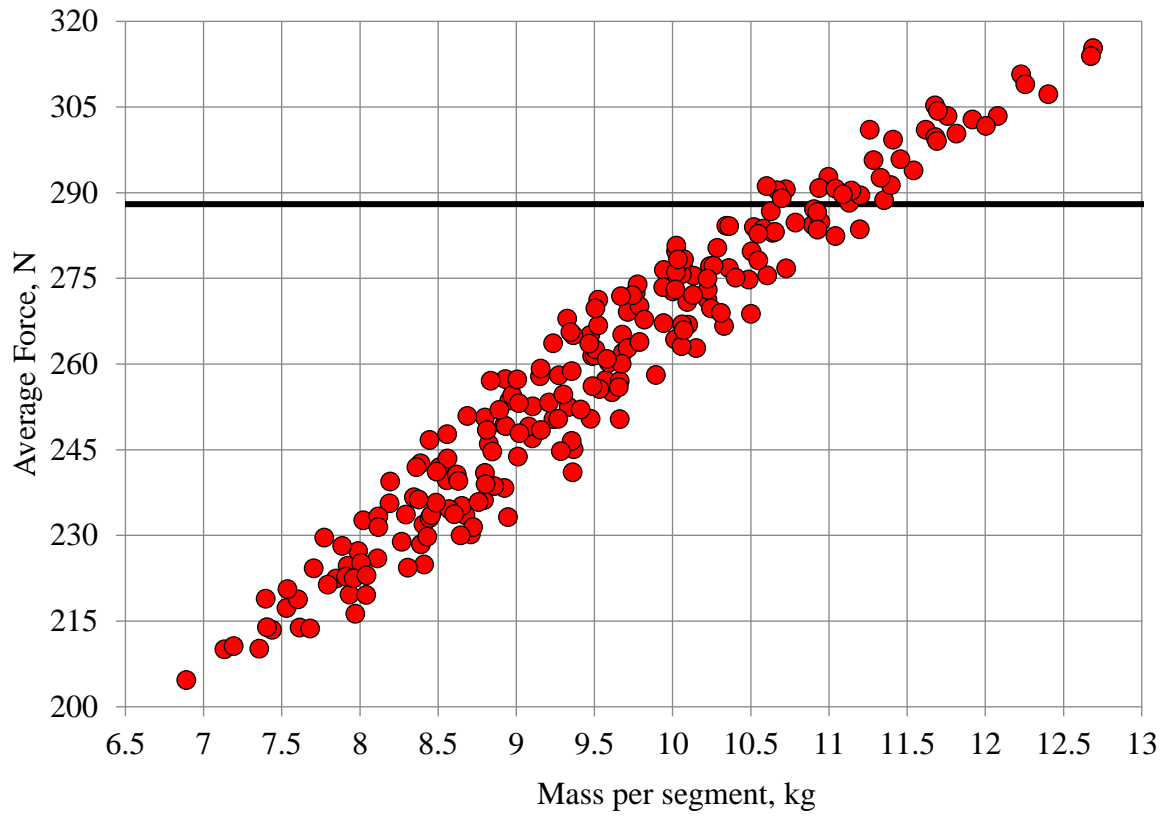
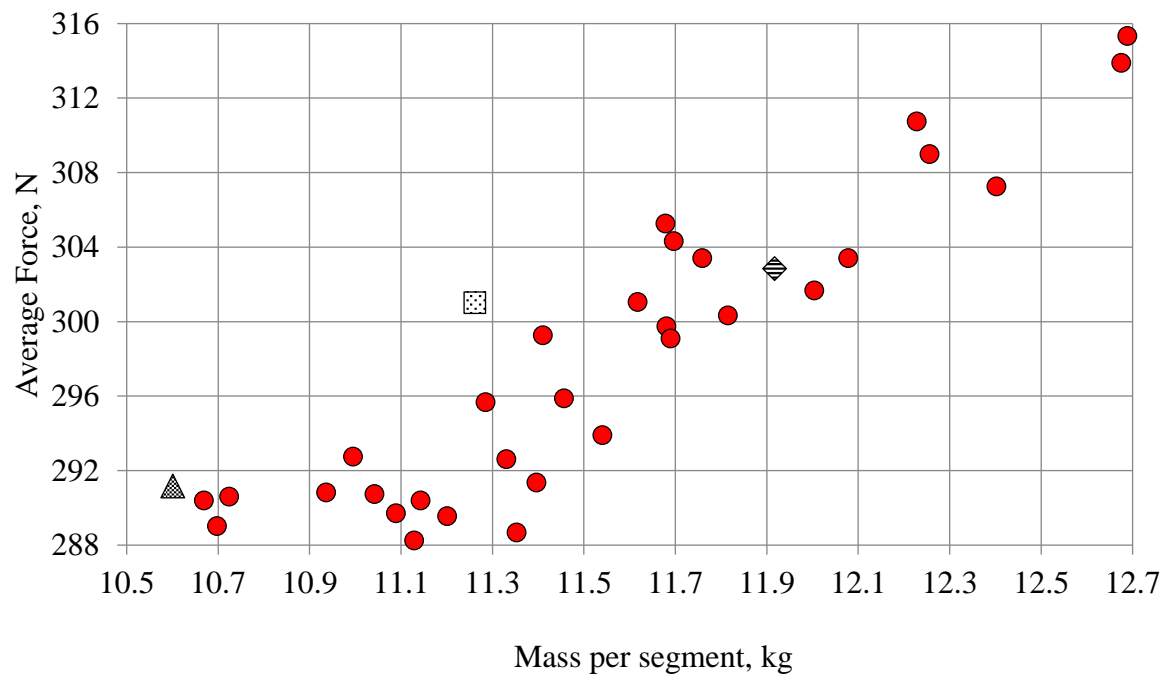


Figure 49: Optimisation results of 225 cases



- PM-72-0;
 - PM-72-17;
 - PM-72-18;
 - Other cases

Figure 50: Optimisation cases exceeding the force threshold

3.4. Power and efficiency

The efficiency and power of the generator at various speeds was required to determine the annual energy yield. A partial linear FEA model of a single stator segment and 2 rotor segments was used with boundary conditions to reduce computation time. The stator segment consists of the core back and 3 coils, 1 coil per phase, and each rotor segment has 2 poles and a back iron. The model was controlled by simple current control; i.e. a sinusoidal current to match the turbine torque. The mechanical power is the power of the turbine as presented in Figure 11 and derived from Equation (1). The efficiency is calculated from the electrical power and the mechanical power. Losses such as windage and vibration loss are neglected.

Table 9 shows the efficiencies across the turbine speed range of the original magnet dimensions and the best designs of the fine design study and the numerical optimiser. The method of calculating the turbine speed range was presented in more detail in Chapter 2. Based on a fixed tip speed ratio, the table presents the turbine speeds, power and efficiencies when the tidal speed is mapped to a rated turbine speed of 25 rpm and 15 rpm respectively (see section 2.1.2). The permanent magnet machine has a high efficiency across the turbine speed range. Table 9 shows that when the TSR_{25} is chosen the mechanical power of the turbine at 25 rpm is lower than the mechanical power than TSR_{15} .

Table 9: Efficiency vs turbine speed

Turbine speed, rpm		mechanical power, kW		Efficiency					
				PM-72-0		PM-72-16		PM-72-17	
TSR_{25}	TSR_{15}	TSR_{25}	TSR_{15}	TSR_{25}	TSR_{15}	TSR_{25}	TSR_{15}	TSR_{25}	TSR_{15}
8.18	5.35	31.27	29.01	95%	95%	95%	95%	95%	95%
10.39	6.71	60.44	56.84	96%	96%	96%	96%	96%	96%
12.66	8.07	103.28	98.51	96%	96%	96%	96%	96%	96%
15.00	9.44	162.09	156.89	96%	97%	96%	97%	96%	97%
17.40	10.82	238.98	234.88	97%	98%	96%	98%	96%	98%
19.87	12.21	335.89	335.38	97%	97%	96%	97%	97%	98%
22.40	13.60	454.57	461.35	97%	98%	96%	97%	96%	98%
25.00	15.00	596.60	615.75	97%	97%	96%	97%	96%	97%
27.66	16.41	763.36	801.58	97%	97%	96%	97%	96%	97%
30.39	17.82	956.05	1021.86	96%	97%	96%	97%	96%	97%
33.18	19.24	1175.71	1279.63	96%	97%	96%	97%	96%	97%
36.04	20.67	1423.17	1577.94	96%	97%	96%	97%	96%	97%
38.96	22.11	1699.13	1919.89	96%	97%	96%	97%	96%	97%
41.95	23.55	2004.09	1984.64	96%	97%	96%	97%	96%	97%
45.00	25.00	2004.09	1984.64	97%	97%	97%	97%	97%	97%

3.5. Selection of final machine

Both the fine design study and numerical optimiser provided a good reduction in magnetic material. The fine design study best result, PM-72-16, achieved a magnet mass reduction of 13.1% and a force reduction of 4.9%.

The FEA optimisation indicated two promising designs. One achieved a 5% magnet mass reduction with negligible effect on the force. The other had 11% magnet mass reduction for a 3.9% force reduction, and this was chosen for use in the comparison as the aim is to improve the cost effectiveness of tidal turbines by reducing the generator costs.

The design PM-72-16 from the fine design study will be used for the comparison to the induction machine design in Chapter 6.

3.6. Summary

The PMSG model has been simplified with a significant reduction in computation time by use of a linear model. This has allowed a design study to be conducted where the magnet dimensions were modified to identify an optimum magnet mass for the generator. The model current was held constant and the resultant force variation was purely due to the variation of the magnet dimensions. If a constant force was desired then the electric loading would have to increase to account for the reduction of the magnetic loading. The increase in the electric loading increases the coil ohmic losses and results in higher coil temperatures. The higher temperatures reduce the expected lifespan of the coils increasing the probability of a segment failure.

The design study identified that the magnet height could be reduced up to 11% with little effect on the average force. From the design studies a mass reduction of 13% for a force reduction of 5% was achieved by reducing the magnet height.

Chapter 4. Induction machine

The induction machine was chosen as an alternative to the permanent magnet synchronous generator for further study due to its simple and robust construction, from the literature there is precedent of its use in tidal turbines. The aim of this chapter is to design an alternative to the permanent magnet machine capable of giving the same performance in the same space envelope. This chapter introduces the design methodology, the segmentation, the design process, the limitations to the design of the OpenHydro turbine, the optimised designs and finally the optimised alternative design is presented. The fully assembled machine consists of a large number of poles due to the low turbine speed. Also the axial length is short compared to the large diameter of the machine, in typical machines the axial length is larger than the diameter.

4.1. Design specification

For the induction machine design to be comparable to the permanent magnet machine the induction machine has to fit within the same cavity. Figure 51 shows a section of the rim generator identifying the available stator and rotor volumes. The most challenging constraint is the air gap length (l_g). A large air gap length means a large stator leakage inductance, which in turn causes poor power factor resulting in higher running costs or a more expensive converter. The stator thickness (H_s) is restricted so the slots have to be designed with consideration of the core back depth. The rotor thickness (H_r) is also restricted and similarly the depth of the bars in the rotor has to be carefully considered. Table 10 lists the space envelope for the designs. The original PMSG has a power rating of 2.2 MW and treating each segment as a separate machine the segment rating is 30 kW. For the induction machine to compete the power rating has to be of the same magnitude. The rated speed of the turbine was set as 25 rpm.

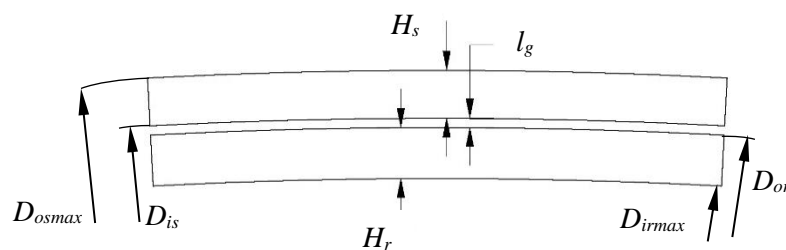


Figure 51: Section of the rim generator

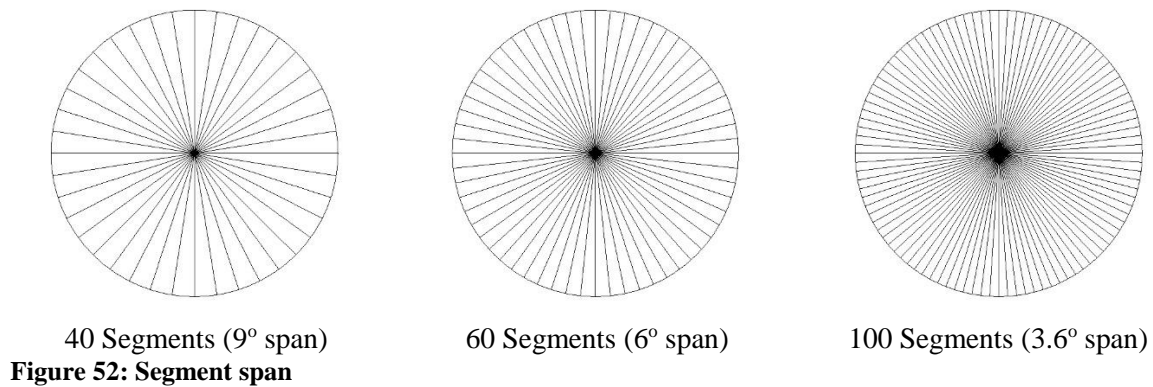
Table 10: Design parameters

Maximum axial length (L_{amax}), m	0.5
Maximum rotor inner diameter (D_{irmax}), m	14.116
Rotor outer diameter (D_{or}), m	14.248
Stator inner diameter (D_{is}), m	14.272
Maximum stator outer diameter (D_{osmax}), m	14.396

4.2. Number of segments

Similar to the permanent magnet design, the proposed induction machine was assumed to be segmented to aid the generator assembly. This introduces the segment number (S_n) as an additional variable to the design process. If the number of segments is great then each segment is relatively small and light, however this limits the design process. Whereas a small number of segments constitutes a large heavy segment, this increases the difficulty of assembly as a large segment increases the amount of design choices, e.g. the number of slots. This can either be utilised to increase the number of poles per segment or increase the number of slots per pole per phase.

To determine the optimal number of segments three designs were created with 40, 60 and 100 segments corresponding to a segment span of 9° , 6° and 3.6° respectively. Figure 52 shows the different segment span of the different number of segments. The 60 segments was chosen as it corresponds to a segment span similar to the permanent magnet design. The 100 segments represents a high number of segments and 40 segments was chosen for the small segment number representation. The segment span and volume of the rotor and stator cavities has been calculated from Equation (9), using the parameters from Table 10. Equation (9) was derived from the equation for the area of a segment. Assuming that the available volume was filled only with steel, the mass per segment for the segment numbers are shown in Table 11. From the table the mass of the 100 segment design is less than half the mass of the 40 segment design.



$$Volume = \frac{\pi}{4 \cdot S_n} \cdot (D_{outer}^2 - D_{inner}^2) \quad (9)$$

Table 11: Segmentation mass

Number of segments	Segment span, m	Rotor segment volume, m^3	Stator segment volume, m^3	Mass per segment, kg
40	1.12	0.03676	0.03490	548.17
60	0.75	0.0245	0.02327	365.45
100	0.45	0.0147	0.01396	219.27

Axial length = 0.5 m; Steel density = 7650 kg/m^3

4.3. Modelling the segment

4.3.1. Wrapping the segment

The segment could be designed as a linear induction machine (LIM), as the large diameter of the machine results in an arc that is effectively linear, as shown in Figure 51. The design of linear induction machines includes the longitudinal and transverse end effects and the concept of goodness factor. The goodness factor of a machine is a metric developed by Eric Laithwaite [52] for assessing the machine based on the suitability for the application. Goodness factor is calculated from the machine speed, electrical circuit resistance and the magnetic circuit reluctance, a value greater than one indicates an efficient design. The longitudinal effects act at the end of the stator as the rotor moves out from under the stator the flux links to the end of the stator block. The transverse edge effect refers to the complex patterns of flux density caused by the eddy currents when the rotor width is narrow when compared to the pole pitch [53]. Wrapping the segment to form a rotary model has two key benefits, first the conventional output coefficient method can be used. Secondly MotorSolve can be used for rapid design validation, as MotorSolve can only generate rotary models. MotorSolve [54] is a software package created by Infolytica. MotorSolve is capable of building FEA models based on templates and can be used for rapid prototyping.

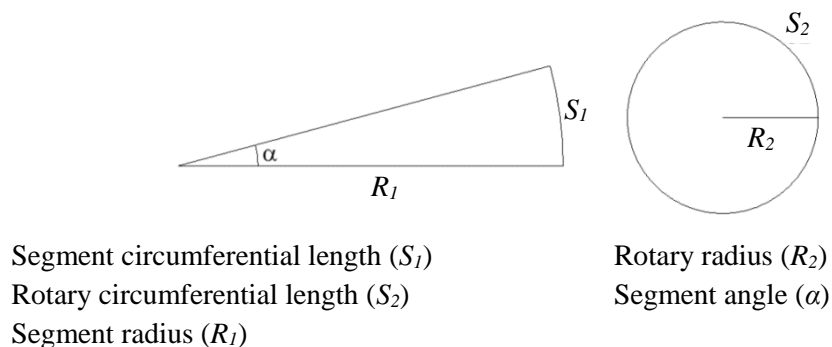


Figure 53: Equating the segment circumferential length to the rotary model

To create the rotary model from the segment, the segment arc length of the stator inner diameter was equated to the rotary model circumferential length. Figure 53 shows the parameters for determining the rotary model diameter. Equation (10) was derived by equating the circumferential lengths $S_1 = S_2$ and allows the radius R_2 to be determined. Using the stator inner diameter as presented earlier, $R_1 = 7.136$ m and α is dependent on the number of segments, 6° for the 60 segment design. Using these values $R_2 = 0.11893$ m so that the inner stator diameter of the rotary segment (D_{is}') = 0.23787 m and with l_g fixed at 0.012 m due to mechanical constraints the rotary rotor outer diameter (D_{or}') = 0.21387 m.

$$R_2 = \frac{\alpha}{360} \cdot R_1 \quad (10)$$

4.3.2. Initial design parameters

It is recommended that the value of the slot width (b_{os}) is at least three times the air gap length [37, pp. 17], to reduce the stator leakage inductance. With l_g fixed at 0.012 m by mechanical constraints the slot width needs to be greater than 0.036 m, for the same segment length this means reducing the number of stator slots (N_s). From Equation (11) [37] either the number of pole pairs (P_p), the number of slots per pole per phase (q) or the number of phases (m) can be varied to reduce N_s . The simplest solution is to reduce q to 1, however this produces a square MMF in the air gap of the machine increasing the power of the odd harmonics. Alternatively the number of phases can be reduced from 3 to 2, however control systems and drives for 3 phase systems are readily available and off the shelf. Therefore the number of pole pairs is the best option for reducing N_s , as setting $P_p = 1$ halves N_s allowing slot widths greater than 0.036 m.

$$N_s = 2 \cdot P_p \cdot q \cdot m \quad (11)$$

To determine the synchronous speed of the rotary model (ω_2) the linear speed of the segment was calculated based on the turbine speed (ω_1) resulting in Equation (12). The corresponding frequency was calculated using Equation (13) [37]. The initial parameters of the different designs are shown in Table 12.

$$\omega_2 = \omega_1 \cdot \frac{R_1}{R_2} \quad (12)$$

$$F = \frac{\omega_2 \cdot P_p}{60} \quad (13)$$

Table 12: Comparison of the complete machine to the rotary segment

Number of segments	40	60	100
Speed, rpm	996	1500	2496
Rated power , kW	55	36	22
Frequency, Hz	33.3	25	41.6
Number of poles	2	1	1
Stator inner diameter, m	0.35668	0.23787	0.14267
Rotor outer diameter, m	0.33268	0.21387	0.11867
Segment angle, degrees	9	6	3.6

4.4. Development of the analytical design model

The design process is laid out in Figure 54, the analytical design model (ADM) is a tool that uses analytical equations to aid the induction machine design based on the initial parameters. The initial designs were validated using the software MotorSolve, the optimised designs from the ADM were simulated using the FEA software JMag.

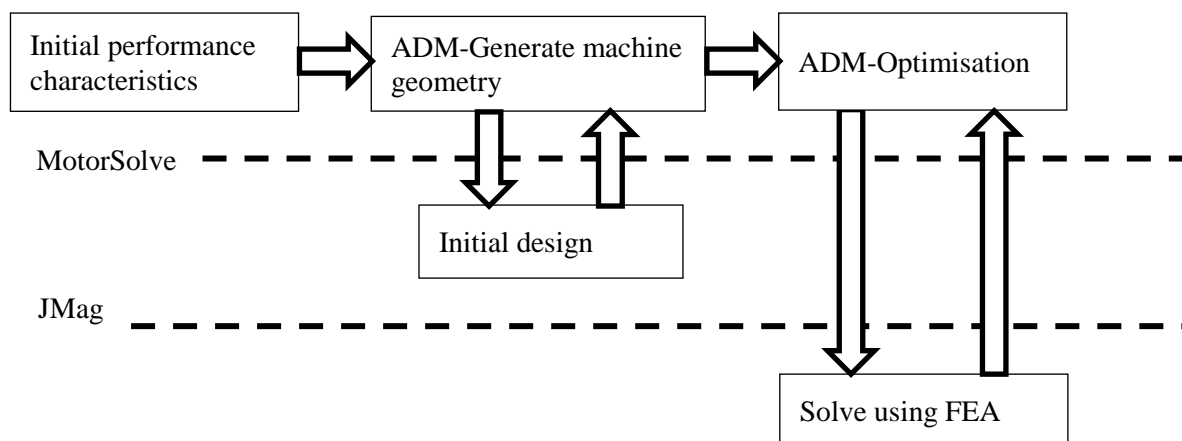


Figure 54: Design workflow

4.4.1. Output coefficient method

The method used to design the induction machine was based on that presented in [37], also found in [55, pp. 388] and [56, pp.138]. Like most machine design methodologies, it is an iterative process. The initial variables for the machine design are listed below.

Line voltage (V_{line})	Synchronous speed (n_s)
Rated power (P_n)	Supply frequency (F)
Number of phases (m)	Number of pole pairs (p_1)
Power factor ($\cos \phi$)	Phase connection, Delta or Wye
Efficiency (η)	Machine saturation factor (K_s)
Number of slots/pole/phase (q)	

Some of these have already been determined in the previous section, all three designs are 3-phase with a line voltage of 415 V. Ideally the segment design would have efficiency greater than 90%, however with an air gap length of 12 mm a target efficiency of 80% was more appropriate. It was decided that the power factor would be sacrificed to achieve a higher efficiency, with the knowledge that a converter would be used to control the machine and provide power factor correction. During the design process efforts were made to prevent the power factor from becoming less than 0.5, as the rating and therefore the cost of the convertor is inversely proportional to the power factor.

4.4.2. Saturation factor estimation

The saturation factor can be broken into two key components: the tooth saturation factor (K_{ts}) and the core back saturation factor (K_{cs}). These are numerical values that represent the degree of saturation in the teeth and core back respectively. The most important of these values is K_{ts} as it is used in the initial stages of the design and affects the overall design. No guidance for estimating K_{ts} is provided in [37], so a method was developed to provide an estimate from the maximum flux densities of the rotor and stator teeth. These parameters are selected and used at a later stage in the design method. The tooth flux density is used as a basis for estimating K_{ts} . K_{ts} can be broken into two terms: the stator tooth saturation factor (K_{tss}) and the rotor tooth saturation factor (K_{tsr}).

The method proposed here is based on the difference between the magnetic energy (E_M) and co-energy (E_C) as a measure of saturation of the machine. When operating within the linear region of the material the magnetic energy and co-energy are effectively equal. However as the material saturates and operational point moves into the non-linear region the energies are no longer equal. The degree of saturation can be represented as a factor by dividing the energy difference (dE) by a reference energy value. The reference energy value is determined by setting a reference point on the B-H curve of the steel material, beyond which the material can be considered fully saturated. Figure 55 shows the B-H curve of the silicon steel M600-65A, the B-H curve can be viewed as two linear regions with a connecting non-linear region referred to as the 'knee'. To determine the saturation reference flux density (B_{REF}) the last ten B-H datapoints of the material were plotted and a linear trendline was applied. From the equation of the trendline the value of the Y intercept was set as B_{REF} , the number of data points used by the trendline was varied to check for convergence.

The reference magnetic energy (E_{M-REF}) and co-energy (E_{C-REF}) of B_{REF} can then be found from the B-H curve of the material, Figure 55. The energy reference (E_{REF}) was set to the largest energy value, this was used as the base for the energy per unit scale. For example a design uses the material M600-65A, the desired peak stator tooth flux density (B_{ts}) is set as 1.5 T and the desired peak rotor tooth flux density (B_{tr}) is 1.55 T. The corresponding energy values are shown in Table 13. The subscripts refer to the stator and rotor values. The Equations (14) and (15) calculate the independent saturation factor of the stator and rotor, and (16) determines the value of K_{ts} . This provides an initial estimation of K_{ts} for use with the analytical method, the value of K_{ts} may change during the design iterations.

Table 13: Flux density and energy values for saturation factor calculation

$B_{REF} = 1.8 \text{ T}$	$E_{C-REF} = 1533 \text{ J}; E_{M-REF} = 13353 \text{ J};$ $E_{REF} = E_{M-REF} = 13353 \text{ J}$
$B_{ts} = 1.5 \text{ T}$	$E_{CS} = 360.79 \text{ J}; E_{MS} = 1649.21 \text{ J};$ $dE_S = 1288.42 \text{ J}$
$B_{tr} = 1.55 \text{ T}$	$E_{CR} = 438.29 \text{ J}; E_{MR} = 2289.71 \text{ J};$ $dE_R = 1851.42 \text{ J}$

$$K_{tss} = \frac{dE_S}{E_{REF}} = \frac{1288.42}{13353} = 0.096 \quad (14)$$

$$K_{tsr} = \frac{dE_R}{E_{REF}} = \frac{1851.42}{13353} = 0.139 \quad (15)$$

$$1 + K_{ts} = 1 + K_{tsr} + K_{tss} = 1 + 0.139 + 0.096 = 1.24 \quad (16)$$

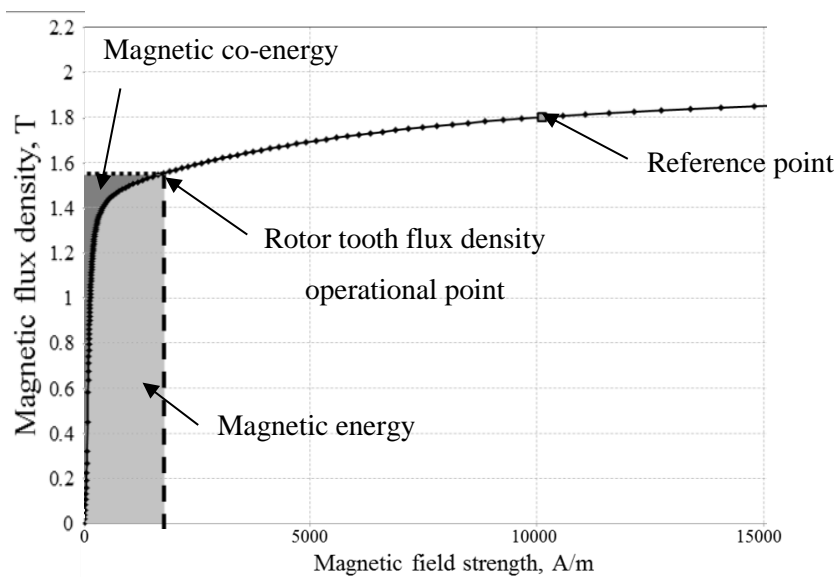


Figure 55: B-H curve of M600-65A with reference point and rotor tooth operational point

4.4.3. Initial sizing of the machine

The inner stator diameter can be calculated using the shear stress calculated from the permanent magnet design, $\sigma = 6.5 \text{ kN/m}^2$, and the initial parameters of the three designs. Table 14 compares the stator inner diameter of the three designs calculated using Equation (17) [37] with the diameters presented in Table 12. The stack aspect ratio (λ) is the ratio of the axial length and the pole pitch. Equation (17) was rearranged so that the shear stress was the subject of the calculation. The shear stress of the machines with the stator inner diameter calculated from Equation (10) could be calculated and compared to the permanent magnet design.

Table 14 demonstrates that the difference between the stator inner diameters from both equations does not exceed 10%. The difference in the stator inner diameter of the 60 and 100 segments is 3% and 1% respectively. However, the difference in shear stress is significant with the 40 segment having a shear stress 34% lower than the permanent magnet design. The shear stress of the 60 segment is 10% higher and the 40 segment is 3% higher than the permanent magnet design. A high shear stress demonstrates a high torque produced for a small rotor volume.

$$D_{is} = \sqrt[3]{\frac{4 \cdot P_p}{\pi^2 \cdot \lambda \cdot \sigma} \left(0.1641 \cdot P_n \cdot \frac{P_p}{F} \right)} \quad (17)$$

Table 14: Comparison of inner stator diameter

Number of segments	40		60		100	
Equation	(17)	(10)	(17)	(10)	(17)	(10)
Stator inner diameter, m	0.3236	0.3567	0.2452	0.2379	0.1443	0.1427
Shear stress, N/m ²	6500	4855	6500	7116	6500	6724

4.4.4. Stator design

The individual segments have previously been compared to a linear induction machine (LIM) and the choices of the windings for a LIM are appropriate for this design. Using the LIM winding configurations the coils are contained within the segment and prevents the coils spanning across segments. With the coils contained the segments can be constructed in modules that are mounted into the frame of the turbine. The most common configurations as outlined by Boldea et al in [37, pp. 593-595] are single layer, double layer, triple layer and fractional windings. None of these configurations are flawless and have benefits that suit particular applications of linear machines.

The double layer winding, a common choice for a conventional SCIG, in a linear machine requires two additional slots for a fully pitched winding. In a conventional rotary machine a double layer winding allows efficient use of the slots and results in shorter end windings. Short pitching a double layer winding is simple and reduces the harmonics in the windings. However the first and last slots are only half filled and the slots are not fully utilised, and short pitching the coils requires additional slots. This winding configuration has short end windings and a simple construction, this is recommended for large LIMs with an odd number of poles [37, pp. 594]. The slot layout of the double layer winding is shown in Figure 56.

The triple layer winding also has short end windings, this winding can be short pitched to remove harmonics and provides an even number of poles. However it requires deep slots to accommodate the additional layers, this is difficult for machines with a limited stator volume. The slot layout of the triple layer winding is shown in Figure 57.

Fractional slot windings have very short end windings and these are recommended for machines with a limited volume [37, pp. 594]. The coils are simple to construct with being concentrated as opposed to distributed. If the machine has a small number of poles and current symmetry is important to reduce vibration and noise. It is suggested that the use of 2 phases with this winding would be better than 3 phases [37, pp. 595]. The slot layout of the fractional winding is shown in Figure 58.

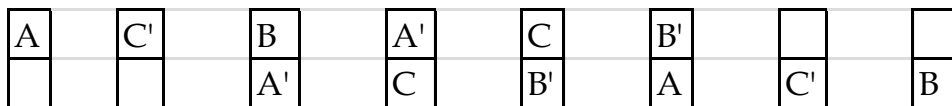


Figure 56: Double layer winding slot layout

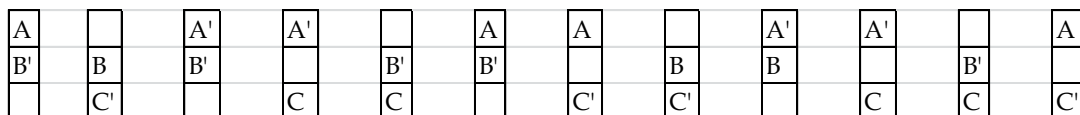


Figure 57: Triple layer slot layout

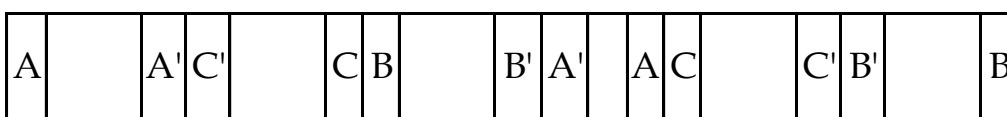


Figure 58: Fractional winding slot layout

The single layer winding has large end windings but this type of winding makes good use of the slots as each slot is filled. This configuration provides an even number of poles, however it cannot be short pitched to reduce harmonics. The coils have a simple construction which helps simplify the design of the machine.

Of these windings the two that are suitable for the OpenHydro design are the single layer winding and the fractional slot winding. For simplicity the initial design will use a single layer winding, the fractional slot winding is similar to the air cored winding in the PMSG.

A 3 phase machine with single layer winding requires different tiers, also referred to as planes, for the overhang of the coils. This overhang can be arranged in 2 or 3 tiers depending on the arrangement of the coils, typically a concentric arrangement is used with single layer windings. Concentric windings can be broken into 3 types: concentric continuous chain, concentric broken chain and split concentric [55, pp. 202]. The concentric continuous chain only requires 2 overhang planes commonly used in machines with only 2 or 3 slots per pole per phase [55, pp. 203].

The concentric broken chain requires an additional overhang plane, however the advantage of this type of concentric winding is that it avoids coils across joints in machines with split stators [55, pp. 203]. The split concentric is mainly used in large machines where there are more than four slots per pole per phase. For the segment design the concentric broken chain will be used for the coils so 3 tiers are required for the end windings of the coils. The disadvantage of this type is that the end winding losses are unsymmetrical. An example of a concentric broken chain winding is shown, Figure 59.

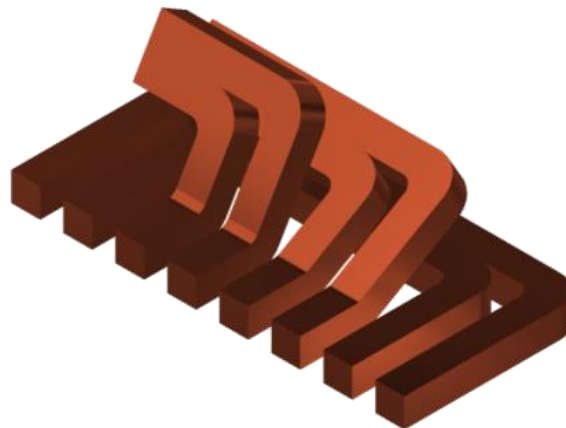


Figure 59: Concentric broken chain end windings

4.4.5. Rotor design

There are several options for the rotor bar profile such as the single bar, deep bar and double bar. The OpenHydro machine will be driven by an inverter as variable speed is required, a suitable rotor slot profile for an inverter driven induction machine is shown in Figure 60 as presented by Zhao et al [57]. The authors recommend that the ratio of $h_{b2}/d_2 < 1.5$ and the ratio of $d_1/d_2 > 0.9$ for lower rotor leakage

inductance and improved power factor [57]. More importantly, this causes a more consistent power factor across the frequency range.

By setting the ratio $d_1/d_2 = 1$ the bar then resembles a rectangular bar which simplifies the construction of the design without affecting the design's performance. The initial design used trapezoidal bars with round backs, Figure 61 demonstrates the evolution of the bar design. Figure 62 shows the final design from MotorSolve.

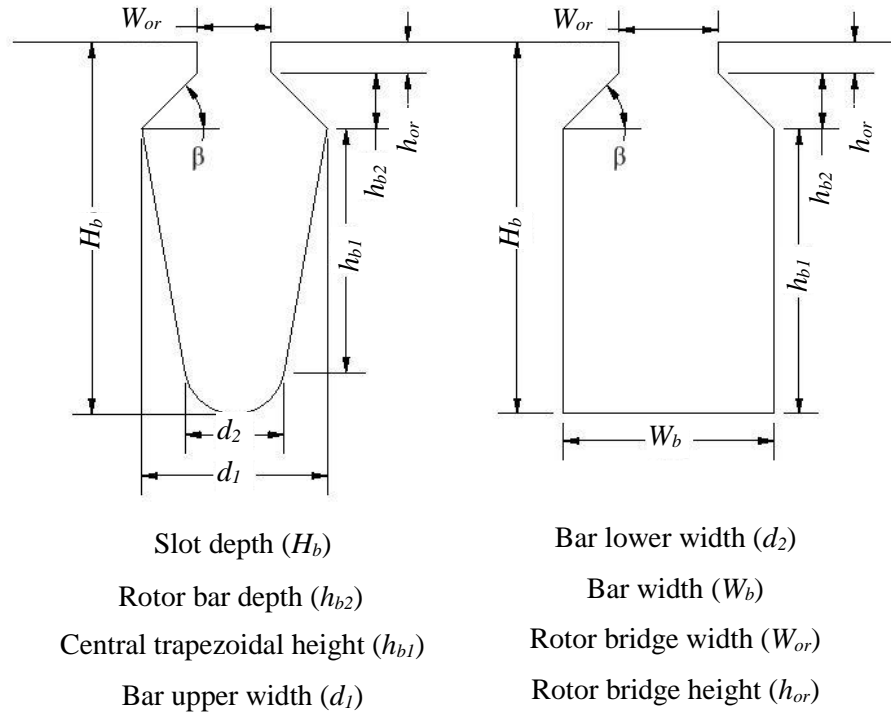


Figure 60: Rotor slot shape for inverter driven induction machine

The rectangular bars were designed using the equations for trapezoidal slots, the variables were altered until the ratio of the upper and lower bar widths was approximately unity. For the bar design to be more representative of the bars used in the models Equations (18)- (20) were derived. The bar angle (β) is a variable of the bar design as is the rotor tooth width (W_{tr}).

$$W_b = \frac{\pi \cdot (D_{or} - 2 \cdot h_{or} + W_{or} \cdot \tan(\beta)) - N_r \cdot W_{tr}}{N_r + \pi \cdot \tan(\beta)} \quad (18)$$

$$h_2 = \frac{1}{2} \cdot (W_b - W_{or}) \cdot \tan(\beta) \quad (19)$$

$$H_b = h_1 + h_2 + h_{or} \quad (20)$$

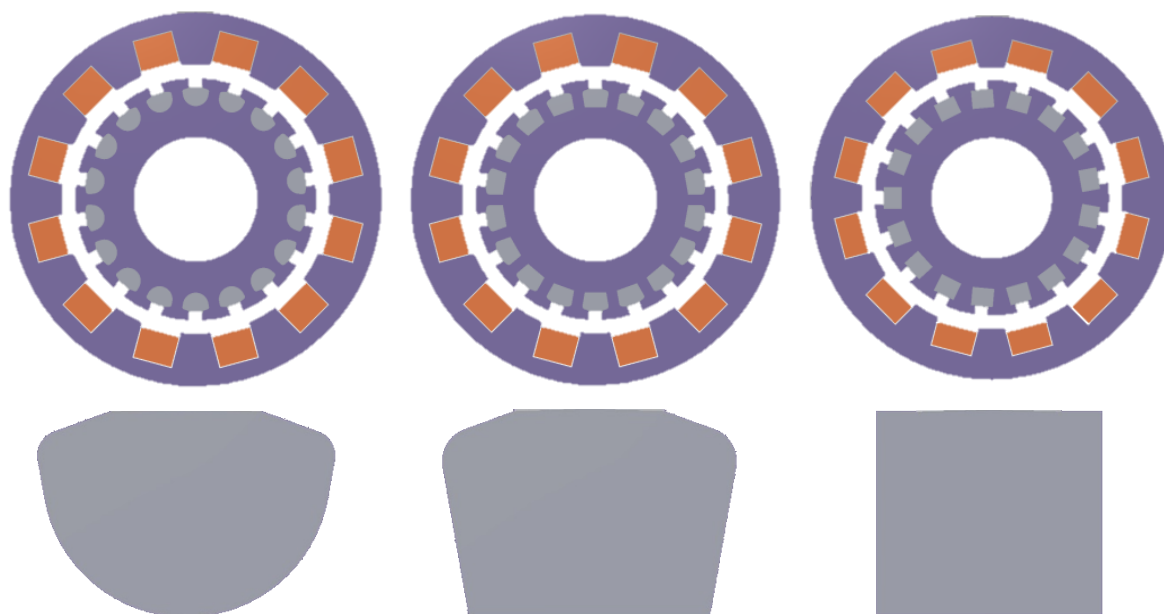


Figure 61: Progression from trapezoidal bars with rounded back to rectangular bars

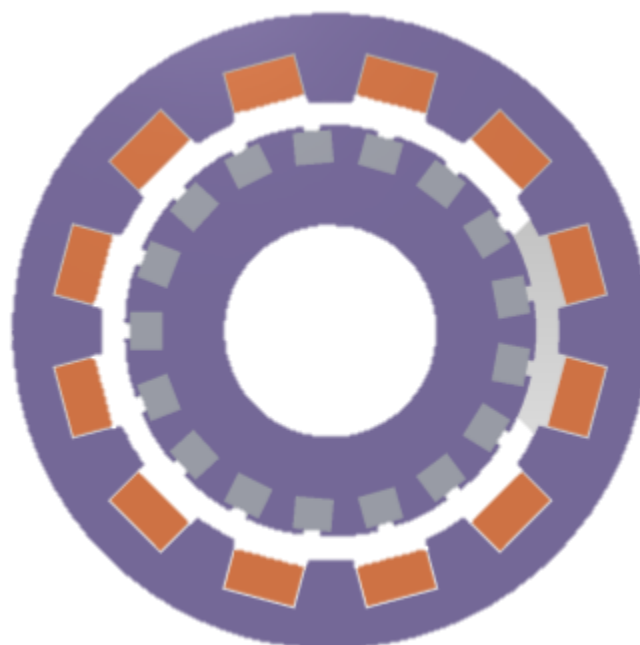


Figure 62: Optimised design

4.4.6. Validity of the slot width guideline in a large air gap machine

A design guideline for induction machines is to ensure the slot opening is at least three times the air gap length. With this design the air gap length is fixed at 12 mm and that the slot opening should be greater than 36 mm. The validity of the slot width design guideline for a large air gap design was investigated. The analytical equations, presented below, were used to investigate the relationship of the slot width and the design performance. Models with various stator slot widths were created, with the slot and copper area held constant. The rotor design was also consistent for each study. It was identified that reducing the slot width (b_{os}) decreased the torque (T) and increased the efficiency (η). The power factor ($\cos\theta$) was constant and the rated current (I_{rn}) reduced. Equations (21)-(31) are presented here as found in [37], and are used to investigate the impact of a slot width less than the designated guideline width.

The torque equation from the ADM, Equation (21), was evaluated and it was observed that the stator phase leakage reactance (X_l) varied significantly by varying the stator slot width. As the slot width is reduced it was expected the slot leakage would increase. Equation (22) shows that the slot leakage is dependent on the permeance, reducing the slot opening increases the permeance. Equation (23) shows the relationship between the slot opening and the permeance. From Equations (21)-(23), it can be observed that as the stator slot opening is decreased the torque also decreases. Similarly the reduction of the slot opening causes the stator slot permeance (λ_{ss}) to increase, as a smaller opening improves the leakage flux path. As the stator leakage reactance is dependent on the permeances the stator leakage reactance increases proportionally. The torque is reduced due to this increased leakage reactance.

In summary, the observed relationship from Equations (21)-(23) is $b_{os} \downarrow = \lambda_{ss} \uparrow = X_l \uparrow = T \downarrow$.

$$T = \frac{V_{phase}^2 \cdot \left(\frac{R_2'}{S}\right)}{\left(R_1 + C_1 \cdot \left(\frac{R_2'}{S}\right)\right)^2 + (X_1 + C_1 \cdot X_2')^2} \cdot \frac{m \cdot P_p}{2 \cdot \pi \cdot F} \quad (21)$$

Torque (T), Nm

Phase voltage (V_{phase}), V

Slip (s)

Stator phase resistance (R_l), Ω

Rotor cage resistance referred to stator (R_2'), Ω

Torque coefficient (C_l)

Stator phase leakage reactance (X_l), Ω

Rotor cage leakage reactance (X_2'), Ω

Number of phases (m)

Number of pole pairs (P_p)

Electrical frequency (F), Hz

$$X_1 = \frac{16 \cdot \pi^2 \cdot 10^{-7} \cdot F \cdot W_1^2 \cdot (\lambda_{ss} + \lambda_{zs} + \lambda_{tts} + \lambda_{os})}{P_p \cdot q} \quad (22)$$

Stator slot leakage permeance (λ_{ss}), WbA^{-1}

Stator zigzag leakage permeance (λ_{zs}), WbA^{-1}

Stator end winding leakage permeance (λ_{os}), WbA^{-1}

Stator tooth leakage permeance (λ_{tts}), WbA^{-1}

Stator slots per pole per phase (q)

$$\lambda_{ss} = \frac{h_{cs} + 3 \cdot h_{os}}{3 \cdot b_{os}} \quad (23)$$

Copper height (h_{cs}), m

Wedge height (h_{os}), m

The magnetisation reactance was observed to rise almost equally with the stator phase leakage reactance. The magnetisation current (I_μ) was observed to decrease and Equation (24) shows that this increases the first term. The value of the stator phase leakage reactance has negligible effect on the magnetisation reactance. Equations (24)-(30) show that a reduction in the stator opening results in the magnetisation reactance increasing. The observed relationship shows that reducing the stator slot opening reduces the Carter coefficient (K_c). The Carter coefficient is a factor that increases the air gap length to account for the slotting of the stator and rotor. Reducing the effective air gap length reduces fundamental MMF (F_{1m}) hence a lower magnetisation current is required to drive the magnet circuit. As a consequence of this the magnetisation reactance (X_m) is increased.

The observed relationship is $b_{os} \downarrow = K_c \downarrow = F_{1m} \downarrow = I_\mu \downarrow = X_m \uparrow$.

$$X_m = \left(\sqrt{\left(\frac{V_{phase}}{I_\mu} \right)^2 - R_1^2} \right) - X_1 \quad (24)$$

Magnetisation reactance (X_m), Ω

Magnetisation current (I_μ), A_{rms}

$$I_\mu = \frac{\pi \cdot P_p \cdot F_{1m} \cdot a_i}{2 \cdot m \cdot \sqrt{2} \cdot W_1 \cdot K_{w1}} \quad (25)$$

Fundamental MMF (F_{1m}), At

Fundamental winding factor (K_{w1})

Number of turns per phase (W_1)

Number of parallel current paths (a_i)

$$F_{1m} = 2 \cdot \left(\frac{B_g}{\mu_0} \cdot l_g \cdot k_c + F_{mts} + F_{mtr} \right) + F_{mcs} + F_{mcr} \quad (26)$$

Peak air gap flux density (B_g), T

Stator tooth MMF (F_{mts})

Permittivity of a vacuum (μ_0), WbA⁻¹

Rotor tooth MMF (F_{mtr})

Air gap length (l_g), m

Stator core back MMF (F_{mcs})

Carter coefficient (k_c)

Rotor core back MMF (F_{mcr})

$$K_c = K_r \cdot K_s \quad (27)$$

$$K_s = \frac{\tau_s}{\tau_s - \frac{b_{os}^2}{5 \cdot l_g + b_{os}}} \quad (28)$$

Rotor Carter coefficient (K_r)

Stator slot opening width (b_{os}), m

Stator Carter coefficient (K_s)

Stator slot pitch (τ_s), m

As the stator leakage reactance increases proportionally to the magnetisation reactance the power factor is effectively constant. The power factor relationship in Equation (29) is based on the ratio of the leakage reactance and the magnetisation reactance.

$$\cos\theta \approx \frac{1 + \frac{X_1 + X_2'}{X_m}}{1 - \frac{X_1 + X_2'}{X_m}} \quad (29)$$

$$\cos\theta \propto \frac{I_\mu}{I_{1n}} \quad (30)$$

From Equation (30), for a constant power factor the rated current has to decrease at the same rate as the magnetisation current. Reducing the rated current reduces the loss power which in turn increases the efficiency, Equation (31).

$$\eta = \frac{P_{mech}}{P_{mech} + 3 \cdot I_{1n}^2 \cdot R_1 + 3 \cdot R_2' \cdot (I_{1n} \cdot k_i)^2} \quad (31)$$

Using the ADM equations, Equations (21)-(31), the effect of the slot aspect ratio was investigated whilst all other dimensions were held constant. The slot depth increased as the slot width decreased, however the core back depth was also held constant and therefore the stator outer diameter was restricted to prevent it exceeding the maximum outer diameter. Figure 63 shows that reducing the slot opening below 36 mm can marginally improve efficiency and power factor, however it shows that the design guideline can be relaxed with a large air gap machine. Figure 63 shows the efficiency from the JMag FEA model compared to the efficiency from the ADM, the ADM predicts a greater variation of efficiency with the slot opening. The graph includes the efficiency calculated in a single instance and after a convergence loop referred to as ADM(6) it was found that the values of current and efficiency effectively converged after 6 loops.

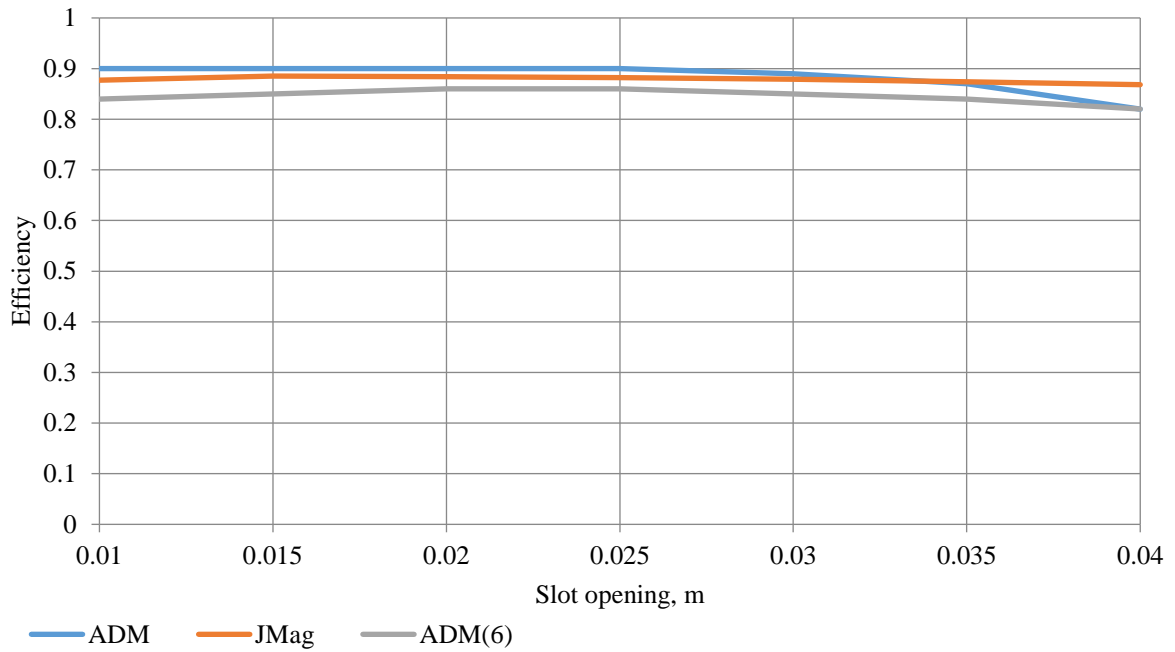


Figure 63: Efficiency variation with slot opening, using FEA and ADM

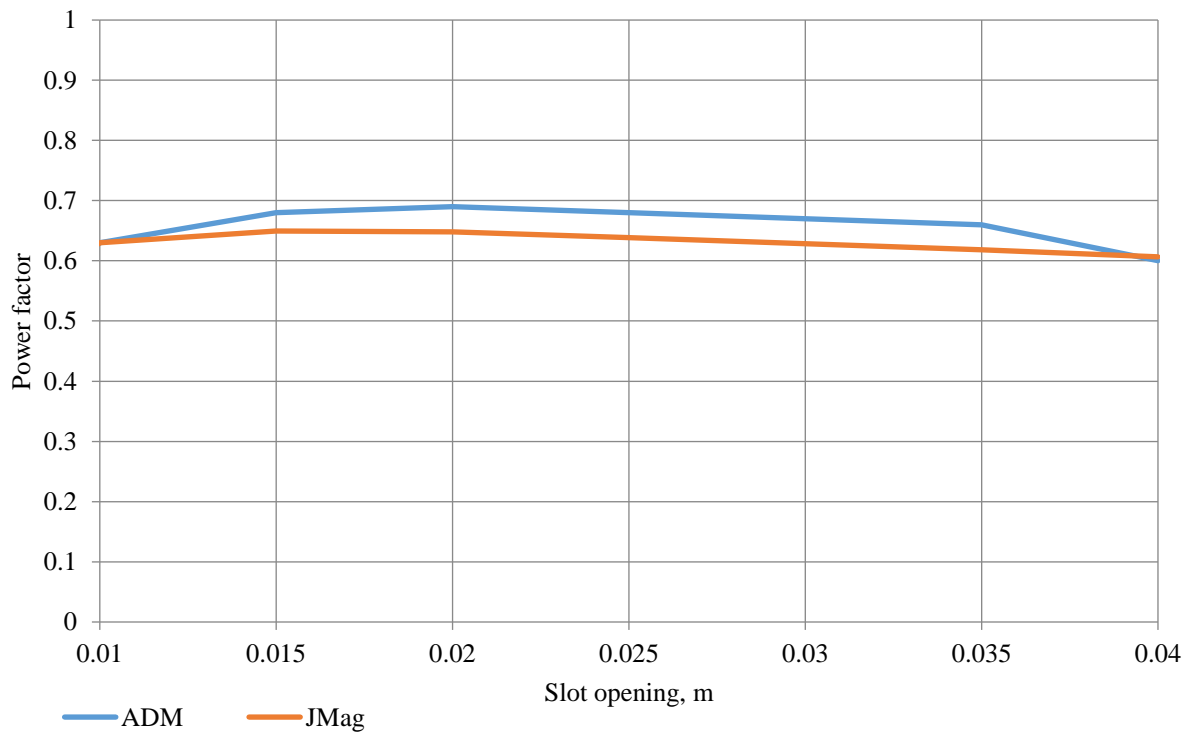


Figure 64: Power factor variation with slot opening, using FEA and ADM

4.4.7. Execution of the proposed analytical design method

The complete design process is shown in Figure 65, the initial sizing of the machine is decided based on the design parameters. The stator design determines the stator characteristics such as the number of stator slots, the type of windings and the slot shape. The rotor design follows based on the choices made for the stator. The equivalent circuit parameters such as the leakage inductances and resistances are calculated based on the machine geometry. The performance of the induction machine is calculated as a motor and the results are compared to the desired values of torque, efficiency, current and power factor. If the design is acceptable then a FEA model is simulated to validate the analytical results.

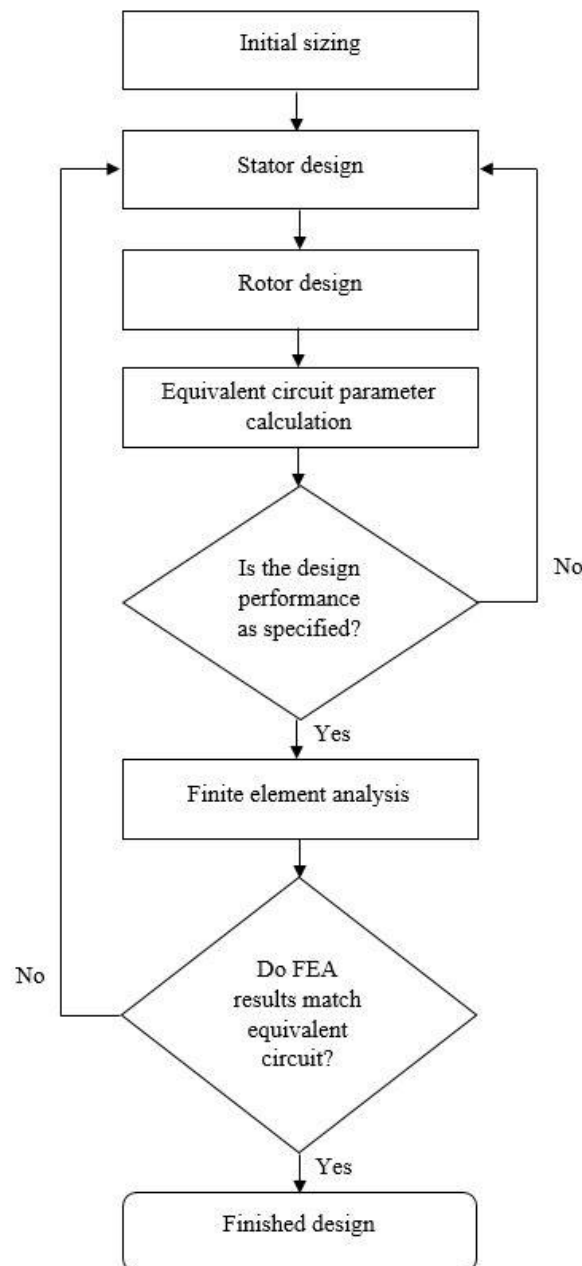


Figure 65: Design flowchart

Initial sizing of the machine

The initial size of machine determines the stator inner diameter, the axial length (L_a), the pole pitch (T) and the slot pitch (T_s). The stator inner diameter is set by the number of segments and calculated as in 4.3, the axial length is calculated based on the number of pole pairs, the stator inner diameter and the stacking factor (SF). Equation (32) is the method of calculating the axial length from [37], typical stacking factors for a single pole pair design are between 0.6-1[37],

$$L_a = \frac{SF \cdot \pi \cdot D_{is}}{2 \cdot P_p} \quad (32)$$

The pole pitch is determined by the number of poles and calculated from Equation (33) and the slot pitch, Equation (34), is set by the number of phases and the number of slots per pole per phase. Both equations are conventional and found in the induction machine design handbook [37].

$$T = \frac{\pi \cdot D_{is}}{2 \cdot P_p} \quad (33)$$

$$T_s = \frac{T}{m \cdot q} \quad (34)$$

Stator design

To begin the stator design the number of stator slots (N_s) has to be determined, the number of stator slots are defined by the chosen number of pole pairs, phases and slots per pole per phase, Equation (11) [37].

The short pitch factor (k_p) and distribution factor (k_d) are calculated based on the slot mechanical angle and the winding factor (k_{w1}) was then found by the multiplication of the two factors. An estimate of the saturation factor is set using the method in 4.4.2, this establishes the flux density shape factor (α_i) and the form factor (k_f). An estimate of the air gap flux density (B_g) is required to calculate the pole flux (φ), Equation (35) [37].

$$\varphi = \alpha_i \cdot T \cdot L_a \cdot B_g \quad (35)$$

All the designs are star connected and the coil layout was chosen in 4.4.4, the number of turns per phase (W_1) was determined using Equation (36) [37]. The machine is designed as a motor thus the EMF is lower than the voltage. The EMF is established by multiplying the phase voltage with the EMF constant (k_e). The EMF constant is established by the number of pole pairs using Equation (37) [37].

$$W_1 = \frac{k_e \cdot V_{ph}}{4 \cdot k_f \cdot k_{w1} \cdot f \cdot \varphi} \quad (36)$$

$$k_e = 0.98 - (0.005 \cdot P_p) \quad (37)$$

The number of conductors per slot (n_s) was calculated from the number of parallel paths (a_i), the number of turns per phase, the number of pole pairs and the number of slots per pole per phase. An integer number of conductors per slot needs to be chosen, the number of turns per phase and the air gap flux density are recalculated.

The rated current (I_{rn}) is required to calculate the wire cross sectional area (A_{cu}), and a value of current density has to be selected. The rated current was calculated from the rated power, the rated voltage and chosen values of efficiency and power factor. Parallel conductors in the same current path such as using Litz wire reduces the amount of current per conductor. However the number of conductors per slot is increased and the wire cross sectional area is decreased by the number of parallel conductors (a_p).

Various dimensions of commercially available round, square and rectangular conductors are provided in lookup tables. The choice of conductor is important as a high fill factor can be achieved with square and rectangular wires. The arrangement of the conductors within the slot also needs consideration, as an example Figure 66 shows 10 rectangular conductors arranged in a slot. The vertical arrangement of five rows and two columns has the best thermal pathways, as each conductor has at least one side in contact with the slot. However the end windings are more difficult as the conductors have to be bent along the width of the conductor. The horizontal arrangement has two rows and five columns, the three centre conductors in the top row have no contact with the slot and have the worst thermal pathway. The slot width and height are determined by the choice of the conductor arrangement and the tooth width was calculated by subtracting the slot width from the slot pitch.

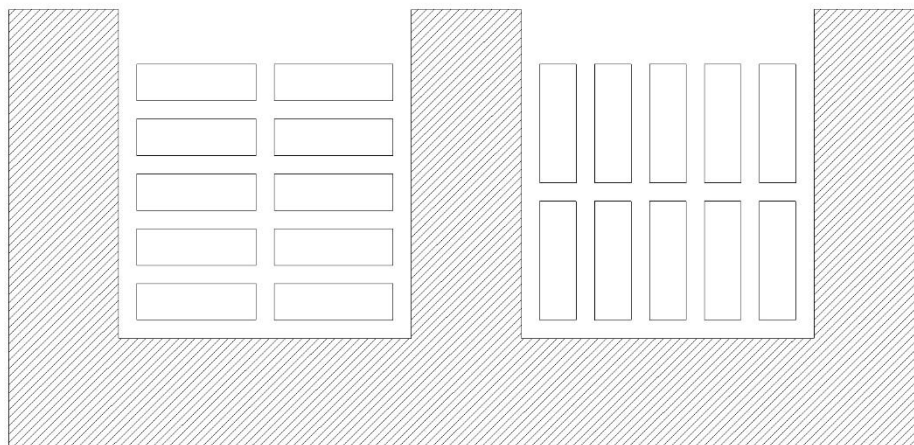


Figure 66: Vertical and horizontal conductors in a slot

Rotor design

The rotor outer diameter is defined by the stator inner diameter and the air gap length, the number of rotor bars (N_r) is selected to reduce noise and vibration [37]. The bar current is calculated using Equation (38) [37], and the ratio of the stator and rotor MMF (k_i) is decided using Equation (39) [37].

$$I_b = \frac{k_i \cdot 2 \cdot m \cdot W_1 \cdot k_{w1} \cdot I_{1n}}{N_r} \quad (38)$$

$$k_i = (0.8 \cdot PF) + 0.2 \quad (39)$$

With the bar current known and the rotor bar current density selected, the rotor slot area can be determined. Similarly the end ring current (I_{er}) can be established from Equation (40) [37], and the end ring cross sectional area is defined by the choice of the end ring current density.

$$I_{er} = \frac{I_b}{2 \cdot \sin\left(\frac{\pi \cdot P_p}{N_r}\right)} \quad (40)$$

The rotor bar tooth width (W_{tr}) is calculated from the lamination factor, the rotor slot pitch (T_r) and the rotor tooth flux density (B_{tr}). The rotor bar dimensions are determined as presented in 4.4.5 with values of the rotor bar angle and the rotor bridge width and height selected. Figure 67 shows the end rings and bars of a squirrel cage, the end ring dimensions are defined by the bar dimensions. The end ring height (H_{er}) is calculated from Equation (41) [37], and the end ring width (W_{er}) is determined from the end ring cross sectional area and the end ring height. The end ring height is either the same as the rotor bar height or 20% larger determined by the factor c which has a value in the range of 1-1.2.

$$H_{er} = c \cdot (H_{b1} + h_{or} + \frac{1}{2} \cdot (W_b - W_{or}) \cdot \tan(\beta) + \frac{1}{2} \cdot W_b) \quad (41)$$

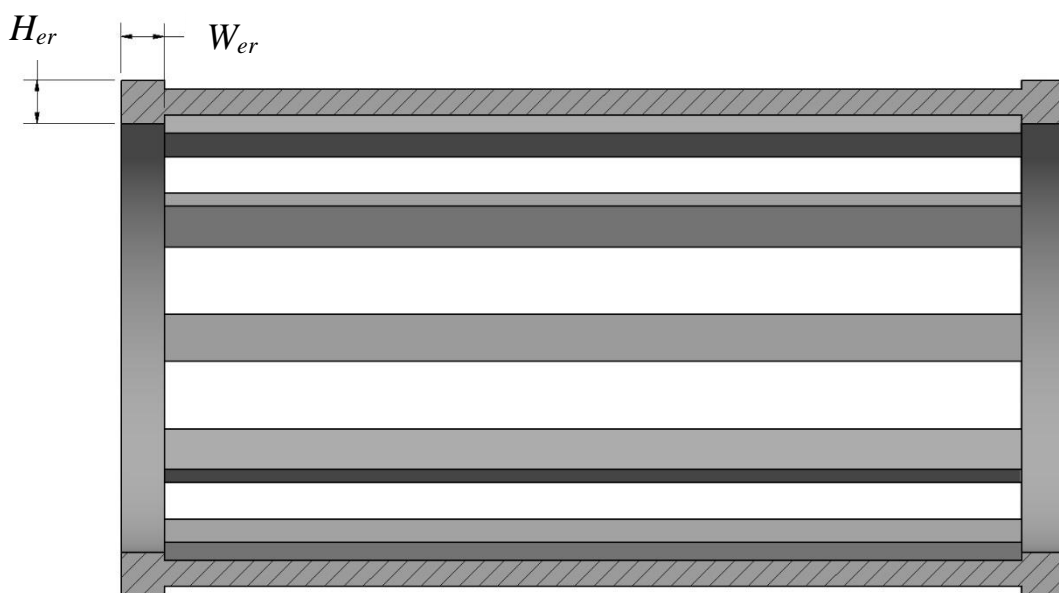


Figure 67: Half section of the squirrel cage

Equivalent circuit parameter calculation

The equivalent circuit parameters are useful to predict the performance of the designs, to calculate the performance the methods presented in [37] and [55] are included. Values are required for both the stator and rotor resistances and inductances as well as for the magnetisation inductance and the core loss resistance. The resistances are calculated based on the geometry of the generator and the resistance equation accounts for the increased winding temperature. The stator and rotor inductances are calculated based on the permeance of the slot as well as the permeance of the loss paths. The methods to calculate the permeances of the paths from both [56] and [37] are incorporated into the ADM. With the design's equivalent circuit parameters calculated the torque, current, efficiency and power factor at various values of slip can be ascertained. If the performance is acceptable the design is validated using MotorSolve.

4.5. The initial designs

The three initial designs are shown in Figure 68, the software MotorSolve was used to validate the performance of the designs. MotorSolve is a FEA software package that can quickly size an electric machine based on a number of parameters. The design can be modified after the initial sizing process or the sizing process can be by-passed. The output of the software provides an equivalent circuit, graphs of torque, power factor, RMS current, RMS line voltage and efficiency versus speed.

The torque of the 60 segment model is shown in Figure 69, the torque is calculated by the ADM based on the geometry of the design. Table 16 lists the equivalent circuit values from the ADM and from MotorSolve. The ADM predicts a lower peak torque than MotorSolve, the magnitude of the peak torque is dependent on the rotor reactance, a lower reactance results in a higher peak torque. However in this case the difference in the peak torques can be attributed to the difference between the stator reactance. The graph also shows the ADM calculations using the MotorSolve equivalent circuit values. The model was then checked using the FEA software JMag, as shown the peak torque is comparable to the peak torque calculated by the ADM. However the values of torque at higher slip are significantly lower, this can be attributed to the ratio of the rotor inductance and resistance.

Table 15: MotorSolve design data

Number of segments	40	60	100
Line voltage, V_{RMS}	415	415	415
Synchronous speed, rpm	996	1500	2496
Frequency, Hz	33.3	25	41.6
Number of pole pairs	2	1	1
Slots/pole/phase	2	2	1
Number of stator slots	24	12	6
Number of rotor slots	28	17	12

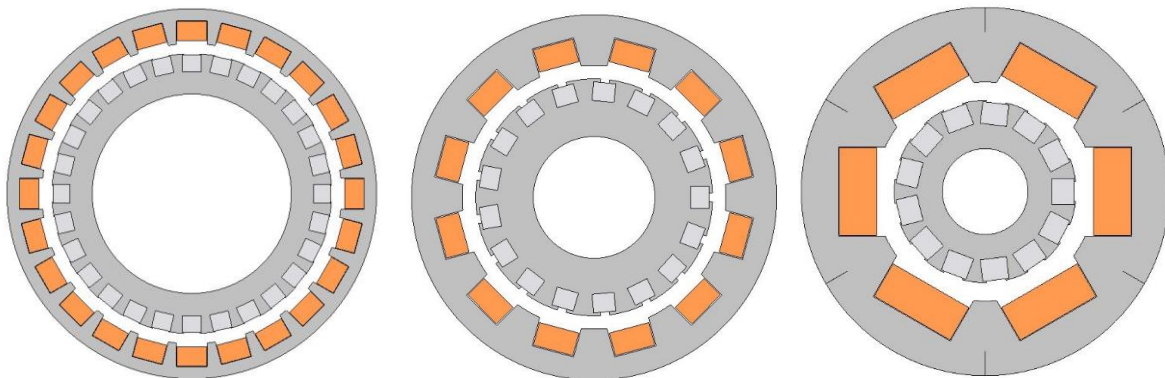
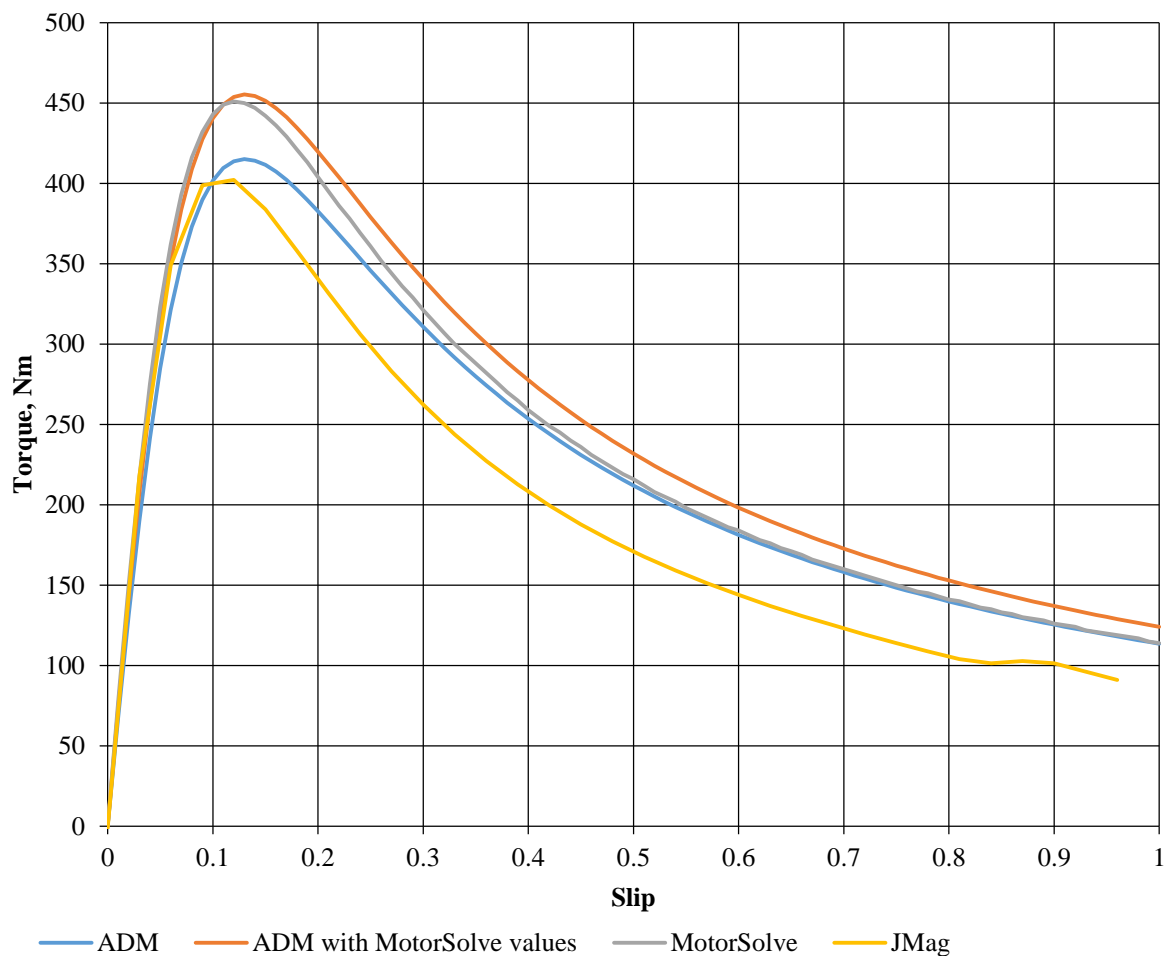


Figure 68: From left to right are the 40, 60 and 100 segment designs

Table 16: Comparison of ADM and MotorSolve

Parameters	ADM	Motorsolve
Stator resistance, Ω	0.0972	0.0828
Referred rotor resistance, Ω	0.1255	0.12
Stator inductance, H	0.00256	0.00216
Referred rotor inductance, H	0.00381	0.00386
Stator reactance, Ω	0.4028	0.3393
Referred rotor reactance, Ω	0.5981	0.6063

**Figure 69: Torque of the 60 segment**

The torque, efficiency and power factor of the three models are shown in Figure 70, Figure 71 and Figure 72. From the profile of the torque curve these designs can be identified as type B induction machines, with operation as a generator the values of the starting torque and current are not relevant with respect to the operational values. The torque of the 40 segment is significantly greater than for the 100 segment however efficiency is comparable. The 60 segment has a higher power factor which is desirable as it reduces the convertor rating.

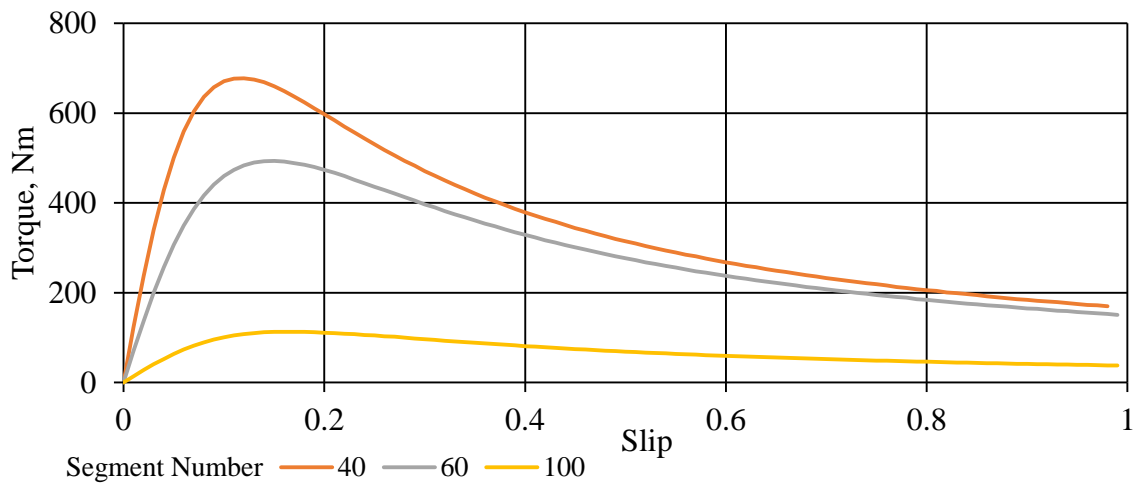


Figure 70: Torque-speed graph of the MotorSolve model

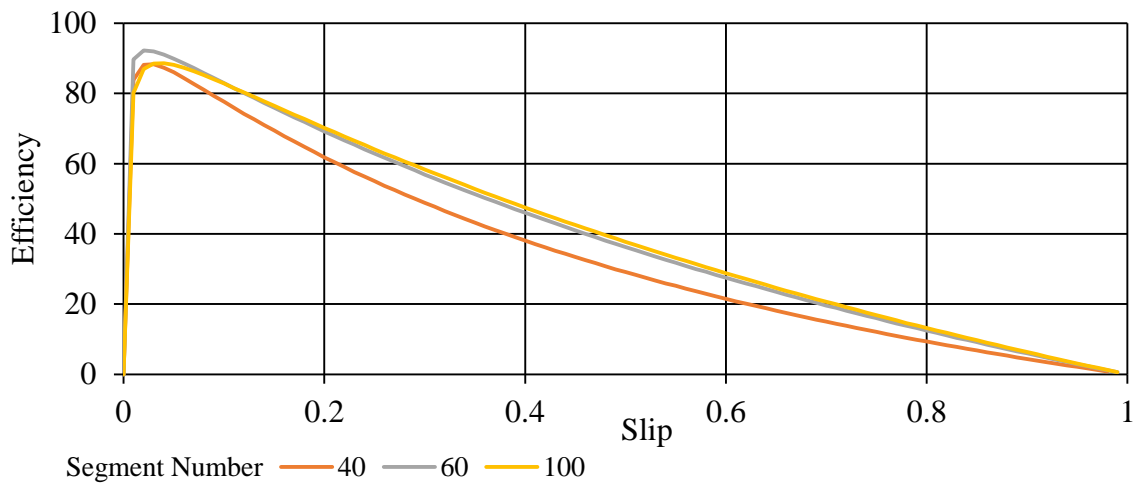


Figure 71: Efficiency of the MotorSolve model

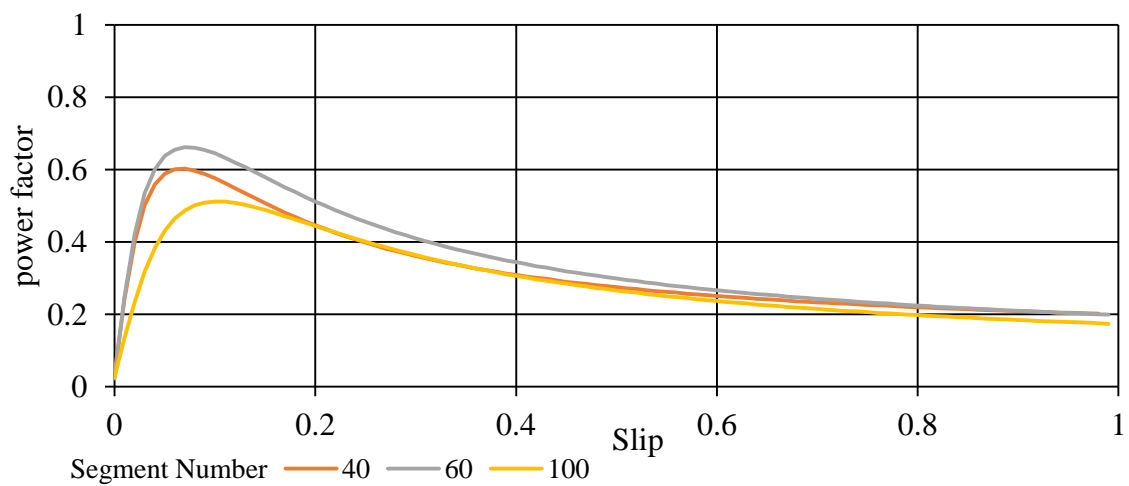


Figure 72: Power factor of the MotorSolve model

Table 17: Efficiency of the three designs for small variations of slip from JMag

Slip	IM-40-0	IM-60-0	IM-100-0
0%	32%	28%	19%
1%	72%	80%	66%
2%	80%	86%	78%
3%	81%	87%	82%
4%	81%	87%	83%
5%	80%	85%	84%
6%	78%	84%	83%
7%	76%	83%	83%
8%	74%	81%	82%
9%	72%	79%	81%
10%	70%	78%	80%

Table 18: Total mechanical power of the three designs for small variations of slip from JMag

Slip	IM-40-0	IM-60-0	IM-100-0
0%	9.42E+04	6.84E+04	4.42E+04
1%	5.36E+05	7.38E+05	3.83E+05
2%	9.56E+05	1.41E+06	7.41E+05
3%	1.27E+06	1.99E+06	1.08E+06
4%	1.49E+06	2.46E+06	1.38E+06
5%	1.62E+06	2.83E+06	1.66E+06
6%	1.68E+06	3.09E+06	1.91E+06
7%	1.69E+06	3.27E+06	2.12E+06
8%	1.66E+06	3.38E+06	2.31E+06
9%	1.62E+06	3.43E+06	2.46E+06
10%	1.56E+06	3.43E+06	2.59E+06

Table 19: Power factor of the three designs for small variations of slip from JMag

Slip	IM-40-0	IM-60-0	IM-100-0
0%	0.09	0.06	0.07
1%	0.21	0.22	0.16
2%	0.32	0.36	0.26
3%	0.39	0.46	0.34
4%	0.42	0.52	0.41
5%	0.43	0.55	0.46
6%	0.43	0.56	0.50
7%	0.42	0.56	0.52
8%	0.41	0.55	0.54
9%	0.40	0.54	0.55
10%	0.38	0.53	0.56

The graphs show the performance of the designs across a wide range of slip from MotorSolve, while the tables contain the results from the models running with a smaller variation of the slip from JMag. The graphs show that the 100 segment has the highest efficiency across the slip range however the 60 segment is capable of higher power factor. The 60 segment design operates at a lower slip than the 100 segment design, this indicates stable operation with little risk of operating in the unstable region of the torque/slip profile. The 40 segment design fails to achieve the desired power rating and has the worst power factor and efficiency.

From the tables in terms of peak efficiency the 60 segment design is the best, achieving an efficiency of 87% with the 40 segment design being the worst with a peak efficiency of 81%. In terms of mechanical power the 60 segment design achieved the rated value of 2.2 MW with an efficiency of 87%. In comparison the 100 segment design only achieves the rated mechanical power at a slip of 7% and a corresponding efficiency of 81%.

These three design have been taken forward for detailed design and are referred to as IM-40-0, IM-60-0 and IM-100-0 respectively.

4.6. 40 segment optimisation

Due to the initial 40 segment design failing to meet the desired rated mechanical power, the machine was redesigned. The 40 segment is the largest of the designs and as such it has the most freedom with regards to design choices such as the pole number, the key challenge is to ensure the design fully utilises the available space. Using guidelines developed earlier, section 4.4.6, the number of poles was reduced and the number of slots per pole per phase was increased to maintain the number of stator slots. The alternative design is referred to as IM-40-1.

Table 20: 40 Segment designs

Design	IM-40-0	IM-40-1
Number of stator slots	24	24
Number of slots per pole per phase	2	4
Number of pole pairs	2	1

Table 21: Efficiency of the initial design and the redesigns

Slip	Original (IM-40-0)	Redesign 1 (IM-40-1)
0.1%	32%	25%
1%	72%	51%
2%	80%	70%
3%	81%	76%
4%	81%	78%
5%	80%	79%
6%	78%	78%
7%	76%	77%
8%	74%	76%
9%	72%	75%
10%	70%	73%

Table 22: Total mechanical power of the initial design and the redesigns

Slip	Original (IM-40-0)	Redesign 1 (IM-40-1)
0.1%	9.42E+04	1.24E+05
1%	5.36E+05	3.88E+05
2%	9.56E+05	9.14E+05
3%	1.27E+06	1.37E+06
4%	1.49E+06	1.76E+06
5%	1.62E+06	2.07E+06
6%	1.68E+06	2.30E+06
7%	1.69E+06	2.46E+06
8%	1.66E+06	2.57E+06
9%	1.62E+06	2.63E+06
10%	1.56E+06	2.65E+06

Table 23: Power factor of the initial design and the redesigns

Slip	Original (IM-40-0)	Redesign 1 (IM-40-1)
0.1%	0.09	0.12
1%	0.21	0.19
2%	0.32	0.31
3%	0.39	0.40
4%	0.42	0.46
5%	0.43	0.49
6%	0.43	0.52
7%	0.42	0.53
8%	0.41	0.53
9%	0.40	0.53
10%	0.38	0.52

4.7. 60 segment optimisation

The design of the IM-60-0 showed an acceptable performance, however to improve the power factor various parameters such as the line voltage, stator and rotor slot openings and turns per phase were altered. The number of rotor bars were also varied to improve the harmonics of the segment model.

The key factor that affects the power factor is the slot leakage flux, a recommended design rule is to design the slot opening to be greater than three times the air gap length. With a 12 mm air gap obeying this rule creates a slot opening of 36 mm or greater. This results in a large Carter coefficient, causing a large air gap MMF and consequently a large magnetisation current. The magnetisation current is a component of the rated current. Equation (31) from [55, pp.275] shows that the efficiency has an inversely proportional relationship to the current squared. As part of the design process the magnetisation current of IM-60-0 was predicted to be 67% of the rated current, for the first redesign the focus was to reduce the magnetisation current.

Equation (25) was used for the calculation, the magnetisation MMF and the number of turns per phase are responsible for the large value of the magnetisation current. The number of pole pairs and the fundamental winding factor were considered constant, reducing the fundamental MMF and increasing the number of turns per phase helped reduce the magnetisation current. The largest factor of Equation (26) is the air gap MMF. To reduce the air gap MMF both the Carter coefficient and the air gap flux density were reduced. The air gap flux density and the turns per phase have an inverse relationship, by increasing the turns per phase to reduce the magnetisation current the air gap flux density is reduced. The Carter coefficient depends on the stator and rotor slot openings. Reducing the width of the slot openings reduces the Carter coefficient, however this increases the slot leakage flux decreasing the power factor of the machine.

The power factor of the induction motor is affected by the ratio of the magnetisation current and the rated current [55, pp. 337]. Reducing the magnetisation current for the same rated current causes the power factor to increase.

Table 24: Redesign of the 60 segment model

design	IM-60-0	IM-60-1	IM-60-2	IM-60-3	IM-60-4
Number of slots per pole per phase	2	2	2	2	2
Number of rotor bars	17	17	17	18	16
Line voltage	415	415	690	690	690

4.7.1. Comparison of the designs

The first redesign (IM-60-1) was created following the method to reduce the magnetisation current. Table 25 shows the efficiency, below 3% slip, of the IM-60-1 was an improvement compared to IM-60-0. At the rated slip, 3%, the efficiency was improved by 14%. As predicted the power factor of IM-60-1 was increased however this occurs at a higher slip than the rated slip.

For the second redesign (IM-60-2) emphasis was placed on the stator ohmic losses as this was calculated to be two thirds of the total losses. The line voltage (V_{line}) was increased to 690 V to reduce the rated current and therefore reduce the stator ohmic losses. Table 25 shows that the efficiency of IM-60-2 increased by 19% compared to IM-60-0 but only 5% compared to IM-60-1. The efficiency has increased but the peak power factor has been reduced, the power factor of IM-60-2 is equal to the power factor of IM-60-0. A feature that is consistent throughout the three designs is the number of rotor bars (N_r), $N_r = 17$. The number of bars of the segmental designs are unsymmetrical and the rotor will experience unbalanced radial forces. In the fully assembled machine the bars are balanced with 1020 bars in total.

Table 25: Efficiency of the original design and redesigns

Slip	IM-60-0	IM-60-1	IM-60-2	IM-60-3	IM-60-4
0.1%	28%	39%	38%	33%	50%
1%	80%	86%	84%	83%	89%
2%	86%	89%	88%	88%	91%
3%	87%	89%	87%	88%	90%
4%	87%	87%	85%	87%	88%
5%	85%	86%	83%	86%	87%
6%	84%	84%	81%	84%	85%
7%	83%	82%	79%	83%	83%
8%	81%	81%	77%	81%	81%
9%	79%	79%	75%	79%	79%
10%	78%	77%	73%	78%	77%

Table 26: Total mechanical power of the original design and redesigns

Slip	IM-60-0	IM-60-1	IM-60-2	IM-60-3	IM-60-4
0.1%	6.84E+04	8.31E+04	9.09E+04	7.53E+04	6.40E+04
1%	7.38E+05	8.57E+05	9.12E+05	8.03E+05	6.07E+05
2%	1.41E+06	1.62E+06	1.68E+06	1.54E+06	1.13E+06
3%	1.99E+06	2.24E+06	2.26E+06	2.17E+06	1.54E+06
4%	2.46E+06	2.72E+06	2.65E+06	2.69E+06	1.83E+06
5%	2.83E+06	3.07E+06	2.89E+06	3.10E+06	2.02E+06
6%	3.09E+06	3.29E+06	3.00E+06	3.42E+06	2.13E+06
7%	3.27E+06	3.43E+06	3.02E+06	3.64E+06	2.17E+06
8%	3.38E+06	3.49E+06	2.98E+06	3.79E+06	2.16E+06
9%	3.43E+06	3.49E+06	2.90E+06	3.88E+06	2.12E+06
10%	3.43E+06	3.46E+06	2.80E+06	3.91E+06	2.06E+06

Table 27: Power factor of the original design and both redesigns

Slip	IM-60-0	IM-60-1	IM-60-2	IM-60-3	IM-60-4
0.1%	0.06	0.06	0.07	0.04	0.07
1%	0.22	0.29	0.32	0.16	0.34
2%	0.36	0.46	0.48	0.26	0.52
3%	0.46	0.56	0.56	0.32	0.59
4%	0.52	0.60	0.58	0.36	0.62
5%	0.55	0.61	0.58	0.37	0.61
6%	0.56	0.61	0.56	0.38	0.60
7%	0.56	0.60	0.54	0.38	0.58
8%	0.55	0.58	0.52	0.38	0.55
9%	0.54	0.57	0.50	0.37	0.53
10%	0.53	0.55	0.48	0.36	0.51

4.8. 100 segment optimisation

The key challenge of the 100 segment design is the limited segment volume that restricts the design choices. The redesign of the 100 segment was referred to as IM-100-1 and the initial 100 segment is referred to as IM-100-0. The 100 segment design has the least flexibility in terms of design choices hence the single alternative with an increased number of turns and rotor bars.

Table 28: Redesign of the 100 segment model

Design	IM-100-0	IM-100-1
Number of rotor bars	12	20
Number of turns per phase	70	150

Table 29: Efficiency of the original design and redesigns

Slip	IM-100-0	IM-100-1
0.1%	19%	3%
1%	66%	65%
2%	78%	77%
3%	82%	81%
4%	83%	82%
5%	84%	82%
6%	83%	82%
7%	83%	81%
8%	82%	80%
9%	81%	78%
10%	80%	77%

Table 30: Total mechanical power of the original design and redesigns

Slip	IM-100-0	IM-100-1
0.1%	4.42E+04	5.10E+03
1%	3.83E+05	3.67E+05
2%	7.41E+05	7.50E+05
3%	1.08E+06	1.09E+06
4%	1.38E+06	1.37E+06
5%	1.66E+06	1.60E+06
6%	1.91E+06	1.77E+06
7%	2.12E+06	1.89E+06
8%	2.31E+06	1.96E+06
9%	2.46E+06	2.00E+06
10%	2.59E+06	2.01E+06

Table 31: Power factor of the original design and both redesigns

Slip	IM-100-0	IM-100-1
0.1%	0.07	0.09
1%	0.16	0.25
2%	0.26	0.41
3%	0.34	0.53
4%	0.41	0.62
5%	0.46	0.67
6%	0.50	0.70
7%	0.52	0.72
8%	0.54	0.72
9%	0.55	0.71
10%	0.56	0.70

The power factor of IM-100-1 is the highest of all the models however the efficiency is reduced to 78% for the rated power of 2 MW.

4.9. Selection of segment number

From the optimisation of the three segment designs the 60 segment achieves the best efficiency with IM-60-1 providing an efficiency of 89% at the rated power with a power factor of 0.56. The design IM-60-1 was chosen to be taken forward, the design was unwrapped to form a linear segment for comparison to the permanent magnet linear model.

4.10. JMag linear model of IM-60-1

The linear model based on the dimensions of the rotary model was used for further optimisation of the design. The linear model better resembles the actual segment. Solving a 3D transient study of the segment model provides the cogging torque and losses, the effect of the gaps between adjacent segments can also be investigated. The stator slot dimensions are the same as for the rotary model, however the width of the tooth root is now smaller due to the unwrapping of the previous model. All dimensions related to the stator inner diameter have been fixed so the stator slot width and the stator tooth tip width are fixed. When the stator is unwrapped the difference in the length of the stator at the back of the slot is removed from the stator tooth root width. The slot dimensions are shown in Figure 73.

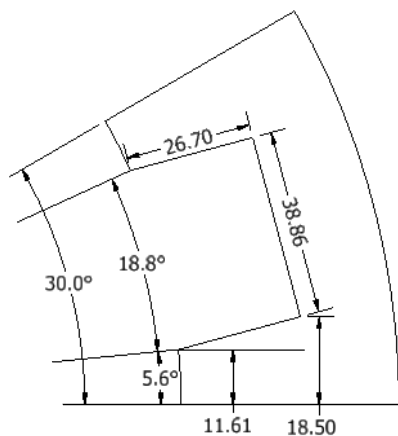


Figure 73: Stator tooth and slot dimensions of the initial design

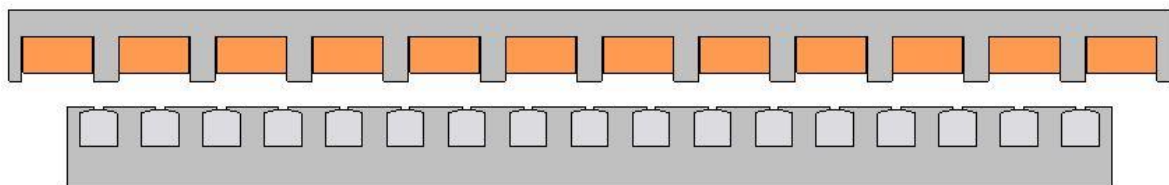


Figure 74: The linear segment

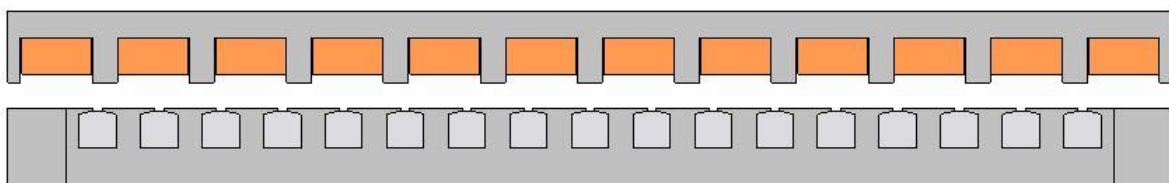


Figure 75: The linear segment with steel spacers

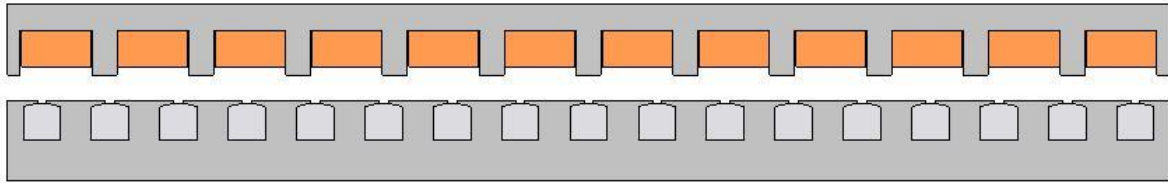


Figure 76: The linear segment with wider teeth

Unwrapping the design results in a shorter translator as shown in Figure 74, the gap between the translator segments introduces a severe spatial harmonic as shown in the force graph Figure 77. The air gap was replaced with steel spacers, this mitigated the ripple as shown in Figure 78. However by distributing the additional steel evenly amongst the translator teeth and maintaining the bar dimensions the ripple was removed, Figure 79.

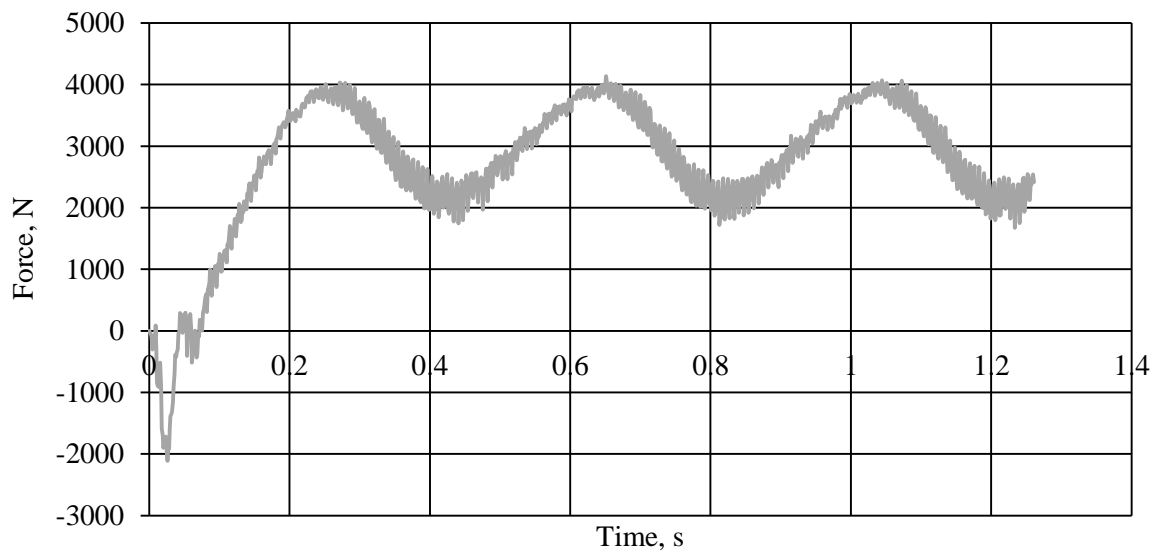


Figure 77: Force of the linear segment

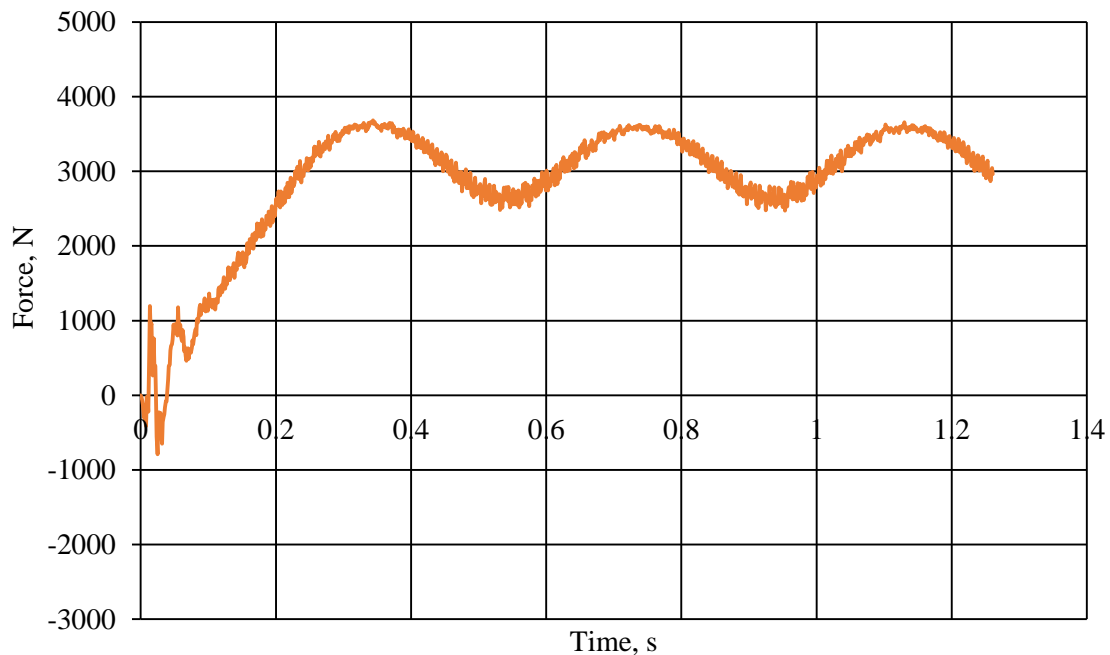


Figure 78: Force of the linear segment with steel spacers

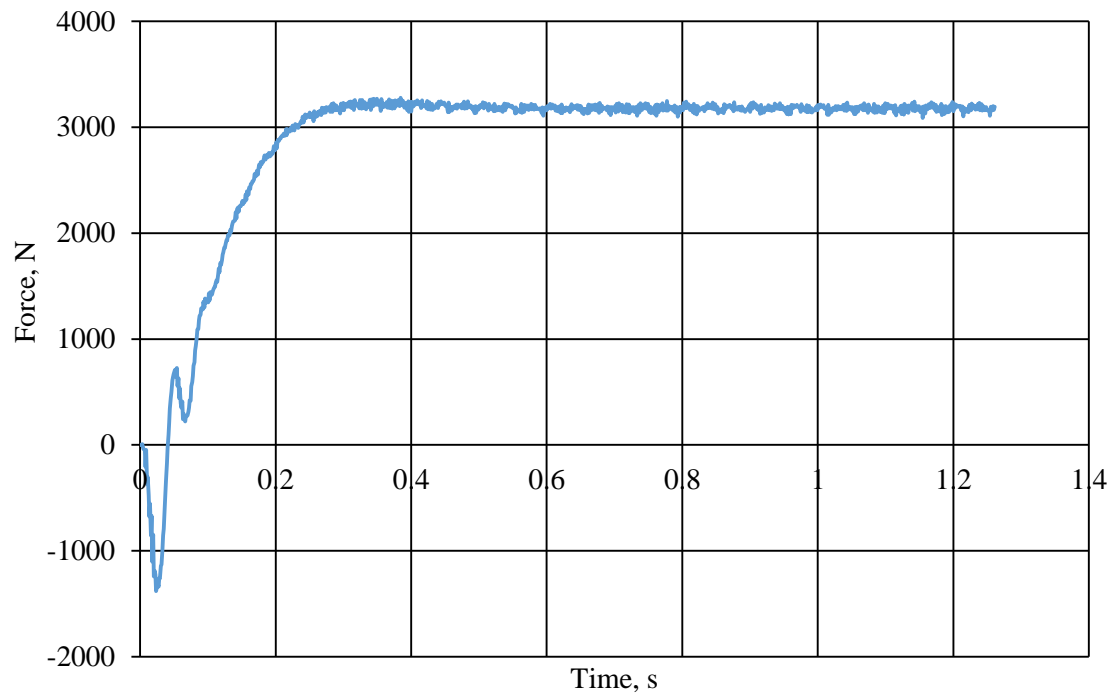


Figure 79: Force of the linear segment with wider teeth

The teeth in the induction machine stator results in a higher attractive force in the machine and with the eccentricity of the rotor this could limit the operational range of the machine. The rotor resists rotating and the machine is started by the flow of the tide. This means the machine can only operate with strong tidal flows and the duration of strong tidal flows is limited.

4.11. Performance of linear induction machine over the tidal speed range

Similar to the permanent magnet machine, the efficiency across the turbine speeds was found assuming two rated speeds of 25 rpm and 15 rpm. The induction machine model was controlled with a simple Volts per Hertz method. The mechanical power is controlled to match the available tidal power from Figure 11 in 2.1.3.

The induction machine was designed with a power rating of 2.2 MW; however the tidal speeds that correspond to this power only occur 1116 hours per year. The available tidal power, calculated using Equation (1), is 600 kW at a tidal speed of 2.75 m/s. The machine was designed to have high performance at a rated speed of 25 rpm. The model was controlled so that the power of model matched the tidal power, and using TSR_{25} the tidal power is 596 kW at a turbine speed of 25 rpm. Table 32 shows that the efficiency is only 58%. TSR_{15} maps the tidal speed of 4 m/s to 25 rpm and the model achieves an efficiency of 82%. Table 32 shows that the design achieves high efficiency at high speeds when the power ratings are close to the rated power, and at lower speeds the design performs poorly. The design has been overrated for the application as it only achieves a high efficiency at the higher tidal speeds unlike the permanent magnet design.

Table 32: Efficiency vs turbine speed

Turbine speed, rpm		mechanical power, kW		Efficiency	
TSR ₂₅	TSR ₁₅	TSR ₂₅	TSR ₁₅	TSR ₂₅	TSR ₁₅
8.18	5.35	31.27	29.01	4%	3%
10.39	6.71	60.44	56.84	8%	3%
12.66	8.07	103.28	98.51	12%	5%
15.00	9.44	162.09	156.89	27%	9%
17.40	10.82	238.98	234.88	36%	16%
19.87	12.21	335.89	335.38	44%	23%
22.40	13.60	454.57	461.35	52%	32%
25.00	15.00	596.60	615.75	58%	42%
27.66	16.41	763.36	801.58	82%	51%
30.39	17.82	956.05	1021.86	89%	59%
33.18	19.24	1175.71	1279.63	92%	65%
36.04	20.67	1423.17	1577.94	93%	71%
38.96	22.11	1699.13	1919.89	93%	80%
41.95	23.55	2004.09	1984.64	92%	81%
45.00	25.00	2004.09	1984.64	92%	82%

4.12. Summary

Three induction machines based on different numbers of segments have been created and the designs were then taken forward for redesign. The 100 segment design has the least design choices (slots per pole combinations), the alternative achieved a high power factor at the expense of efficiency. The original 40 segment design failed to meet the specification, but the redesign achieved the rated power with a low efficiency and power factor. The 60 segment design has shown promise and has been through four redesigns, the first improved the efficiency and at higher slip the power factor. The first redesign IM-60-1 was chosen for the comparison, due to having the best efficiency of all the designs and the best power factor of the 60 segment designs.

The number of segments of the three designs were chosen as 40, 60 and 100 to represent the minimum, median and maximum segment size. These numbers of segments could provide insight to the advantages and disadvantages of the segment size during the design process. It was identified that a high number of segments provides a small segment size, which is advantageous to the construction of the turbine, however the design choices are limited. Conversely a low number of segments provides a great amount of freedom with respect to the design yet the construction is more complex. Therefore the optimum number of segments produces a segment of moderate mass and an arc length that does not limit the design choices.

The segment model IM-60-1 was then used to create a linear model, the translator was shorter due to unwrapping the segment and this introduced a severe spatial harmonic to the force. By widening the rotor teeth the spatial harmonic was removed. The efficiencies of the induction machine have been calculated across the turbine speed range, the design has been over rated and as a consequence the efficiencies at low speed are low.

Chapter 5. Eccentricity

This chapter investigates the effect of eccentricity in the OpenHydro turbine, the aim of the chapter is to assess the effect of eccentricity on both the permanent magnet generator and the induction generator and compare the designs robustness. To this end the linear FEA segment models of both machines are modelled with various air gap lengths. An analytical method for the modelling of the fully assembled induction generator is also presented to assess the effect with multiple segments.

5.1. The problem of eccentricity

Eccentricity is a condition that occurs when the rotor is not concentric to the stator, Figure 80 shows a radially eccentric rotor. Axial eccentricity can also occur. Eccentricity is a concern in electrical machines due to the forces and speeds when in operation. The effects of eccentricity vary from minor failure like increasing the bearing wear, to a catastrophic failure such as the rotor colliding with the stator [58]. There are two distinguishable types of eccentricity, static eccentricity refers to a misalignment of the rotor and stator that is constant when the machine is operating. Dynamic eccentricity is a misalignment that rotates while the machine is under operation. Eccentricity is a mechanical failure and occurs due to manufacturing defects or during machine assembly. A static eccentric condition can develop into a dynamic eccentric condition as the bearings experience excessive wear and the shaft can deflect. Eccentricity is more common in large machines, typically due to large unbalanced magnetic forces, a weak shaft or a heavy rotor mass. Generally the amount of eccentricity is small and results in more maintenance cycles due to the excessive bearing wear. However the OpenHydro turbine features a shaft-less rotor using hydrodynamic bearings.

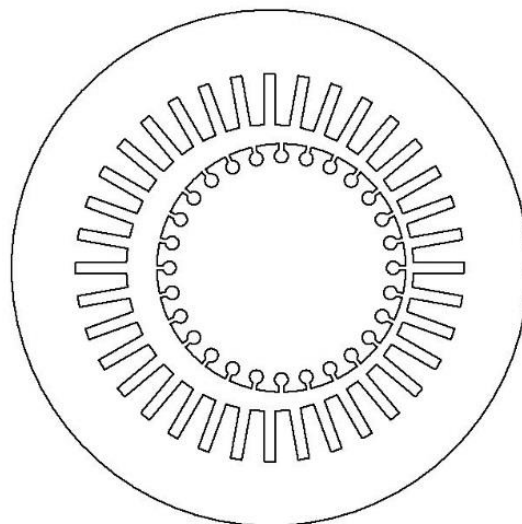


Figure 80: Rotor eccentricity

A hydrodynamic bearing has no moving components, the bearing utilises a thin film of lubricant between the journal and the bearing surfaces. The minimum thickness of the film is dependent on the mass of the journal and the velocity. The OpenHydro turbine utilises squeeze film bearings, the exact layout is commercially sensitive but Figure 81 is an indicative layout. A squeeze film bearing compresses the lubricant between the bearing surface and journal. The coil covers of the stator act as the bearing surface and the magnet covers act as the journal. The compression of the lubricant results in a positive pressure capable of supporting a load [59]. The lubricant of the OpenHydro turbine is the surrounding sea water, which contains abrasive contaminants such as grains of sand damaging the rotor and stator surfaces.

The other increase in the bearing wear is from a collision which is an immediate failure rather than a gradual failure. The eccentricity of the OpenHydro turbine has a greater impact on the magnetic circuit rather than the mechanical aspects usually associated with eccentricity. The force of a collision between the rotor and the bearing block is diminished by the lubricant. As the rotor is able to freely move within the stator frame the impact on the electric loading of the machine is of interest.

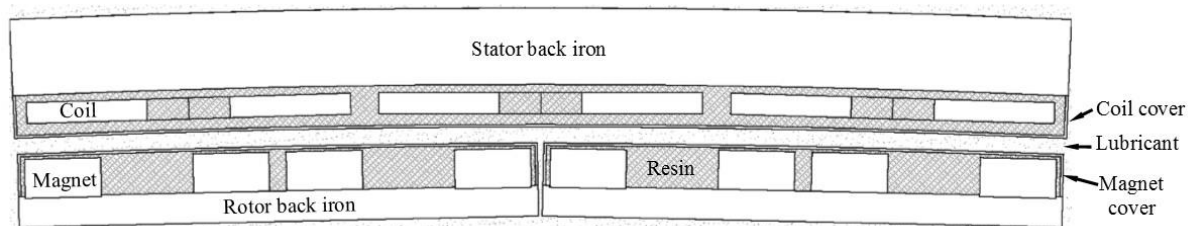


Figure 81: Hydrodynamic squeeze film bearing

5.2. Eccentricity in the permanent magnet segment

An eccentric condition in the permanent magnet generator causes unbalanced radial magnetic forces; however this effect is mitigated by the air cored coils used in the OpenHydro machine. To overcome this the turbine has complex connections between stator segments so that if a segment is damaged the coils are disconnected. This allows the turbine to continue operating at a lower power rating and limits the damage to a single segment. The cables and connector blocks used are expensive due to the generator ratings and the environmental conditions resulting in a higher manufacturing cost.

To simulate the eccentric condition on a segment the FEA permanent magnet linear model of PM-72-16, Figure 82, was set with various air gap lengths (l_g). The air gap lengths corresponded to the opening and closing of the air gap as experienced by a segment due to eccentricity. To investigate the effect of eccentricity on the EMF of a segment the model was run under no load at a linear speed corresponding to a turbine speed of 25 rpm.

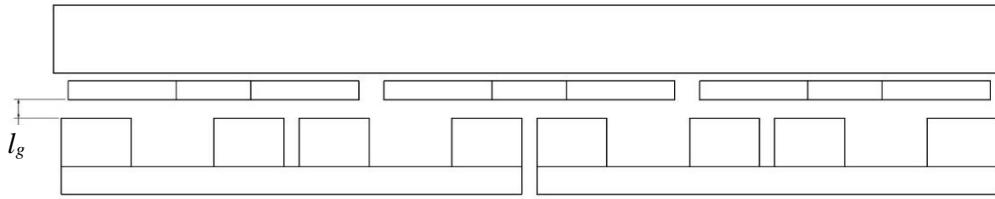


Figure 82: Permanent magnet linear model

The EMF increases, almost linearly, as the air gap closes due to eccentricity. Figure 83 shows the resultant no load EMF and air gap flux density with respect to the air gap length. The nominal air gap length is 12 mm, if the air gap closes to only 6 mm then from Figure 83 the EMF increases by 17%. Whereas the air gap of the segment 180° opposite would open to 18 mm and the EMF of that segment decreases by 14%. Under load the drop in EMF causes a reduction in the segment power, the effect of the EMF drop is dependent on the control method. A voltage control method controls the machine using the voltage and running the machine as a generator requires the voltage to be lower than the EMF. During eccentricity if the EMF drops lower than the voltage the segment behaves as a motor. A current control method would see the efficiency of the segment drop as the electric power is reduced for the same mechanical power applied.

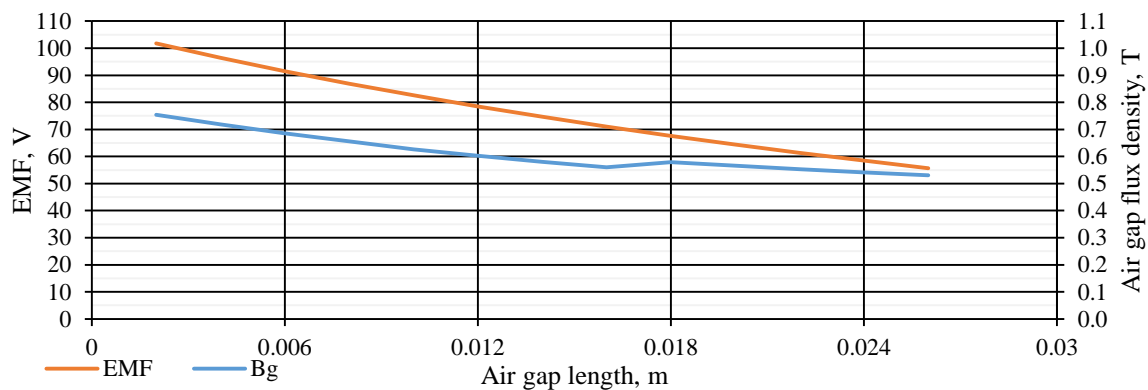


Figure 83: Graph of EMF and flux density with an eccentric condition

5.3. Eccentricity in the induction machine segment

The effect of eccentricity in the induction machine is more complicated to describe as the closing of the air gap reduces the magnetisation current of the segment. As the air gap length increases, assuming that the torque component of the current is constant, the segment current will increase due to the increase in the magnetisation current. A prolonged eccentric condition risks damaging the coils due to the higher electric loading of the segment. Connecting the opposite segments in series should balance the phase current during eccentricity.

To simulate the effect of eccentricity on a segment the linear induction machine FEA model was used, Figure 76 in Chapter 4. The model was run under loaded condition and a linear speed corresponding to a turbine speed of 25 rpm. As stated in Chapter 4 Equations (25) and (26) from [37] demonstrate that as the air gap closes the MMF and magnetisation current are reduced. The magnetisation current is a

component of the rated current. A reduction of the magnetisation current results in the rated current decreasing and Figure 84 shows the results of the FEA model. As the air gap increases the segment force decreases and inversely the rated current increases. The nominal air gap length is the same as the PM model, 12 mm, if the air gap closes to only 6 mm the current decreases by 6% and the force increases by 5% whereas air gap of the opposite segment opens to 18 mm and the current increases by 6% and force decreases by 4%.

Similar to the permanent magnet segment the current increase causes the ohmic losses to increase reducing the efficiency. Unlike the permanent magnet machine the stator teeth provide good thermal pathways.

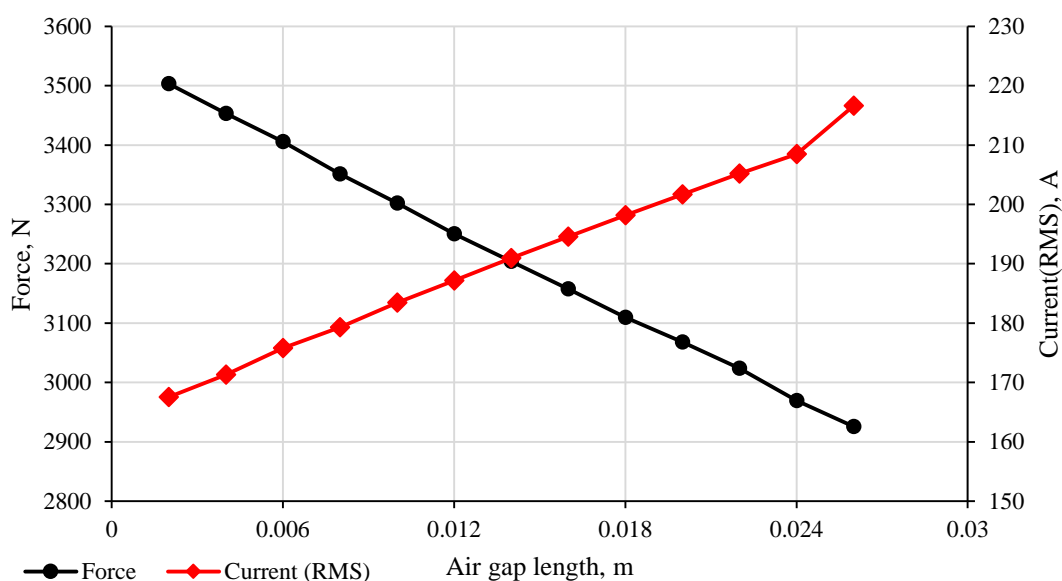


Figure 84: Linear IM segment force and current with eccentricity

5.4. Eccentricity model

Traditionally industry adopted a wait and see approach towards machine failures, investigating the cause only after a failure occurred. Health monitoring of machines uses the currents to identify faults as they develop, allowing repairs before a complete failure. Toliyat et al [60] developed an analytical model of an induction machine to identify an eccentric condition in the machine based on the stator currents. This model has been used in numerous studies of fault conditions in induction machines [61-63] and has further developed to include conditions such as axial eccentricity, saturation and skew [64, 65]. This method of modelling eccentricity is referred to as the modified winding function approach, MWFA, as it was derived from the winding function approach, WFA. The model has already been developed for the induction machine, therefore it was decided that the model would be used to investigate the eccentricity of the induction machine design. To model the permanent magnet design the MWFA could be modified at a later date. This model was used to investigate eccentricity in the fully assembled induction machine, as the FEA only provides results of a single segment. The MWFA

can represent both dynamic and static eccentricity, however only the static eccentricity is accounted for. As with static eccentricity the matrices are simpler to solve as the stator inductance is independent of rotor position, all the equations presented here are purely for static eccentricity.

5.4.1. The windings function approach

The winding function, $N(\phi)$, is determined from the turns function, $n(\phi)$, as expressed by Equation (42) [66], where $\langle n(\phi) \rangle$ is the average of the turns function. The turns function is based on the physical position of the coils in the machine. Figure 85 shows a coil in a stator frame, the turns function is formed by sweeping around the stator and assigning values of either equal to the number of conductors in the slot or zero as determined by the coil span. Equation (43) clarifies this process. The angle ϕ in Figure 85 represents the coils position relative to a fixed axis. This axis can be set anywhere on the stator periphery and independent of the rotor angle (θ_r).

$$N(\phi) = n(\phi) - \langle n(\phi) \rangle \quad (42)$$

$$n(\phi) = \begin{cases} +nn & \phi_1 \leq \phi \leq \phi_2 \\ 0 & \phi_1 > \phi > \phi_2 \end{cases} \quad (43)$$

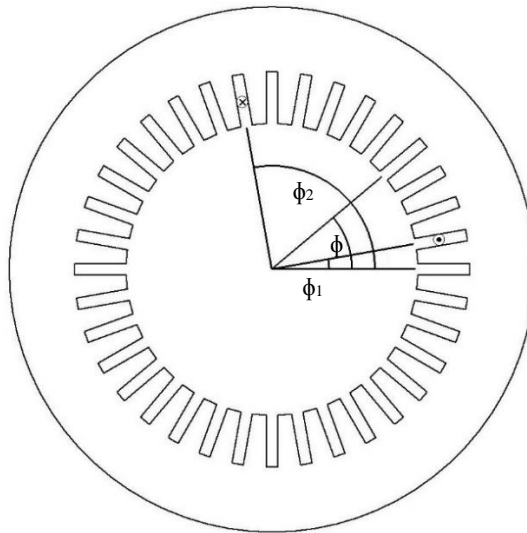


Figure 85: Stator model

The winding function of a single phase is the sum of the winding functions of all the coils within that phase (m) as expressed by Equation (44), the upper limit (a) is equal to the number of coils per phase. Figure 86 shows the phase winding function of the machine used in [60] without an eccentric condition.

$$N_m = \sum_{i=1}^a N_{mi} \quad (44)$$

Without eccentricity the air gap length is considered constant and therefore independent of the stator angle. However in the case of eccentricity this is no longer the case as the average can be calculated using Equation (45) [65]. The average turns function becomes a function of the stator angle as the air gap length varies with respect to the stator angle.

$$\langle n(\phi) \rangle = \frac{1}{2 \cdot \pi \cdot \langle l_g^{-1}(\phi) \rangle} \cdot \int_0^{2\pi} n(\phi) \cdot l_g^{-1}(\phi) d\phi \quad (45)$$

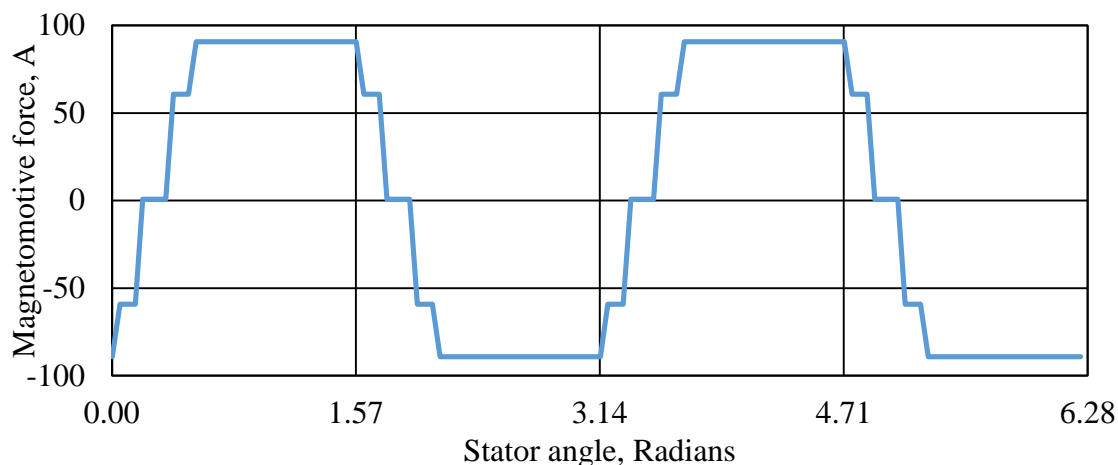


Figure 86: Winding function a single phase

The winding function of the rotor bars are determined in the same way, each bar is considered as a phase with a single turn. Figure 87 shows the winding function for a single rotor bar, each subsequent bar has the same winding function except with a displacement equal to the rotor bar slot pitch relative to the stator angle (ϕ).

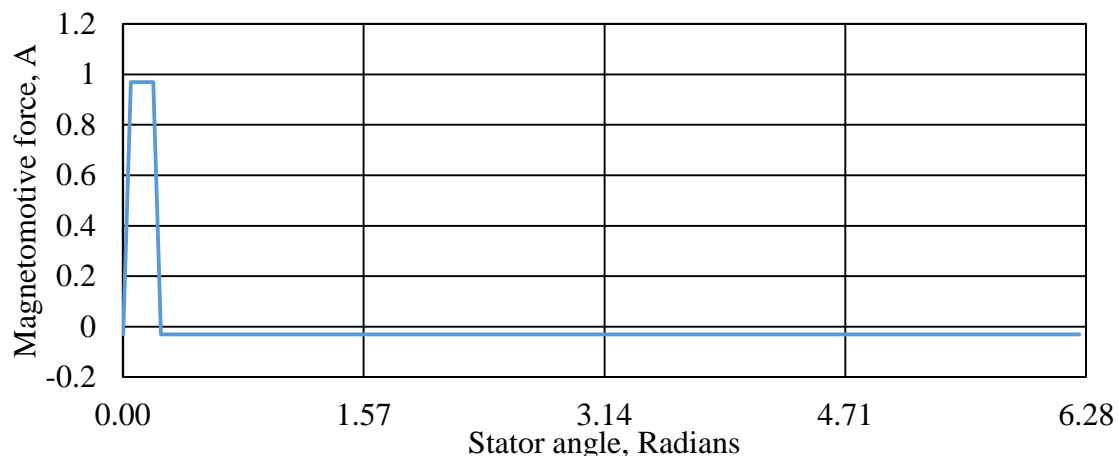


Figure 87: Winding function of a rotor bar

5.4.2. Inductance

The MWFA can be used to determine the inductances of the machine, the mutual inductance between the phase windings can be calculated by use of Equation (46) [60]. This equation needs to be modified to incorporate the eccentricity condition, the air gap length (l_g) and the average radius (r_{avg}) both need to be integrated as they are functions of the stator angle as expressed in Equation (47) [60].

$$L_{ab}(\theta_r) = \frac{\mu_0 \cdot r_{avg} \cdot l_a}{l_g} \cdot \int_0^{2\pi} N_a(\phi) \cdot n_b(\phi) d\phi \quad (46)$$

$$L_{ab}(\theta_r) = \mu_0 \cdot l_a \cdot \int_0^{2\pi} N_a(\phi) \cdot n_b(\phi) \cdot r_{avg}(\phi) \cdot l_{g1}^{-1}(\phi) d\phi \quad (47)$$

In the case of the self-inductances of the phases the turns function in Equation (47) can be removed and instead the winding function is squared as in Equation (48) [67].

$$L_{ab}(\theta_r) = \mu_0 \cdot l_a \cdot \int_0^{2\pi} (N_a(\phi))^2 \cdot r_{avg}(\phi) \cdot l_{g1}^{-1}(\phi) d\phi \quad (48)$$

The air gap length due to eccentricity in Equation (49) [60, 61] is a function of the severity of the eccentric condition and the stator angle. Where δ is the amount of static eccentricity expressed as a factor.

$$l_{g1}(\phi) = l_g - \delta \cdot l_g \cdot \cos \phi \quad (49)$$

The inverse air gap length is approximated using Equation (50) [60], the terms A_0 and A_1 are shown in Equations (51) and (52) [60, 61]. As shown in the equations for a static eccentric condition the air gap length is independent of the rotor position, however with dynamic eccentricity the air gap length is a function of the rotor position.

$$l_{g1}^{-1}(\phi) = \frac{A_0}{l_g} + \frac{A_1}{l_g} \cdot \cos \phi \quad (50)$$

$$A_0 = \frac{1}{\sqrt{1 - \delta^2}} \quad (51)$$

$$A_1 = \frac{2 - \sqrt{1 - \delta^2}}{\delta \cdot \sqrt{1 - \delta^2}} \quad (52)$$

5.5. Model validation

As discussed earlier the MWFA has been validated against practical results [60-65]. The MWFA equations in the previous sections were implemented in a Matlab script for the purpose of modelling eccentricity in the fully assembled IM machine. The same machine parameters, as presented in Toliyat's paper [60] in Table 33, were used to validate the Matlab script. The script can be found in Appendix A: Eccentricity Matlab script.

The resultant inductances calculated by the script are compared to the results presented in the paper. Figure 88, Figure 89 and Figure 90 on page 85 are graphs of various mutual inductances from the Matlab script overlapped with the results from [60], the results show good correlation to those presented in the paper. A comparison of Figure 88 and Figure 90 shows that with 50% static eccentricity the mutual inductance is no longer symmetrical.

The transient period refers to the period of time before the current and voltage of the machine settle to steady state values. During the transient period the amplitudes of the current and voltage are larger than the steady state values. As inductance affects the time constant it can be inferred that a generator with eccentricity will have a longer transient period. A prolonged transient period results in the generator operating at a higher current and voltage for a longer period of time. This reduces the life span of the conductor insulation as well as increases ohmic losses.

Table 33: 3-phase 1 hp induction motor, with double layer windings

Stator outer diameter	0.2286 m	Stator resistance	3.5332 Ω
Stator inner diameter	0.127 m	Stator leakage inductance	0.028 H
Axial length	0.102 m	Rotor bar resistance	68.34 $\mu\Omega$
Air gap length	0.000456 m	Rotor bar leakage inductance	0.28 μH
Average radius	0.0633 m	End ring segment resistance	1.56 $\mu\Omega$
Number of stator turns in series	90	End ring segment leakage inductance	0.03 μH
Number of stator slots	36	Number of slots short pitched	1
Number of poles	4	Number of rotor bars	28

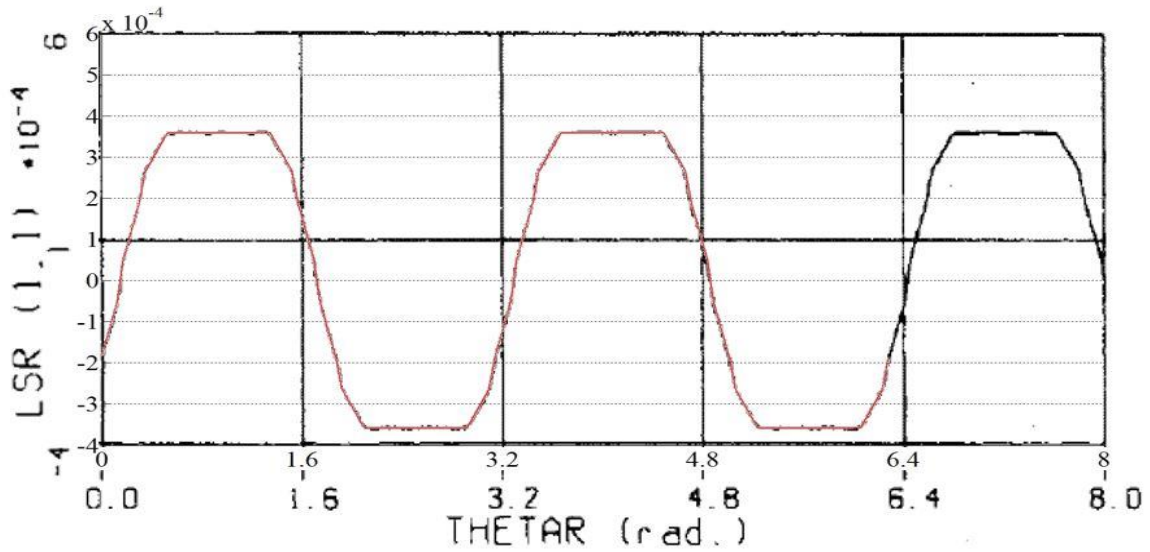


Figure 88: Results from [60] combined with the predictions from the Matlab model of the mutual inductance of stator phase a and rotor loop 1 with no eccentricity

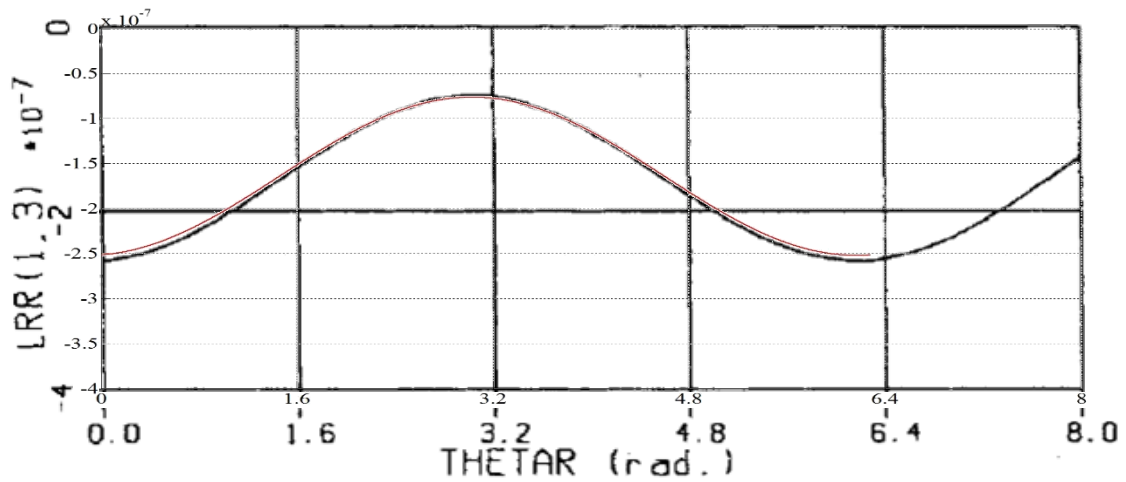


Figure 89: Results from [60] combined with the predictions from the Matlab model of the magnetising inductance of rotor loop 1 with 50% static eccentricity

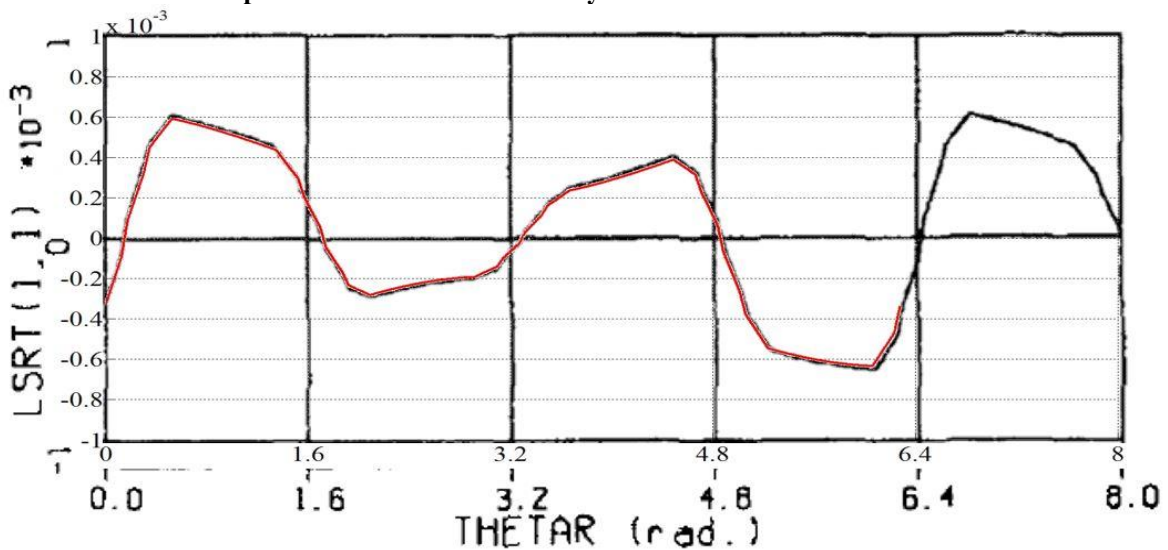


Figure 90: Results from [60] combined with the predictions from the Matlab model of the mutual inductance of stator phase a and rotor loop 1 with 50% static eccentricity

5.6. 60 Segment induction machine

The best induction machine design was selected in the discussion of Chapter 4 as the geometry of the design, IM-60-1, was used with the eccentricity model and presented in Table 34. Figure 91, Figure 92 and Figure 93 are graphs of various mutual inductances. The effect of eccentricity on the inductance is clearly shown in Figure 93 as the peak mutual inductance varies with the rotor position. There are 120 poles hence 60 inductance cycles per rotor rotation.

Table 34: IM-60-1 parameters

Stator outer diameter	14.364 m	Number of stator turns in series	32
Stator inner diameter	14.272 m	Number of stator slots	720
Axial length	0.448 m	Number of poles	120
Air gap length	0.012 m	Number of slots short pitched	0
Average radius	7.13 m	Number of rotor bars	1020

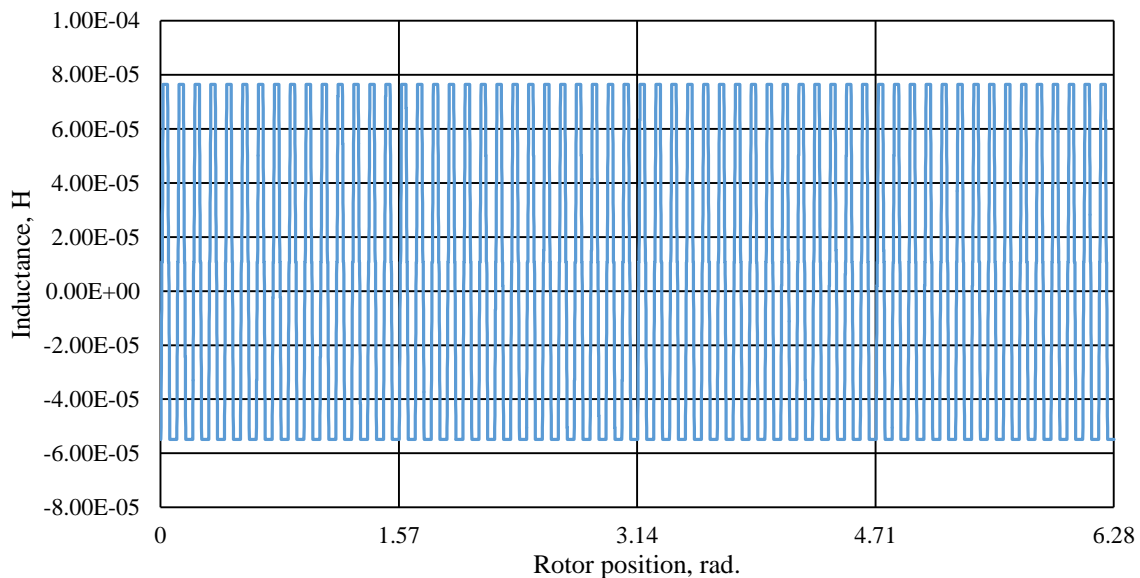


Figure 91: Mutual inductance of stator phase a and rotor loop 1 with no eccentricity from the Matlab model

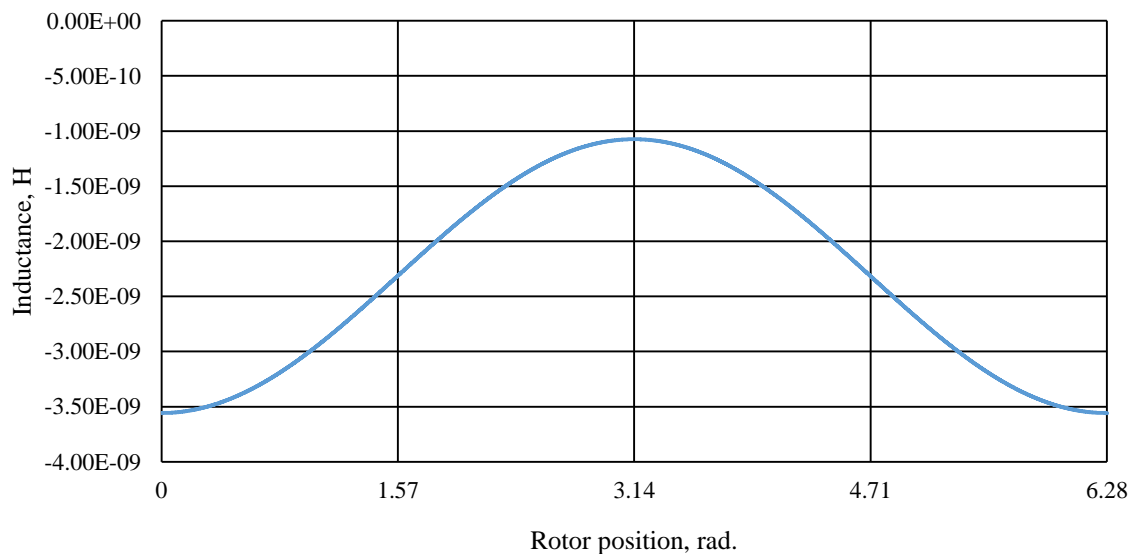


Figure 92: Magnetising inductance of rotor loop 1 with 50% static eccentricity from the Matlab model

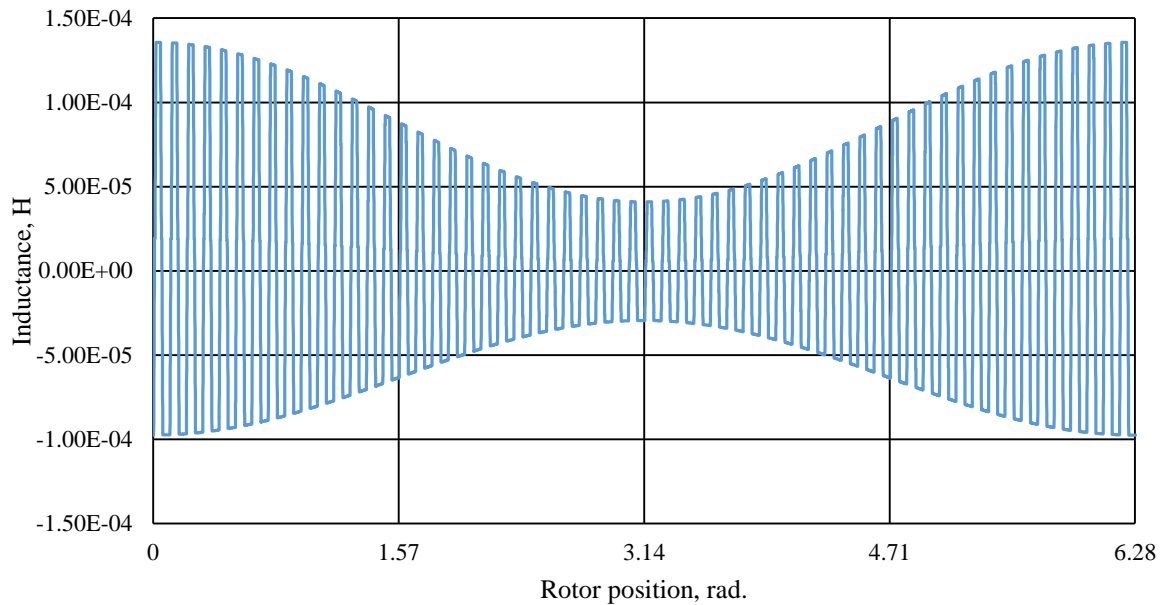


Figure 93: Mutual inductance of stator phase a and rotor loop 1 with 50% static eccentricity

Each segment has 2 poles therefore each inductance cycle represents a single segment. The segment positioned at 0 radians has a mutual inductance of 0.136 mH but the opposite segment at 3.14 radians has a mutual inductance of 0.0363 mH. The higher mutual inductance demonstrates better magnetic coupling between the stator and rotor and that the rotor is closer to the segment. The close proximity of a segment and the rotor reduces the magnetisation current. Conversely the opposite segment is further from the rotor and requires a larger magnetisation current.

5.7. Summary

The FEA segment models of both the induction machine and permanent magnet design show that the current per segment is dependent on the air gap length. As current influences the ohmic losses this reduces the efficiency of the segment, the permanent magnet design has poor thermal conductivity however the induction machine has a higher current loading. The eccentricity analytical model shows that the induction machine inductances vary significantly with eccentricity. The variation of inductance results in a longer transient period. A longer transient period is detrimental to the efficiency and the lifespan of the generator. During the transient period the amplitudes of the current and voltage are larger than the steady state values and the generator operates at a higher electric loading for a longer period of time. This increases the ohmic losses and reduces the life span of the conductor insulation.

Chapter 6. The cost of energy

This chapter aims to determine the best choice of machine for the OpenHydro tidal turbine, rather than just a comparison based on efficiency an economic model is used. The economic model allows a comparison between the permanent magnet design and the induction machine designs by assessing the designs based on the material costs as well as the power generated. The economic comparison is based on a 15 year lifetime.

6.1. Overview of key factors affecting cost

There are various costs involved with tidal turbines and to assess the best machine type for this application these costs need to be estimated fairly. The capital costs and maintenance costs need to be exceeded by the energy sold over the lifetime of the project, otherwise the project is not financially feasible.

6.1.1. Capital costs

The capital costs are the costs of the initial set up of an operational turbine, this consists of cost of material, labour and components. The deployment, installation and connection costs are also included in the capital costs. These costs are applied in the initial year.

6.1.2. Operational and maintenance costs

This is the turbine costs incurred over the operational lifetime such as maintenance costs, both planned and unplanned, observation costs and the cost of any legal requirements such as permits. These costs can be recurring depending on the frequency of planned maintenance, for example a five year maintenance cycle would apply these costs to years 5 and 10. The maintenance cost of year 15 would be omitted as the turbine would be recovered for decommissioning with a 15 year lifetime, so only the cost of recovering the turbine would be applied. The duration of maintenance also influences the income of the year as the turbine is not operational.

6.1.3. Energy supply

The energy supply cost is the most important aspect as this determines whether the project is a success or a failure. This cost can be quantified by the income earned from selling the energy produced by the turbine. Before reaching a conclusion it is important to consider how the cost of energy per turbine can vary depending on the number of deployed turbines. For a tidal turbine to be cost competitive with alternative renewable energy the cost of energy needs to be low to reduce the energy cost to consumers. It is assumed that the deployed turbine is a prototype, hence a high cost of energy is required to cover the costs of the prototype system. A strike price is the fixed price at which a commodity can be bought or sold for. For this comparison the cost of energy is assumed to be a strike price over the turbine's lifespan.

6.2. Turbine capital costs

6.2.1. Installation and deployment costs

The installation and deployment costs are high due to the fact the turbine is still within the prototype stages but in the future, when the tidal farms are fully established, the deployment costs will become negligible. The initial outlay of purchasing a single custom barge, which is adequate for an entire tidal farm, means these costs have been reduced drastically. Overall, there is a negligible difference between the permanent magnet and induction designs due to the substantial costs involved with both the installation and deployment factors. It can be assumed that the costs are the same for both machines and have, therefore, been removed from the economic model.



Figure 94: OpenHydro deployment barge [68]

6.2.2. Material costs

The permanent magnet and induction designs share some common materials, such as the electric steel and copper. Table 35 shows the costs used for calculating the machining costs of the two machines. Table 36 contains the volume of segment materials for both the induction machine and permanent magnet machine designs. The material mass is determined by the volume and density and the material costs of the designs were calculated by multiplying the cost per kilogram with the material mass. Figure 95 shows that IM-60-1 requires significantly more copper than PM-72-16 to achieve the desired performance. However Figure 95 also shows that the magnets have a significantly higher cost compared to the steel and copper. Purchase of the materials in bulk is more cost effective especially with the establishment of a dedicated production facility.

Table 35:Material cost per kilogram

<u>Materials</u>	<u>£/kg</u>
Nd-Fe-B	£ 60.00
Copper	£ 9.60
Electric steel	£ 4.00
Aluminium	£ 1.60

Table 36: Design volume per segment

Part		PM-72-16	IM-60-1
Stator	Core back, m ³	0.011956	0.011637
	End winding, m ³	0.001001	0.008171
	Copper, m ³	0.001889	0.005467
Rotor	Nd-Fe-B, m ³	0.002758	-
	Core back, m ³	0.004888	0.007533
	End ring, m ³	-	0.035928
	Bar, m ³	-	0.004227

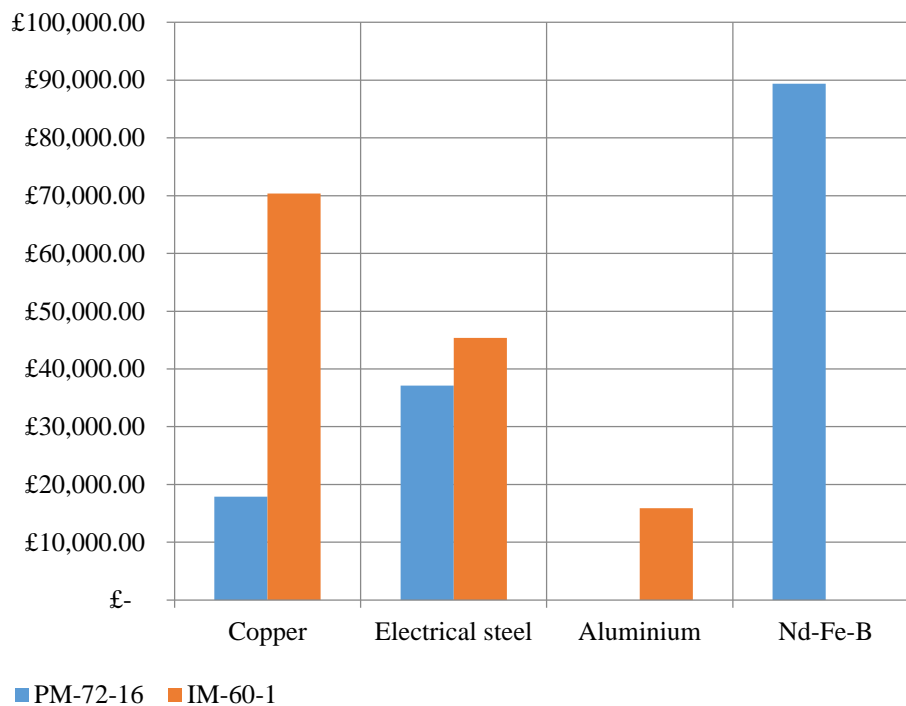


Figure 95: Material costs

6.2.3. Labour costs

Tidal turbines are an emerging technology with most devices still within the prototype stage which means, without manufacturing precedence, it is difficult to accurately estimate the labour costs. In 2012 OpenHydro produced 6 turbines over the course of a year, a turbine being produced every 2 months. To estimate labour costs, the workforce salary is only a single aspect as the facility overheads also have to be included. Size of the workforce, the machinery costs, the building rent and the facility running costs are also required. These costs are unknown quantities and several assumptions would be required. A simpler assumption would be that labour costs are similar for both the induction and permanent magnet design and therefore these costs are neglected from the economic model.

6.3. Operational and maintenance costs

These costs are difficult to predict without practical data provided from deployed prototype turbines. As the OpenHydro turbine is still in the prototype stages a fixed maintenance cycle has yet to be employed, however work is ongoing to determine the optimum method based on the existing prototypes. The maintenance costs of the induction machine are difficult to estimate based on existing machines due to the shaft-less rotor and large air gap. The maintenance costs of the induction machine are neglected from the economic model. As the comparison focuses on the generator and as the mechanical aspect of the turbine is constant the associated cost is also neglected from the economic model. Eccentricity increases the required segment current and the higher current loading increases the winding temperatures causing the winding insulation to degrade faster reducing the operational lifetime of the winding. The reduction in the winding lifetime results in maintenance becoming more frequent. The largest cost associated with the maintenance is the retrieval of the turbine and shorter periods between maintenance cycles increases these costs.

6.4. Drive system

Both the induction machine and permanent magnet machine utilise a fully rated 4 quadrant drive system with two back to back active rectifiers. However, due to the higher reactive power of the induction machine the power rating of the drives are higher. OpenHydro has developed a subsea substation capable of controlling multiple turbines referred to as the turbine control centre (TCC). The internal configuration and rating are unknown as are the involved costs; Figure 96 shows the TCC being tested. The reduction in power factor caused by eccentricity and the low power factor of the induction machine would be included with the drive costs, as a lower power factor increases the reactive power rating of the drive system and therefore its cost.



Figure 96: Turbine control centre [69]

6.5. Annual tidal energy

Figure 97 shows the annual energy extracted from the tides for each tidal speed derived from Figure 17 and Figure 11 when the tidal speed is mapped to 15 rpm. Figure 98 shows the energy extracted when the tidal speed is mapped to 25 rpm. This data combined with the efficiencies of the permanent magnet and induction machine designs for the different speeds can be used to determine the cost of energy. This data is used in the economic analysis for comparison.

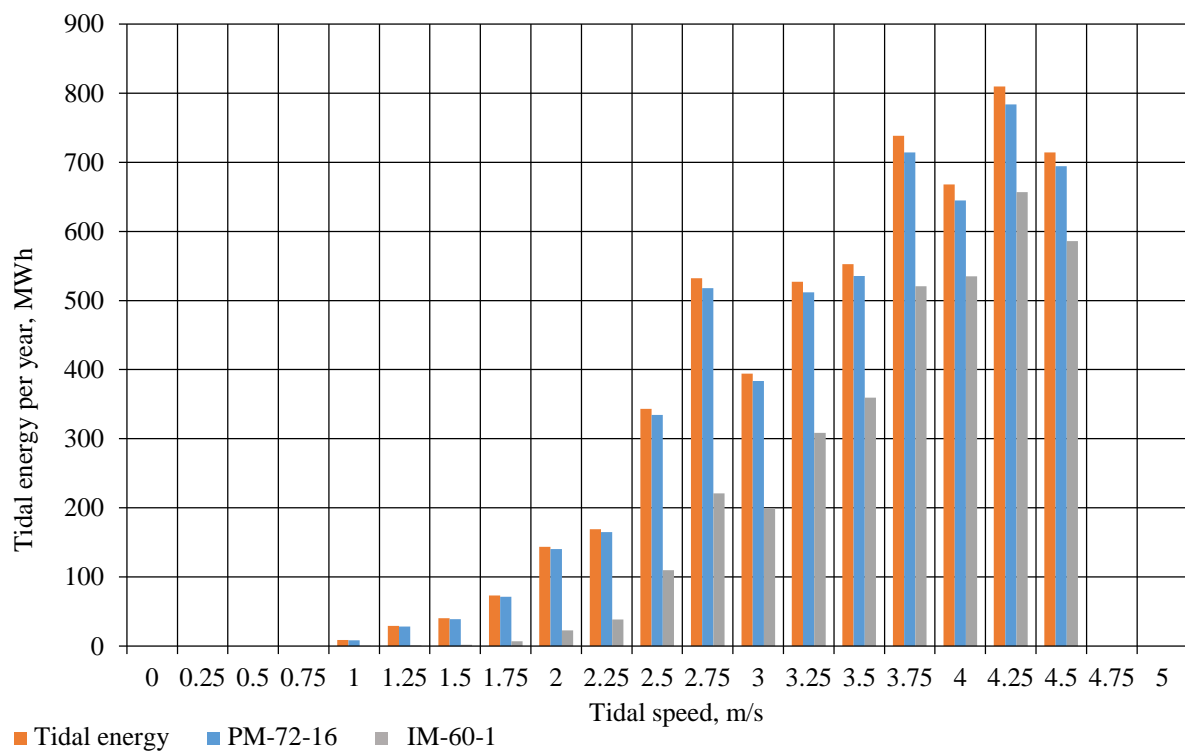


Figure 97: Annual energy extraction when 2.75 m/s is mapped to 15 rpm

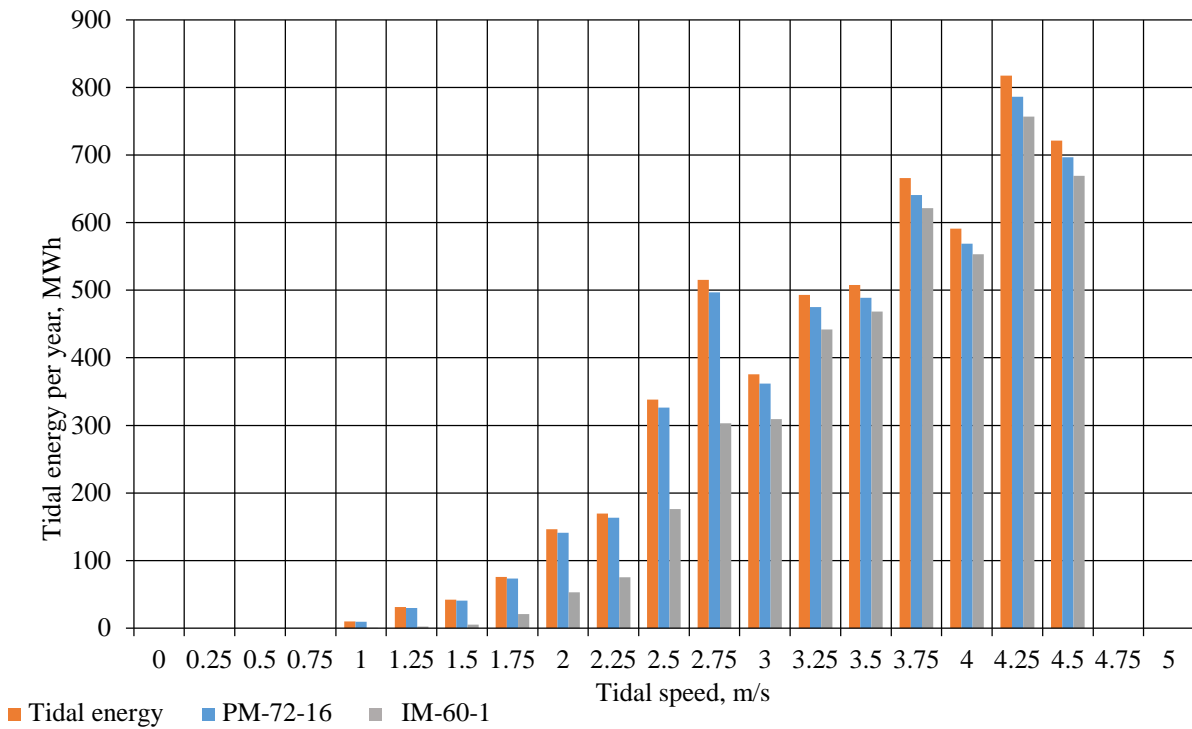


Figure 98: Annual energy extraction when 2.75 m/s is mapped to 25 rpm

6.6. Net present value

The cumulative net present value (*CNPV*) method was chosen for the comparison as the *CNPV* method is commonly used to assess potential projects. A discount factor (*DF*) of 7% was applied and the cost of energy was set as £120/MWh. The value of money is not constant, £10 15 years ago is not equal to £10 in the present, but this is accounted for by the cumulative present value factor (*CPVF*). Table 37 shows the *CPVF* values for each year of the 15 year lifetime, calculated using Equation (53) [70].

$$CPVF = \frac{1 - (1 + DF)^{-year}}{DF} \tag{53}$$

Table 37: Cumulative present value factors

Year	1	2	3	4	5	6	7	8	9	10	11	12	13	14	15
<i>CPVF</i>	0.9	1.8	2.6	3.3	4.1	4.7	5.3	5.9	6.5	7.0	7.5	7.9	8.3	8.7	9.1

Table 38 shows the yearly income of the turbine over the 15 years, these results suggest that the rate of return of the first year is 3% with the turbine becoming profitable in less than a year. However this neglects to take account of the installation and deployment costs, and the turbine may not be profitable until year 5. Another measure to compare the machines by is the profitability index (*PI*). This is the ratio of the lifetime costs and the initial capital costs. A higher *PI* signifies a more profitable venture. Table 38 shows that the induction machine has a lower capital cost but the net income of the original permanent magnet machine is higher. The profitability index of the induction machine is only slightly

higher than the permanent magnet machine for TSR_{25} . The optimised permanent magnet design has a lower capital cost than the original design and has a net income resulting in a higher profitability index.

Table 38: Net present values of the PM-72-16 and IM-60-1

Year	PM-72-0		PM-72-16		IM-60-1	
	TSR_{15}	TSR_{25}	TSR_{15}	TSR_{25}	TSR_{15}	TSR_{25}
0	-£158,029	-£158,029	-£144,368	-£144,368	-£131,652	-£131,652
1	£625,656	£595,176	£624,959	£594,288	£400,155	£499,818
2	£1,210,381	£1,151,416	£1,209,032	£1,149,698	£774,133	£966,937
3	£1,756,853	£1,671,266	£1,754,895	£1,668,773	£1,123,644	£1,403,497
4	£2,267,574	£2,157,107	£2,265,047	£2,153,889	£1,450,290	£1,811,497
5	£2,744,884	£2,611,164	£2,741,825	£2,607,269	£1,755,567	£2,192,805
6	£3,190,968	£3,035,517	£3,187,412	£3,030,988	£2,040,872	£2,549,168
7	£3,607,869	£3,432,108	£3,603,848	£3,426,988	£2,307,512	£2,882,218
8	£3,997,496	£3,802,754	£3,993,041	£3,797,081	£2,556,709	£3,193,479
9	£4,361,633	£4,149,152	£4,356,773	£4,142,962	£2,789,603	£3,484,378
10	£4,701,949	£4,472,888	£4,696,709	£4,466,215	£3,007,261	£3,756,245
11	£5,020,000	£4,775,446	£5,014,406	£4,768,322	£3,210,680	£4,010,327
12	£5,317,245	£5,058,210	£5,311,319	£5,050,664	£3,400,791	£4,247,787
13	£5,595,044	£5,322,475	£5,588,809	£5,314,535	£3,578,465	£4,469,712
14	£5,854,669	£5,569,452	£5,848,144	£5,561,143	£3,744,515	£4,677,118
15	£6,097,309	£5,800,272	£6,090,514	£5,791,619	£3,899,702	£4,870,956
Net income	£5,939,280	£5,642,243	£5,946,146	£5,647,251	£3,768,050	£4,739,304
<i>P.I.</i>	38.58	36.70	42.19	40.12	29.62	37.00

6.7. Summary

Certain aspects have been neglected from the comparison, such as labour costs, as it is difficult to estimate the actual time frame required to build either machine. Maintenance costs are also neglected as the cost of extraction significantly exceeds any maintenance or manufacturing costs, this is purely due to the deployment environment. In the future, when the infrastructure is in place, this may not be the case. Although at the time of writing the generator accounts for, at most, 10% of the overall project cost.

The capital cost of the induction machine design is 17% lower than that of the permanent magnet, however, over a 15 year lifetime the net income of the induction machine is 16% lower at a rated speed of 25 rpm. In comparison at a rated speed of 15 rpm the net income of the induction design is 37% lower due to the low efficiency. It is evident that the profitability index of the induction machine is lower than the original permanent magnet design. The optimised permanent magnet design has 0.1% higher net income and a 9% lower capital cost than the original permanent magnet design. Furthermore, the profitability index is higher than both the original and induction machine.

Chapter 7. Conclusion

7.1. Overview

From the reviewed literature the squirrel cage induction machine was chosen as an alternative design to the permanent magnet machine. The removal of rare earth magnet content for the direct drive turbine was an opportunity to improve the cost competitiveness of the OpenHydro tidal turbine to alternative renewable energy sources.

Both the permanent magnet and induction machine were segmented, which simplifies the construction and assembly of the turbine. It also improves the fault tolerance of the turbine depending on the coil connections.

7.1.1. Permanent magnet optimisation

The permanent magnet design underwent both manual and numerical optimisation with a simplified linear FEA model. The results of the optimisation showed that the magnet mass could be reduced with minimum impact on the performance of the generator.

7.1.2. Squirrel cage induction generator

The induction machine segment was wrapped to form a rotary induction machine, the conventional design process was then applicable. The number of segments were investigated with FEA models of three designs; the best design was then manually optimised. The study produced a model that was comparable to the permanent magnet generator performance.

7.1.3. Eccentricity

The effect of eccentricity on the individual segments of both the permanent magnet and induction machine was investigated using linear FEA models. A numerical model, based on published work, was created to evaluate the effect on the fully assembled generator.

7.1.4. The cost of energy

The material costs of the permanent magnet and induction machine were calculated for comparison. The available power of a deployment site was calculated, then the efficiencies of the two generators across the speed range were applied to determine the power extraction. The cost of this energy sold was then used to compare the two generators over a 15 year lifetime.

7.2. Permanent magnet generator

The original model of the permanent magnet generator included features that had no effect on the magnet circuit such as chamfers and bolts, these features increased the computation time to solve the model due to the unnecessary mesh. The model has been simplified with a significant reduction in computation time and due to the scale of the turbine the model can be made linear with little effect on the results. A design study using the simplified linear model has been conducted where the magnet dimensions were modified to identify an optimum magnet mass for the generator. The study identified that the magnet height could be reduced up to 11% with little effect on the average force. The best design from the design studies achieved a mass reduction of 13% with a force reduction of 5% by reducing the magnet height.

7.3. Squirrel cage induction generator

The induction machine was chosen as the alternative to the permanent magnet machine due to the lack of expensive rare earth magnetic material. Three induction machines based on different numbers of segments have been created and the designs were then taken forward for redesign. The 100 segment design has the least flexibility in its design and it was found that the alternative achieved a high power factor at the expense of efficiency. The original 40 segment design failed to meet the specification; however, the redesign achieved the rated power with a low efficiency and power factor. The 60 segment design has been through four redesigns, the first improved the efficiency and the power factor. The first redesign of the 60 segment, IM-60-1, was chosen for the comparison as it has the best efficiency of all the designs and the best power factor of the 60 segment designs

A linear model has been created based on the segment model IM-60-1, the translator was shorter due to shorter circumference of the rotor this introduced a severe spatial harmonic to the force. By widening the rotor teeth the spatial harmonic was removed.

7.4. Eccentricity

The OpenHydro turbine has a shaft-less rotor which allows the rotor to move freely within the stator frame. To investigate the effect of eccentricity on the induction machine and the permanent magnet machines the FEA linear models were set with varying air gap lengths. The FEA segment models of both the induction machine and permanent magnet design showed that the current per segment was dependent on the air gap length. But as the current influences the ohmic losses this reduces the efficiency of the segment. The permanent magnet design has poor thermal conductivity and high operating temperatures, causing the winding insulation to degrade faster reducing the lifetime of the coil. However the induction machine has a higher current loading resulting in higher losses and, due to the varying phase inductance, a lower power factor.

The FEA models focused on the effect on a single segment to model the eccentricity effect on the fully assembled machine and an analytical model from published literature was scripted. The eccentricity analytical model showed that the induction machine inductances vary significantly with eccentricity. The inductance influences the settling time to steady state values and the power factor of the machine.

7.5. The cost of energy

To compare the designs it was decided that an economic analysis would be the fairest method as both the machine performance and the material costs are assessed. The cumulative net present value method was chosen for the comparison, the *CNPV* method is commonly used to assess potential projects. Certain aspects have been neglected from the comparison, such as labour costs as it is difficult to estimate the actual time frame required to build either machine. Maintenance costs are also neglected as the cost of extraction significantly exceeds any maintenance or manufacturing costs as this is purely due to the deployment environment. In the future when the infrastructure is in place this may not be the case, however the generator accounts for 10% of the overall project costs at the time of writing.

The machines are both considered to have a lifetime of 15 years. Another measure to compare the machines is the profitability index, this is the ratio of the lifetime costs and the initial capital costs. A higher profitability index signifies a more profitable venture.

The capital cost of the induction machine design is 17% lower than that of the permanent magnet, however over a 15 year lifetime the net income of the induction machine is 16% lower when the tidal speed is mapped to a turbine speed of 25 rpm. When the tidal speed is mapped to 15 rpm, the net income of the induction machine is 37% lower corresponding to the lower efficiency. The profitability index of the induction machine is lower than the original permanent magnet design. The optimised permanent magnet design has 0.1% higher net income and a 9% lower capital cost than the original permanent magnet design. The profitability index is higher for the optimised permanent magnet design than both the original and induction machine.

7.6. Future work

Changing the winding of the induction machine from a concentric broken chain winding to a concentrated single tooth winding reduces the end winding length. The short end winding reduces the stator phase resistance, however this type of winding increases MMF harmonics of the design. It is expected that the large air gap would filter the harmonics due to the fringing effect of the magnetic field. The single tooth winding significantly increases the number of poles and the power factor has squared proportional relationship with the number of poles. The frequency is also dependent on the number of poles as the stator and rotor leakage reactance increase proportionally to the frequency.

As an example: using the 40 segment design for a coil span of 1 (a single tooth winding) with 24 stator slots, 20 poles are required compared to the original 2 per segment. As a result for 40 segments the total number of poles increases from 80 to 800 and the frequency increases from 16.6 Hz to 166 Hz.

The MWFA model was used to a degree to investigate the effect of eccentricity with regards to the fully assembled induction machine. A similar investigation can be done for the permanent magnet machine based on [71]. The MWFA model originated with a synchronous machine therefore it should be possible to adapt the MWFA to work for the permanent magnet design.

From the FEA models the effect of eccentricity on a single segment was observed whereas with the MWFA model only the phase components could be observed. Through the observations of the MWFA it was found that the phase voltage and current is dependent on the segment connections and that the MWFA is based on the MMF, it is independent of the coil connections. To investigate the optimum coil connections to mitigate the effect of eccentricity, further work may include modification of the MWFA to accommodate the coil connections.

The number of segments could be further investigated as the 40 segment design could be adapted to provide a 20 segment design. The segment arc length of the 20 segment design would be equivalent to the arc length of two connected 40 segments. Likewise an 80 segment design could be viewed as half the 40 segment design. From the 60 segment design a 30 and a 120 segment design could be developed and the 100 segment could provide 50 and 200 segment designs. Though the 120 and 200 segments are not feasible due to the restricted volume of the segment.

During the course of the project it was observed that work regarding transmission methods for offshore renewable energy sources was on-going. The use of DC transmission offered lower losses compared to AC transmission which presented the idea of combining each segment with an active rectifier. The segment could then be controlled individually and monitored. The power would be delivered to shore by DC transmission with an additional cable for the data from the built in active rectifiers. The power could then be converted by an onshore substation and fed to the grid.

7.7. Summary

The permanent magnet generator of the OpenHydro turbine has been successfully optimised with little loss in performance for a reduction in rare earth magnetic material. The squirrel cage induction machine was identified as a possible alternative to the permanent magnet design, the resultant design has been over rated for this application. The lower efficiencies of the induction machine across the turbine speed range reduces the possible net income of the generator over a 15 year lifetime. The permanent magnet machine has a higher capital cost than the induction machine but achieves good efficiency across the turbine speed range. This results in a high net income that offsets the high material costs of the permanent magnet generator.

To conclude, the present induction machine design is not competitive with the optimised permanent magnet design and it can be recommended that the permanent magnet design is the best choice for the application of a large air gap direct drive tidal turbine.

Appendix A: Eccentricity Matlab script

A1. Validation model script

```
%System Variables
H = 3048;           %Number of samples
dx = 2*pi/H;       %Number of steps in radians

%Stator Variables
nn = 30;           %Number of turns per coil
Ns = 36;           %Number of stator slots
As = 2*pi/Ns;      %Stator mechanical angle
Pp = 2;            %Number of pole pairs
q = Ns/(3*2*Pp);
Beta = 2*pi*Pp/Ns; %Beta is the electrical angle between adjacent stator slots
Alpha = Beta*1;    %Alpha = Beta*Number of slots short pitched
%Rotor Variables

Nr = 28;           %Number of rotor slots
Ar = 2*pi/Nr;      %Rotor mechanical angle
BarNo = 1;

%Preallocating Arrays
count = 1;         %Counter for the arrays
Coilna = zeros(1,H);
Phi2 = zeros(1,H);
Barna = zeros(Nr,H);
BarNa = zeros(Nr,H);
NaNb = zeros(1,H);
NaNc = zeros(1,H);
NbnC = zeros(1,H);
Igeff = zeros(1,H);
geff = zeros(1,H);
AvgR = zeros(1,H);
Rr = zeros(Nr+1,Nr+1);

ICoilNaBarna = zeros(Nr,H);
ICoilNbBarna = zeros(Nr,H);
ICoilNcBarna = zeros(Nr,H);
Barna1 = zeros(Nr,H);
BarNa1 = zeros(Nr,H);
MBarna = zeros(Nr,H);
MBarNa = zeros(Nr,H);
IBar = zeros(Nr,H,Nr);

for phi = 0:dx:2*pi-dx,
    if((phi>=As)&&(phi<=pi/2))||((phi>pi+As)&&(phi<=3*pi/2)),
        Coilna(1,count) = +nn;
    else
        Coilna(1,count) = 0;
    end
    if((phi>0+2*As)&&(phi<=(pi/2+As))||((phi>pi+2*As)&&(phi<=(3*pi/2+As))),
        Coilna(2,count) = +nn;
    else
        Coilna(2,count) = 0;
    end
    if((phi>0+3*As)&&(phi<=(pi/2)+(2*As))||((phi>(pi)+(3*As))&&(phi<=(3*pi/2)+(2*As))),
        Coilna(3,count) = +nn;
    else
        Coilna(3,count) = 0;
    end
end
```

```

if((phi>(0))&&(phi<=(pi/2+As))||((phi>(pi))&&(phi<=(3*pi/2+As))),
    Coilna(4,count) = +nn;
else
    Coilna(4,count) = 0;
end
if((phi>(0+As))&&(phi<=(pi/2)+2*As))||((phi>(pi+As))&&(phi<=(3*pi/2+2*As))),
    Coilna(5,count) = +nn;
else
    Coilna(5,count) = 0;
end
if((phi>(0)+(2*As))&&(phi<=(pi/2)+3*As))||((phi>(pi)+(2*As))&&(phi<=(3*pi/2)+3*As)),
    Coilna(6,count) = +nn;
else
    Coilna(6,count) = 0;
end
Phi2(count) = phi;
count = count+1;
end;
count = 1;
%Rotor Turns Function
label = 'Rotor turns function';
disp(label)
for BarNo = 1:1:Nr,
    for phi = 0:dx:2*pi-dx,
        if((phi>(BarNo-1)*Ar)&&(phi<=BarNo*Ar)),
            Barna(BarNo,count) = 1;
        else
            Barna(BarNo,count) = 0;
        end
        count = count+1;
    end;
    count = 1;
    BarNa(BarNo,:) = Barna(BarNo,:)-mean(Barna(BarNo,:));
end

%-----%
%Modified Winding Function Approach
U0 = 4*pi*10^-7;           %Permeability of vacuum
Rrotor = 0.07;             %Rotor radius, m
Rstator = 0.063525019;    %Stator inner radius, m
g = 0.000456438;         % Air gap length, m
% AvgR = Rs - g/2;        % Average radius, m
la = 0.1024128;          % Axial length, m
Igeff1 = g^-1;

dg = 1*10^-32;           % Rotor deviation approximately zero for no eccentricity condition

A0 = 1/(g*sqrt(1-dg^2));
A1 = 2*(1-sqrt(1-dg^2))/(g*dg*sqrt(1-dg^2));
count = 1;
for phi = 0:dx:2*pi-dx,
    geff(1,count) = g - dg*g*cos(phi);
    Igeff(1,count) = A0+A1*cos(phi);
    AvgR(1,count) = Rstator - geff(1,count)/2;
    count = count + 1;
end;

Shift = floor(As*q/dx);%Pp*dx);
Coilna1 = Coilna;
Coilna = sum(Coilna);
Coilnb = circshift(Coilna,[0 2*Shift]);
Coilnc = circshift(Coilna,[0 4*Shift]);

```

```

MCoilNa = sum(CoilNa.*Igeff)*(2*pi-dx)/(2*pi*H*A0);
MCoilNb = sum(CoilNb.*Igeff)*(2*pi-dx)/(2*pi*H*A0);
MCoilNc = sum(CoilNc.*Igeff)*(2*pi-dx)/(2*pi*H*A0);

MCoilNa = CoilNa - MCoilNa;
MCoilNb = CoilNb - MCoilNb;% circshift(MCoilNa,[0 2*Shift]);
MCoilNc = CoilNc - MCoilNc;%-1*circshift(MCoilNa,[0 Shift]);

for BarNo = 1:1:Nr,
    MBarna(BarNo,:) = sum(Barna(BarNo,:).*Igeff)*2*pi/(2*pi*H*A0);%*2*pi/H;
    MBarNa(BarNo,:) = Barna(BarNo,:) - MBarna(BarNo,:);
end;
%-----%
% Inductance
Constant = U0*la;

% Stator Inductance
Laa = Constant*sum(AvgR.*Igeff.*MCoilNa.*CoilNa)*(2*pi-dx)/H;
Lbb = Constant*sum(AvgR.*Igeff.*MCoilNb.*CoilNb)*(2*pi-dx)/H;
Lcc = Constant*sum(AvgR.*Igeff.*MCoilNc.*CoilNc)*(2*pi-dx)/H;

Lac = Constant*sum(AvgR.*Igeff.*MCoilNa.*CoilNc)*(2*pi-dx)/H;
Lab = Constant*sum(AvgR.*Igeff.*MCoilNa.*CoilNb)*(2*pi-dx)/H;
Lbc = Constant*sum(AvgR.*Igeff.*MCoilNb.*CoilNc)*(2*pi-dx)/H;

Lss(1,1) = Laa;
Lss(1,2) = Lab;
Lss(1,3) = Lac;
Lss(2,1) = Lab;
Lss(2,2) = Lbb;
Lss(2,3) = Lbc;
Lss(3,1) = Lac;
Lss(3,2) = Lbc;
Lss(3,3) = Lcc;

% Mutual & Rotor Inductance
count = 1;
for BarNo = 1:1:Nr,
    for RotorPos = 0:dx:2*pi-dx,
        Shift = floor(RotorPos/dx);
        Barna1(BarNo,:) = circshift(Barna(BarNo,:),[0 Shift]);
        %BarNa1(BarNo,:) = circshift(MBarNa(BarNo,:),[0 Shift]);

        ICoilNaBarna(BarNo,count) = sum(MCoilNa.*Barna1(BarNo,:).*Igeff.*AvgR)*2*pi/H;
        ICoilNbBarna(BarNo,count) = sum(MCoilNb.*Barna1(BarNo,:).*Igeff.*AvgR)*2*pi/H;
        ICoilNcBarna(BarNo,count) = sum(MCoilNc.*Barna1(BarNo,:).*Igeff.*AvgR)*2*pi/H;

        %IBar(BarNo,count) = sum(BarNa1(BarNo,:).*Barna1(BarNo,:).*Igeff.*AvgR)*2*pi/H;
        count = count + 1;
    end;
    count = 1;
end;

Lar = Constant.*ICoilNaBarna;
Lbr = Constant.*ICoilNbBarna;
Lcr = Constant.*ICoilNcBarna;
Lsr(:,1) = Lar;
Lsr(:,2) = Lbr;
Lsr(:,3) = Lcr;

```

```

Barna1 = zeros(Nr,H);
for BarNoZ = 1:1:Nr,
    for BarNo = 1:1:Nr,
        for RotorPos = 0:dx:2*pi-dx,
            Shift = floor(RotorPos/dx);
            Barna1(BarNo,:) = circshift(Barna(BarNo,:),[0 Shift]);
            BarNa1(BarNoZ,:) = circshift(BarNa(BarNoZ,:),[0 Shift]);
            IBar(BarNo,count,BarNoZ) = sum(BarNa1(BarNoZ,:).*Barna1(BarNo,:).*Igeff.*AvgR)*2*pi/H;
            count = count + 1;
        end;
        count = 1;
    end;
end;
Lbar = Constant.*IBar;

%-----%
% Voltage and Current

f = 60;
H1 = 128;                % Number of samples
dX = (1/f)/H1;          % Timestep
CycleNo = 30;
S = 0.01;                % Slip
phi = 0:dX:CycleNo*(1/f);
Va = 294*cos((2*pi*f*phi)-(2*pi/3));
Vb = 294*cos((2*pi*f*phi)+(2*pi/3));
Vc = 294*cos((2*pi*f*phi));
Vs =[Va;Vb;Vc];

Vr = zeros(Nr+1,CycleNo*H1+1);    %Preallocating array

V = [Vs;Vr];
AngVel = 2*pi*(f/Pp);            %Synchronous speed in Rad/S

Kps = cos(Alpha/2);
Kds = (sin(q*Beta/2))/(q*sin(Beta/2));
Kws = Kps * Kds;

Ke = 0.5/(Kws*90);
Ki = (3*Kws*90)/(Nr*0.5*1);

R1 = 3.5332;                    %Stator phase resistance, ohms
Rb = 68.34*10^-6;                %Rotor bar resistance, ohms
Re = 1.56*10^-6;                %End ring resistance, ohms

Ls = 0.028;                      %Stator leakage inductance, H
Lb = 0.28*10^-6;                %Rotor bar leakage inductance, H
Le = 0.03*10^-6 ;              %End ring leakage inductance, H

% Rotor bar resistance matrix
for BarNoZ = 1:1:Nr+1,
    for BarNo = 1:1:Nr+1,
        if (BarNo == BarNoZ),
            Res = 2*(Rb + Re);
        elseif (BarNo == BarNoZ+1||BarNo == BarNoZ-1||BarNo == Nr && BarNoZ
==1||BarNo==1&&BarNoZ==Nr),
            Res = -Rb;
        else
            Res = 0;
        end;
    end;
end;

```

```

    if (BarNo == Nr+1||BarNoZ==Nr+1),
        Res = -Re;
    end;

    if(BarNo== Nr+1&&BarNoZ == Nr+1),
        Res = Nr*Re;
    end;

    Rr(BarNoZ, BarNo) = Res;           %Rotor resistance

end;
end;

%Rotor inductance matrix
Lrr = zeros(Nr,H,Nr);                % Preallocating array

TempMatrix = zeros(1,Nr);
AddMatrix =zeros(Nr,Nr);

TempMatrix(1,1) = 2*(Lb+Le);
TempMatrix(1,2) = -Lb;
TempMatrix(1,end) = -Lb;
AddMatrix(1,:) = TempMatrix;
for Count = 2:1:Nr,
    AddMatrix(Count,:) = circshift(TempMatrix,[0,Count]);
end;

for Count = 1:1:H,
    Lrr(:,Count,:) = squeeze(Lbar(:,Count,:)) + AddMatrix;
end;
TempMatrix = zeros(1,H,Nr);
TempMatrix(1,:) = Le;
Lrr = [Lbar;TempMatrix];
Lrr(:,end+1) = Le;
Lrr(end,:,end) = Nr*Le;

Rs = [R1 0 0;0 R1 0; 0 0 R1];

dLsr = diff(Lsr,1,2)/dx;             %Differentiation of Lsr
dLsr(:,end+1,:) = 0;

Rrref = (Ki/Ke).*Rr;
Lrrref = (Ki/Ke).*Lrr;

```

A2. 60 Segment script

```

%System Variables
SegNum = 60;           %Number of segments
SegAngle = 2*pi/SegNum; %Segment angle in rads
H1 = 256;             %Number of samples per segment
dx = SegAngle/H1;    %Number of steps in rads per segment
H = H1*SegNum;       %Number of samples

%Stator Variables
nn = 32;              %Number of turns per coil
Ns = 720;             %Number of stator slots
As = 2*pi/Ns;        %Stator slot mechanical angle
Pp = 60;              %Number of pole pairs
q = Ns/(3*2*Pp);     %Number of slots per phase per pole pair
Beta = 2*pi*Pp/Ns;   %Beta is the electrical angle between adjacent stator slots
Alpha = Beta*1;      %Alpha = Beta*Number of slots short pitched
m = 3;                %Number of phases

%Rotor Variables

Nr = 1020;            %Number of rotor slots
Ar = 2*pi/Nr;        %Rotor mechanical angle
BarNo = 1;

%Preallocating Arrays
count = 1;            %Counter for the arrays
Coilna = zeros(2,H);
Coilna1 = zeros(2,H1);
Phi2 = zeros(1,H);
Barna = zeros(Nr,H);
BarNa = zeros(Nr,H);
NaNb = zeros(1,H);
NaNc = zeros(1,H);
NbnC = zeros(1,H);
Igeff = zeros(1,H);
geff = zeros(1,H);
AvgR = zeros(1,H);
Rr = zeros(Nr+1,Nr+1);

ICoilNaBarna = zeros(Nr,H);
ICoilNbBarna = zeros(Nr,H);
ICoilNcBarna = zeros(Nr,H);
Barna1 = zeros(Nr,H);
BarNa1 = zeros(Nr,H);
MBarna = zeros(Nr,H);
MBarNa = zeros(Nr,H);
%IBar = zeros(Nr,H,Nr);

%Stator Turns Function
for phi = 0:dx:SegAngle-dx,
    if((phi>=As)&&(phi<=As*q*m)),%||(phi>pi+As)&&(phi<=3*pi/2)),
        Coilna1(1,count) = +nn;
    else
        Coilna1(1,count) = 0;
    end
end

```

```

if((phi>0+2*As)&&(phi<=(As*q*m+As)),%||(phi>pi+2*As)&&(phi<=(3*pi/2+As))),
    Coilna1(2,count) = +nn;
else
    Coilna1(2,count) = 0;
end
count = count+1;
end;

count = 1;

%Rotor Turns Function
for BarNo = 1:1:Nr,
    for phi = 0:dx:2*pi-dx,
        if((phi>(BarNo-1)*Ar)&&(phi<=BarNo*Ar)),
            Barna(BarNo,count) = 1;
        else
            Barna(BarNo,count) = 0;
        end
        count = count+1;
    end;
    count = 1;
    BarNa(BarNo,:) = Barna(BarNo,:)-mean(Barna(BarNo,:));
end

%-----%
%Modified Winding Function Approach
U0 = 4*pi*10^-7;           %Permeability of vacuum
Rrotor = 7.124;           %Rotor radius, m
Rstator = 7.136;         %Stator inner radius, m
g = 0.012;               %Air gap length, m
%AvgR = Rs - g/2;       %Average radius, m
la = 0.4482;            %Axial length, m
Igeff1 = g^-1;

dg = 1*10^-32;         %Rotor deviation approximately zero for no eccentricity condition

A0 = 1/(g*sqrt(1-dg^2));
A1 = 2*(1-sqrt(1-dg^2))/(g*dg*sqrt(1-dg^2));
count = 1;
for phi = 0:dx:2*pi-dx,
    geff(1,count) = g - dg*g*cos(phi);
    Igeff(1,count) = A0+A1*cos(phi);
    AvgR(1,count) = Rstator - geff(1,count)/2;
    count = count + 1;
end;

Shift = floor(As*q/dx;%Pp*dx));

Coilna = repmat(Coilna1,1,SegNum);
Coilna = sum(Coilna);
Coilnb = circshift(Coilna,[0 2*Shift]);
Coilnc = circshift(Coilna,[0 4*Shift]);

MCoilna = sum(Coilna.*Igeff)*(2*pi-dx)/(2*pi*H*A0);
MCoilnb = sum(Coilnb.*Igeff)*(2*pi-dx)/(2*pi*H*A0);
MCoilnc = sum(Coilnc.*Igeff)*(2*pi-dx)/(2*pi*H*A0);

```

```

MCoilNa = Coilna - MCoilna;
MCoilNb = Coilnb - MCoilnb;%circshift(MCoilNa,[0 2*Shift]);
MCoilNc = Coilnc - MCoilnc;%-1*circshift(MCoilNa,[0 Shift]);

for BarNo = 1:1:Nr,
    MBarna(BarNo,:) = sum(Barna(BarNo,:).*Igeff)*2*pi/(2*pi*H*A0);%*2*pi/H;
    MBarNa(BarNo,:) = Barna(BarNo,:) - MBarna(BarNo,:);
end;

```

A3. 60 Segment inductance calculations script

```
Constant = U0*la;
```

```
%Stator Inductance
```

```
Laa = Constant*sum(AvgR.*Igeff.*MCoilNa.*Coilna)*(2*pi-dx)/H;
Lbb = Constant*sum(AvgR.*Igeff.*MCoilNb.*Coilnb)*(2*pi-dx)/H;
Lcc = Constant*sum(AvgR.*Igeff.*MCoilNc.*Coilnc)*(2*pi-dx)/H;
```

```
Lac = Constant*sum(AvgR.*Igeff.*MCoilNa.*Coilnc)*(2*pi-dx)/H;
Lab = Constant*sum(AvgR.*Igeff.*MCoilNa.*Coilnb)*(2*pi-dx)/H;
Lbc = Constant*sum(AvgR.*Igeff.*MCoilNb.*Coilnc)*(2*pi-dx)/H;
```

```
Lss(1,1) = Laa;
Lss(1,2) = Lab;
Lss(1,3) = Lac;
Lss(2,1) = Lab;
Lss(2,2) = Lbb;
Lss(2,3) = Lbc;
Lss(3,1) = Lac;
Lss(3,2) = Lbc;
Lss(3,3) = Lcc;
```

```
%Mutual & Rotor Inductance
```

```
count = 1;
```

```
for BarNo = 1:1:Nr,
```

```
    for RotorPos = 0:dx:2*pi-dx,
```

```
        Shift = floor(RotorPos/dx);
```

```
        Barna1(BarNo,:) = circshift(Barna(BarNo,:),[0 Shift]);
```

```
        ICoilNaBarna(BarNo,count) = sum(MCoilNa.*Barna1(BarNo,:).*Igeff.*AvgR)*2*pi/H;
```

```
        ICoilNbBarna(BarNo,count) = sum(MCoilNb.*Barna1(BarNo,:).*Igeff.*AvgR)*2*pi/H;
```

```
        ICoilNcBarna(BarNo,count) = sum(MCoilNc.*Barna1(BarNo,:).*Igeff.*AvgR)*2*pi/H;
```

```
        count = count + 1;
```

```
    end;
```

```
    count = 1;
```

```
end;
```

```
Lar = Constant.*ICoilNaBarna;
```

```
Lbr = Constant.*ICoilNbBarna;
```

```
Lcr = Constant.*ICoilNcBarna;
```

```
Lsr(:,1) = Lar;
```

```
Lsr(:,2) = Lbr;
```

```
Lsr(:,3) = Lcr;
```

A4. Current and torque calculation script

```

clearvars Index1 Array RotorElecAngle RotorAngVel RotateElec;
clearvars A B dLsr supp I Te Tetemp;

%Initialisation States
f = 55;
T = 1/(2*f);
H1 = 128;           % Number of samples
TimeStep = (T)/H1; % Timestep in seconds
CycleNo = 60;

C = eye(3+Nr+1,3+Nr+1);
D = zeros(3+Nr+2,3+Nr+1);

J = 0.02;           % Moment of inertia, kg.m^2
b = 0.000124;      % Coefficient of friction
c = 6;             % Constant of Tm

% Voltage Calculations%
t1 = 0:TimeStep:CycleNo*T;
Va = 230*cos((2*pi*f*t1)-(2*pi/3));
Vb = 230*cos((2*pi*f*t1)+(2*pi/3));
Vc = 230*cos((2*pi*f*t1));
Vs = [Va;Vb;Vc];

Vr = zeros(Nr+1,CycleNo*H1+1);
V = [Vs;Vr];

%Preallocating Arrays
I = zeros(3+Nr+1,CycleNo*H1+1); % Initial states
Itemp = zeros(3+Nr+1,CycleNo*H1+1);
Te = zeros(1,CycleNo*H1);
RotorAngVel = zeros(1,CycleNo*H1);

for t = 0:TimeStep:CycleNo*TimeStep*H1-TimeStep,

    Index1 = round(t/TimeStep)+1;
    Array(1,Index1) = RotorElecAngle;
    RotorElecAngle = RotorElecAngle - 2*pi*floor(RotorElecAngle/(2*pi));
    RotateElec = fix(RotorElecAngle/dx) + 1;

    [A, B, dLsr supp] =
    InductanceMatrix(t,Lss,dLsr,Lsr,Lrr,RotorAngVel(1,Index1),RotateElec,Rs,Rr);

% Current calculations

    Itemp(:,Index1) = B\V(:,Index1)-(B\A)*I(:,Index1);

    [I(:,Index1+1) y ~] = Integra(Index1, TimeStep, Itemp(:,1:Index1));

    Te(1,Index1+1) =
    0.5.*(I(1:3,Index1)*dLsr supp)'*I(4:end,Index1)+(I(4:end,Index1)*dLsr supp)*I(1:3,Index1));
    Tetemp = (1/J).*Te(1,1:Index1);
    RotorAngVel(1,Index1+1) = (Integra(Index1, TimeStep, (Tetemp)));

```

```
RotorElecAngle = Integra(Index1,TimeStep,RotorAngVel(1,1:Index1));
```

```
end;
```

A5.Functions

A5i. Integra function

```
function [Y1,y,x] = Integra(Index1, TimeStep, X)
x(:,1) = X(:,1);
y(:,1) = x(:,1);

for n = 1:1:Index1-1,
    y(:,n) = x(:,n);
    x(:,n+1) = x(:,n) + TimeStep.*X(:,n);
end
Y1 = y(:,end);
end
```

A5ii. InductanceMatrix function

```
function [A, B, dLsrssupp] = InductanceMatrix(t,Lss,dLsr,Lsr,Lrr,Wr,RotateElec,Rs,Rr)
Ke = 0.0059;
Ki = 18.2291;
C = eye(32,32);
D = zeros(32,32);
if(RotateElec == 89),
    RotateElec = 90;
end;
dLsrssupp = [squeeze(dLsr(:,RotateElec,:)); squeeze(dLsr(1,RotateElec,:))];
Lsrssupp = [squeeze(Lsr(:,RotateElec,:)); zeros(1,3)];
Lrrrefsupp = squeeze(Lrr(:,RotateElec,:));

L = [Lss Lsrssupp'; Lsrssupp (Ki/Ke).*Lrrrefsupp];
R = [Rs zeros(3,29); zeros(29,3) (Ki/Ke).*Rr];

Z1 = Wr.*dLsrssupp';
Z2 = Wr.*dLsrssupp;
Z3 = Wr.*Lrrrefsupp;
dL = [zeros(3,3) Z1; Z2 Z3];

A = (R+dL);
B = L;

end
```

References

-
- [1] S. Djebbari, J. F. Charpentier, F. Sculler, and M. Benbouzid, "A systemic design methodology of PM generators for fixed-pitch marine current turbines," in *2014 First International Conference on Green Energy ICGE 2014*, 2014, pp. 32-37.
- [2] Atlantis. (25/07). *SeaGen Brochure*. Available: <https://www.atlantisresourcesltd.com/wp/wp-content/uploads/2016/08/SeaGen-Brochure.pdf>
- [3] OpenHydro. (18/11/2013). *Company History*. Available: <http://www.openhydro.com/Company/History>
- [4] OpenHydro. (07/09/2017). *OpenHydro Projects*. Available: <http://www.openhydro.com/Projects>
- [5] A. C. Baker, *Tidal power*. London, U.K.: P. Peregrinus, 1991.
- [6] R. Kirby and T. L. Shaw, "Severn Barrage, UK—environmental reappraisal," *Proceedings of the Institution of Civil Engineers - Engineering Sustainability*, vol. 158, pp. 31-39, 2005.
- [7] H. Headland, "Tidal power and the Severn Barrage," *Electrical Engineers, Journal of the Institution of*, vol. 1949, pp. 164-166, 1949.
- [8] S. E. B. Elghali, M. E. H. Benbouzid, and J. F. Charpentier, "Marine Tidal Current Electric Power Generation Technology: State of the Art and Current Status," in *2007 IEEE International Electric Machines & Drives Conference*, 2007, pp. 1407-1412.
- [9] R. A. Dunlap, *Sustainable energy*, 2nd edition. ed.
- [10] Tidal Lagoon Power. (2017, February 27th). *Swansea Bay Project* [online]. Available: <http://www.tidallagoonpower.com/projects/swansea-bay/>
- [11] J. Hardisty and Ebooks Corporation. (2009). *The analysis of tidal stream power*. Available: http://www.NCL.ebib.com/EBLWeb/patron?target=patron&extendedid=P_437512_0&
- [12] S. Draper, G. T. Houlby, M. L. G. Oldfield, and A. G. L. Borthwick, "Modelling tidal energy extraction in a depth-averaged coastal domain," *Renewable Power Generation, IET*, vol. 4, pp. 545-554, 2010.
- [13] F. Maganga, G. Germain, J. King, G. Pinon, and E. Rivoalen, "Experimental characterisation of flow effects on marine current turbine behaviour and on its wake properties," *Renewable Power Generation, IET*, vol. 4, pp. 498-509, 2010.
- [14] P. Mycek, B. Gaurier, G. Germain, G. Pinon, and E. Rivoalen, "Experimental study of the turbulence intensity effects on marine current turbines behaviour. Part II: Two interacting turbines," *Renewable Energy*, vol. 68, pp. 876-892, 8// 2014.
- [15] N. J. Baker, S. Cawthorne, E. Hodge, and E. Spooner, "3D modelling of the generator for OpenHydro's tidal energy system," in *Power Electronics, Machines and Drives (PEMD 2014), 7th IET International Conference on*, 2014, pp. 1-6.
- [16] OpenHydro. (24/07/2017). *Operation and Maintenance*. Available: <http://www.openhydro.com/technology/site-selection>
- [17] E. Spooner and OpenHydro, "A subsea permanent magnet generator," *MagNews*, pp. 26-27, 2014.
- [18] M. Calasan, N. Šoć, V. Vujičić, G. Joksimović, C. Hao, Q. Wang, *et al.*, "Review of marine current speed and power coefficient; Mathematical models," in *2015 4th Mediterranean Conference on Embedded Computing (MECO)*, 2015, pp. 427-431.
- [19] T. Burton, *Wind energy handbook*, 2nd ed.. ed. Chichester, West Sussex

Oxford: Chichester, West Sussex : Wiley, 2011.

- [20] Y. Xia, K. H. Ahmed, and B. W. Williams, "Wind Turbine Power Coefficient Analysis of a New Maximum Power Point Tracking Technique," *IEEE Transactions on Industrial Electronics*, vol. 60, pp. 1122-1132, 2013.
- [21] OpenHydro. (2014, 04/06/2014). *Deployment*. Available: <http://www.openhydro.com/Technology/Sub-sea-Cabling>
- [22] Great Britain. Hydrographic Department, "Tidal stream atlas. Rosyth Harbour and approaches," in *Np 220*, Ed. 2. ed. Taunton: Hydrographic Dept., 2009.
- [23] P. L. Fraenkel, "Power from marine currents," *Proceedings of the Institution of Mechanical Engineers, Part A: Journal of Power and Energy*, vol. 216, pp. 1-14, February 1, 2002 2002.
- [24] Google. (2018). *Maps*. Available: <https://www.google.co.uk/maps/@56.0081329,-3.4608116,13.25z>
- [25] UK Government. (2018). *Rosyth Tide data*. Available: <http://www.ukho.gov.uk/easytide/EasyTide/ShowPrediction.aspx?PortID=0227&PredictionLength=7>
- [26] A.B.P. Mer. (2014, April 12th). *WEBvision-Renewables Atlas (Tide) (v1.0 ed.)* [online]. Available: http://vision.abpmer.net/renewables/map_default.phtml?config=tide&resetsession=groups,resultlayers
- [27] T. J. E. Miller, *Brushless permanent-magnet and reluctant motor drives*. Oxford New York: Clarendon Press ; Oxford University Press, 1989.
- [28] C. Trust. (2012, 18/11/2013). *Technology Innovation Needs Assessment*. Available: <https://www.carbontrust.com/media/168547/tina-marine-energy-summary-report.pdf>
- [29] Marine Current Turbines. (25/07/2017). *SeaGen Technology*. Available: <http://www.marineturbines.com/Seagen-Technology>
- [30] Atlantis. (25/07/2017). *AR-1500*. Available: <https://www.atlantisresourcesltd.com/wp/wp-content/uploads/2016/08/AR1500-Brochure-Final-1.pdf>
- [31] Scotrenewables. (25/07/2017). *SR2000*. Available: <http://www.scotrenewables.com/projects/flotec>
- [32] Andritz Hydro. (25/07/2017). *HS1000*. Available: <https://www.andritz.com/products-en/group/products/tidal-current-turbines>
- [33] Tidal Energy Today. (2017, 21/04/2017). *Gallery: Nautricity's CoRMAT hits Scottish waters*. Available: <http://tidalenergytoday.com/2017/04/21/gallery-nautricitys-cormat-hits-scottish-waters/>
- [34] Nautricity. (2017, 11/06/2017). *How CoRMAT works*. Available: <http://www.nautricity.com/cormat/cormat-efficiency/>
- [35] Atlantis Resources. (04/07). *MeyGen Phase 1A*. Available: <https://www.atlantisresourcesltd.com/projects/meygen/>
- [36] A. Hughes and B. Drury, *Electric motors and drives : fundamentals, types and applications*, Fourth edition. ed.
- [37] I. Boldea and S. A. Nasar, *The induction machines design handbook*, 2nd ed. Boca Raton, FL: CRC Press/Taylor & Francis, 2010.
- [38] S. Benelghali, M. E. H. Benbouzid, and J. F. Charpentier, "Generator Systems for Marine Current Turbine Applications: A Comparative Study," *Oceanic Engineering, IEEE Journal of*, vol. 37, pp. 554-563, 2012.
- [39] H. Gorginpour, H. Oraee, and R. A. McMahan, "A Novel Modeling Approach for Design Studies of Brushless Doubly Fed Induction Generator Based on Magnetic Equivalent Circuit," *IEEE Transactions on Energy Conversion*, vol. 28, pp. 902-912, 2013.

- [40] C. Concordia, *Synchronous machines : theory and performance*. New York London: Wiley ; Chapman & Hall, 1951.
- [41] X. Yuanyuan, N. Maki, and M. Izumi, "Performance Comparison of 10-MW Wind Turbine Generators With HTS, Copper, and PM Excitation," *Applied Superconductivity, IEEE Transactions on*, vol. 25, pp. 1-6, 2015.
- [42] A. Zavvos, A. S. McDonald, M. Mueller, D. J. Bang, and H. Polinder, "Structural comparison of permanent magnet direct drive generator topologies for 5MW wind turbines," in *Power Electronics, Machines and Drives (PEMD 2012), 6th IET International Conference on*, 2012, pp. 1-6.
- [43] D. C. Hanselman, *Brushless permanent-magnet motor design*. New York: McGraw-Hill, 1994.
- [44] M. A. Mueller, "Design and performance of a 20 kW, 100 rpm, switched reluctance generator for a direct drive wind energy converter," in *Electric Machines and Drives, 2005 IEEE International Conference on*, 2005, pp. 56-63.
- [45] S. Djebbari, J. F. Charpentier, F. Sculler, M. Benbouzid, and S. Guemard, "Rough design of a Double-Stator Axial Flux Permanent Magnet generator for a rim-driven Marine Current Turbine," in *Industrial Electronics (ISIE), 2012 IEEE International Symposium on*, 2012, pp. 1450-1455.
- [46] K. Lu, P. O. Rasmussen, and E. Ritchie, "Design Considerations of Permanent Magnet Transverse Flux Machines," *IEEE Transactions on Magnetics*, vol. 47, pp. 2804-2807, 2011.
- [47] H. Polinder, B. C. Mecrow, A. G. Jack, P. G. Dickinson, and M. A. Mueller, "Conventional and TFPM linear generators for direct-drive wave energy conversion," *IEEE Transactions on Energy Conversion*, vol. 20, pp. 260-267, 2005.
- [48] R. P. Deodhar, A. Pride, and J. J. Bremner, "Design Method and Experimental Verification of a Novel Technique for Torque Ripple Reduction in Stator Claw-Pole PM Machines," *IEEE Transactions on Industry Applications*, vol. 51, pp. 3743-3750, 2015.
- [49] A. Ibala and A. Masmoudi, "On the sizing of the PM excitation of a hybrid claw pole alternator," in *2016 Eleventh International Conference on Ecological Vehicles and Renewable Energies (EVER)*, 2016, pp. 1-6.
- [50] Infolytica. (2018). *MagNet*. Available: <https://www.infolytica.com/en/products/magnet/>
- [51] A. I. Khuri and J. A. Cornell, *Response surfaces : designs and analyses*. New York: M. Dekker, 1987.
- [52] E. R. Laithwaite, "The goodness of a machine," *Electrical Engineers, Proceedings of the Institution of*, vol. 112, pp. 538-541, 1965.
- [53] T. W. Preston and A. B. J. Reece, "Transverse edge effects in linear induction motors," *Electrical Engineers, Proceedings of the Institution of*, vol. 116, pp. 973-979, 1969.
- [54] Infolytica. (2018, 05/03). *MotorSolve*. Available: <https://www.infolytica.com/en/products/motorsolve/>
- [55] M. G. Say, *The performance and design of alternating current machines; transformers, three-phase induction motors and synchronous machines*, 3rd ed. London,: Pitman paperbacks, 1968.
- [56] L. Lagron, R. C. Simpson, and M. G. Say, *Polyphase induction motors, their theory, calculation, and application*. London, Glasgow,: Blackie & son limited, 1931.
- [57] Z. M. Zhao, S. Meng, C. C. Chan, and E. W. C. Lo, "A novel induction machine design suitable for inverter-driven variable speed systems," *Energy Conversion, IEEE Transactions on*, vol. 15, pp. 413-420, 2000.

- [58] J. Faiz and S. M. M. Moosavi, "Detection of mixed eccentricity fault in doubly-fed induction generator based on reactive power spectrum," *IET Electric Power Applications*, vol. 11, pp. 1076-1084, 2017.
- [59] B. J. Hamrock, S. R. Schmid, and B. O. Jacobson, *Fundamentals of fluid film lubrication*, 2nd ed. New York: Marcel Dekker, 2004.
- [60] H. A. Toliyat, M. S. Arefeen, and A. G. Parlos, "A method for dynamic simulation of air-gap eccentricity in induction machines," *IEEE Transactions on Industry Applications*, vol. 32, pp. 910-918, 1996.
- [61] S. Nandi, R. M. Bharadwaj, and H. A. Toliyat, "Performance analysis of a three-phase induction motor under mixed eccentricity condition," *IEEE Transactions on Energy Conversion*, vol. 17, pp. 392-399, 2002.
- [62] A. Purvee, G. Banerjee, T. Munkhjargal, C. Otgonchimeg, and Z. Oyundelger, "Calculation of inductance and dynamic simulation of air eccentricities of squirrel cage induction motor," in *2016 International Conference on Condition Monitoring and Diagnosis (CMD)*, 2016, pp. 69-73.
- [63] H. A. Toliyat and T. A. Lipo, "Transient analysis of cage induction machines under stator, rotor bar and end ring faults," *IEEE Transactions on Energy Conversion*, vol. 10, pp. 241-247, 1995.
- [64] A. Ghoggal, S. E. Zouzou, M. Sahraoui, H. Derghal, and A. Hadri-Hamida, "A winding function-based model of air-gap eccentricity in saturated induction motors," in *2012 XXth International Conference on Electrical Machines*, 2012, pp. 2739-2745.
- [65] A. Ghoggal, S. E. Zouzou, H. Razik, M. Sahraoui, and A. Khezzar, "An improved model of induction motors for diagnosis purposes – Slot skewing effect and air-gap eccentricity faults," *Energy Conversion and Management*, vol. 50, pp. 1336-1347, 2009/05/01/ 2009.
- [66] J. Gojko, "A.C. Winding Analysis Using a Winding Function Approach," *International Journal of Electrical Engineering Education*, vol. 48, pp. 34-52, 2011.
- [67] T. A. Lipo, *Analysis of synchronous machines*, 2nd ed. Boca Raton, FL: Taylor & Francis, 2012.
- [68] OpenHydro. (27/07/2017). *Deployment System*. Available: <http://www.openhydro.com/Technology/Open-Centre-Turbine>
- [69] OpenHydro. (15/08/2017). *Turbine Control Centre*. Available: <http://www.openhydro.com/Technology/Turbine-Control-Centre>
- [70] D. Watson and A. Head, *Corporate finance : principles & practice*, 4th ed. Harlow, England ; New York: FT/Prentice Hall, 2007.
- [71] M. Hajiaghajani, H. Lei, S. M. Madani, and H. A. Toliyat, "A method for detection of eccentricity in permanent magnet machines," in *38th IAS Annual Meeting on Conference Record of the Industry Applications Conference, 2003.*, 2003, pp. 1833-1838 vol.3.